Detailed X-ray properties of galaxy groups and fossil groups

Dissertation
zur
Erlangung des Doktorgrades (Dr. rer. nat.)
der
Mathematisch-Naturwissenschaftlichen Fakultät
der
Rheinischen Friedrich-Wilhelms-Universität Bonn

von
Bharadwaj Vijaysarathy
aus
Chennai

Bonn, 2015

Dieser Forschungsbericht wurde als Dissertation von der Mathematisch-Naturwissenschaftlichen Fakultät der Universität Bonn angenommen und ist auf dem Hochschulschriftenserver der ULB Bonn http://hss.ulb.uni-bonn.de/diss_online elektronisch publiziert.

1. Gutachter:	Prof. Dr. Thomas H. Reiprich
2. Gutachter:	Prof. Dr. Peter Schneider
Tag der Promotion:	10.07.2015
Erscheinungsjahr:	2015

Abstract

Most galaxies in the Universe are aggregated into groups of galaxies, agglomerations of a few 10s of galaxies (at most). Typically, they have been considered to be similar to clusters, which contain a few 100s of galaxies, which however does not mean that the two types of systems have the exact same properties. In this dissertation, the goal was to study the similarities and differences between groups and clusters, for a selection of properties, primarily of the hot X-ray emitting gas, i.e. the intracluster medium. This was carried out via three sub-projects.

In the first project, the goal was to investigate the cool-core properties of a sample of 26 galaxy groups with Chandra data and correlate it to the feedback from the supermassive black hole (SMBH) in the group centres. This involved handling data in three wavelengths, namely, X-ray, radio, and near-infrared (NIR). For the X-ray analysis, the Chandra data was used to extract temperature and density profiles and constrain the central cooling time (CCT) and central entropy; two important cool-core diagnostics. The CCT was used to classify the galaxy groups into strong cool-core, weak cool-core, and non cool-core classes, which was done for the first time for an objectively selected galaxy group sample. The radio output of the central active galactic nucleus (AGN) was constrained using catalogue data and correlated to the CCT. The mass of the central SMBH was determined using NIR data for the brightest cluster galaxy (BCG) from the 2MASS extended source catalogue (XSC), and a scaling relation from Marconi & Hunt (2003). Finally, the scaling relation between the X-ray luminosity/mass of the galaxy group and cluster (L_X/M_{500}) and the NIR luminosity of the BCG was extended all the way from the cluster regime to the group regime. The results show that although the observed cool-core fraction is similar in galaxy groups and clusters, there are important differences between the two classes of objects. Firstly, despite having very short CCTs (CCT $<$ 1 Gyr), there are some galaxy groups which have a centrally rising temperature profile unlike what is observed for clusters. Secondly, there is an absence of a correlation between the CCT and the central radio-loud AGN fraction in groups unlike that for clusters. Thirdly, the indications of an anti-correlation trend between the CCT and the radio luminosity of the central AGN observed for clusters is not seen for galaxy groups. Fourthly, the weak correlation between the radio luminosity and the mass of the SMBH observed for strong cool-core (SCC) galaxy clusters is absent for SCC galaxy groups. Finally, the strong correlation for the L_X–L_{BCG} and the M_{500}–L_{BCG} scaling relation observed for clusters weakens significantly when the scaling relation is extended to the group regime.

In the second project, the bolometric L_X–T scaling relation was extended from the cluster regime to the group regime. Additionally, we studied the impact of ICM cooling and AGN feedback on the scaling relation for the first time for galaxy groups by fitting the relation for individual sub-samples, accounting for different cases of ICM cooling and AGN feedback. The impact of selection effects were qualitatively and quantitatively examined using simulations, and bias-corrected relations were established for the entire sample and all sub-samples. The slope of the bias-corrected L_X–T relation is marginally steeper but consistent within errors to that of clusters ($\sim$ 3), with the relation being steepest and highest in

normalisation for the strong cool-core groups (CCT $\leq$ 1 Gyr), and shallowest for those groups without a strong cool-core. The statistical scatter in T on the group regime is comparable to the cluster regime, while the statistical and intrinsic scatter in $L_{\rm X}$ increases. Interestingly, we report for the first time that the bias-corrected intrinsic scatter in $L_{\rm X}$ is higher than the observed scatter for groups. We also see indications that groups with a relatively powerful radio-loud AGN have a much steeper $L_{\rm X}$–T relation. Finally, we speculate that such powerful AGN are preferentially located in groups which lack a strong cool-core.

The scientific goal of the third project was to investigate the core properties of fossil systems in detail for the very first time using Chandra archival data for 17 systems. The presence/absence of a cool-core in fossils was determined via three diagnostics, namely the CCT, cuspiness, and concentration parameter. The X-ray peak/BCG separation and the X-ray peak/emission weighted centre separation was quantified to give an indication of the dynamical state of the system. We also studied five low redshift fossils ($z < 0.05$) in detail and obtained their deprojected ICM properties. Lastly, we also studied the $L_{\rm X}$–T relation which shows indications of being shallower and higher in normalisation compared to other galaxy groups, after factoring in potential selection effects. We interpreted these results within the context of the formation and evolution of fossils, and concluded that these systems are affected by non-gravitational processes particularly AGN feedback which leaves a strong imprint on the ICM.

Contents

CHAPTER 1

Introduction

It would not be an exaggeration to state that the current decade is the golden age of precision cosmology. This is largely due to a multitude of missions/telescopes in different stages of planning and execution, which will offer unparalleled multi-wavelength coverage to researchers. The most recent one, namely the Planck mission (Planck Collaboration et al. 2014a), has managed to constrain the cosmological parameters to a very high level of precision, albeit some of the numbers are in tension with results from previous studies (e.g. the value of the Hubble constant H_0 and the matter density parameter Ω_M, Planck Collaboration et al. 2014b). Complementary to Planck will be two upcoming missions, namely eROSITA and Euclid (Predehl et al. 2010; Laureijs et al. 2011 respectively, Fig. 1.1), which will try to understand dark energy, that is considered to comprise 68% of the energy content of the Universe (Planck Collaboration et al. 2014b). Both Euclid and eROSITA are stage-IV dark energy missions as illustrated by the dark energy task force (Albrecht et al. 2006) and would be the next step after Planck in space-based cosmological missions. For X-ray astronomers, the eROSITA instrument is undoubtedly one of the most exciting X-ray missions in the next decade along with other missions such as the USA's NuSTAR (Harrison et al. 2013), and Japan's Astro-H (Takahashi et al. 2014). eROSITA is slated to perform only the second ever imaging all-sky survey in the X-ray wavelength, with the fundamental aim of detecting close to 10^5 galaxy clusters, and constrain the dark energy equation of state (e.g. Merloni et al. 2012).

With their complex structure consisting of galaxies, hot X-ray emitting gas (collectively called "baryons"), and dark matter, galaxy clusters are excellent laboratories for both cosmologists and astrophysicists. Cosmologists are keen on investigating their masses and distribution to constrain the large-scale structure of the Universe, and to throw light on the fraction of dark matter and dark energy (e.g. Reiprich 2006; Vikhlinin et al. 2009b). Astrophysicists on the other hand, are investigating complicated baryonic physics and answering questions such as how the X-ray emitting gas on the kiloparsec scale interacts with a supermassive black hole on the parsec level (e.g. Churazov et al. 2002). It would not be a far stretch to say that the study of galaxy clusters in the next decade with the latest and best instruments, both ground and space-based, across wavelengths, will probably consolidate our understanding of the Universe like never before. Though not very obvious, understanding baryonic physics via X-rays is absolutely important for cluster cosmology. Survey telescopes like eROSITA will not have enough cluster X-ray photons to constrain physical properties such as the mass and the temperature of the hot X-ray emitting gas of the galaxy cluster directly, making one dependent on observable proxies such as the X-ray luminosity, and correlations (i.e. scaling relations) to constrain these physical properties. To

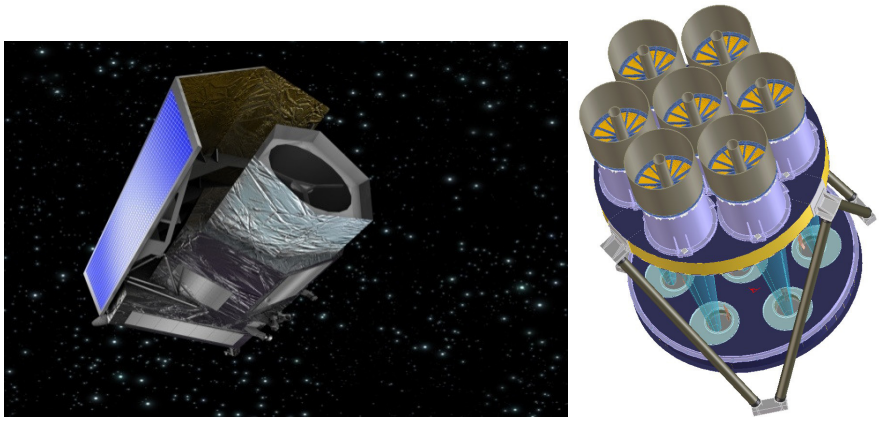

Figure 1.1: *Left:* Artist rendition of the Euclid telescope (optical). Figure credit; ESA-C. Carreau. *Right:* Artist rendition of the eROSITA telescope (X-rays). Figure credit; eROSITA consortium. Both missions are survey missions that have the primary science objective of understanding the mysterious dark energy.

ensure that the observable is a good descriptor of the underlying physical properties, one will have to understand the gas physics at play in clusters, as these physics makes scaling relations deviate from simple theoretical expectations. Several unanswered questions abound in baryonic physics such as: What is the role of intracluster medium (ICM) cooling and feedback from supermassive black holes in the cores of clusters? What happens to the X-ray gas in the outermost regions of these massive objects? Why do X-ray scaling relations deviate from self-similarity? Is there a similarity break between the high-mass "clusters" and the low-mass "groups"? Each of these questions is directly interesting to an astrophysicist, and their implications on cosmological studies of clusters makes them also relevant for cosmologists. With the first data set of the eROSITA all-sky survey to arrive within the next three years, it is important to answer many, if not most of these questions as soon as possible with existing data sets, which would ensure that observable proxies can be used with accuracy on the survey data to constrain the physical properties and cosmological parameters thereon.

Theoretical and observational results indicate that most galaxy clusters are in the low-mass regime (e.g. Tinker et al. 2008) and are accorded the nomenclature "galaxy groups". In recent years, galaxy group studies have gained traction, albeit still not to the extent of galaxy clusters. Indeed, a simple astrophysics data system (ADS)[1] abstract search shows that searching "galaxy clusters" and "galaxy groups" yields entries which are lower by almost a factor of 8 for the latter, though admittedly this is not corrected for overlapping studies. Observationally, galaxy groups are not as easy to explore as high-mass clusters in X-rays due to their low surface brightness and the expected impact of gravitational and non-gravitational processes on their structure. Thus, despite being much more numerous than high-mass clusters, using them for precision cosmology studies has still not been explored in detail. This should however not be seen as a drawback, but as an opportunity to do more work on the low-mass regime, particularly in X-rays. This dissertation is one such attempt, where we explore in detail certain X-ray properties of galaxy groups, their impact on scaling relations, and also provide a brief outlook for the upcoming eROSITA all-sky survey. Presented mostly as a collection of research papers of which I have been the lead author, this dissertation presents results from independent scientific investigations with the underlying theme of understanding the X-ray properties of galaxy groups and fossil systems in detail.

The organisation of this dissertation is as follows: Chapter 2 presents a theoretical background on the subject matter and brings the reader up to speed with the requisite knowledge for understanding the sci-

[1] http://adsabs.harvard.edu/abstract_service.html

entific results in subsequent chapters. Chapter 3 discusses X-ray astronomy in general, with a focused look into the Chandra X-ray telescope, and a brief overview of eROSITA. Chapter 4 discusses ICM cooling, AGN feedback and BCG properties of galaxy groups and results thereof. Chapter 5 presents the impact of ICM cooling, AGN feedback and selection effects on the X-ray luminosity (L_X) and temperature (T) scaling relation for galaxy groups, and comparisons to the scaling relation for clusters. Chapter 6 looks into some properties of fossil systems, an interesting sub-class of clusters/groups, and focuses mainly on their core properties. Chapter 7 is a detailed summary of all the scientific investigations conducted in this dissertation, and also provides an outlook for potential future studies. Preliminary results of a pilot study on estimating gas masses from the upcoming eROSITA all-sky survey are also presented.

CHAPTER 2

Theoretical background

2.1 Galaxy groups and clusters

With masses between 10^{13}–10^{15} solar masses ($M_\odot$), galaxy groups/clusters are the largest gravitationally bound objects in the Universe. The choice of nomenclature is a natural one, as these systems are essentially an aggregation of galaxies bound by gravity. This is a very simplistic definition however, as galaxies form only a part of the total mass and in reality these are much more complex systems than originally envisioned. The distribution of matter within galaxy clusters and groups is organised as follows:

- Galaxies which number from as few as 4-5 to a few 1000.
- Hot X-ray emitting gas known as the intracluster medium (ICM) which has a temperature of around 10^7 K. The ICM is generally the dominant baryonic component in clusters.
- Dark matter accounts for roughly 80% of the total mass of the cluster and is the dominant source of the gravitational potential in clusters.
- Relativistic particles with velocities comparable to the speed of light.

2.1.1 Galaxy groups

Typically when galaxy clusters contain few 10s of galaxies, they are called as galaxy groups to represent a smaller aggregation of galaxies. Alternatively, one could classify clusters with total masses less than 10^{14} $M_\odot$ or with ICM temperatures below 2 keV as galaxy groups (e.g. Stott et al. 2012). Generally, the low mass/low temperature objects have fewer galaxies and vice-versa, but this is not always true. Fossil groups of galaxies (Ponman et al. 1994) for instance, could have high masses and temperatures, but low optical richness[1].

The shape of the galaxy cluster mass function, i.e. the number density of clusters as a function of mass (e.g. Tinker et al. 2008), shows that most galaxies in the universe are organised in low-mass groups, making them far more numerous than high-mass clusters (Fig. 2.1). Moreover, due to their shallower gravitational potential, they are expected to be much more strongly affected by processes such as mergers, feedback from supermassive black holes (SMBH), and galactic winds. The plethora of these

[1] richness is a measure of the number of galaxies in a cluster/group, see Sec. 2.2

objects, and the impact of gravitational and non-gravitational effects on them (particularly in X-rays), make galaxy groups potentially excellent cosmological and astrophysical laboratories, sometimes more so than their high-mass counterparts. On a practical note, however, given their low masses, low-surface brightness (especially in X-rays), and low optical richness, galaxy groups provide a rather strong observational challenge for scientists. Even on the theoretical side, the impact of baryonic[2] physics on global properties is hard to simulate as the details of many processes are poorly understood. Throughout this dissertation, important similarities and differences between galaxy clusters and groups will be highlighted and explained as and when relevant.

2.2 Cluster galaxies

When observed in the optical wavelength, galaxy clusters appear as an overdensity of galaxies. Most galaxies in the Universe are not isolated but aggregated into clusters/groups, but as mentioned above they comprise a very small fraction of the mass ($< 5\%$) for rich clusters (e.g. Fukugita et al. 1998). Galaxy groups however, could have up-to 20% of their mass in the cluster galaxies (e.g. Schindler 2004). The term optical richness is used to quantify the number of galaxies associated with the cluster. An optically "rich" cluster would have more than 100 galaxies, while an optically "poor" cluster would have less than 50 galaxies. A more formal usage of richness was provided by Abell 1958 to identify and classify clusters into the famous Abell catalogue. In that catalogue, richness classes varying from 0 (< 50 galaxies) to 5 (> 300 galaxies) were used to identify and classify potential galaxy clusters. Note that, at times cluster membership can be contentious due to strong projection effects making it highly imperative to estimate velocities and redshifts for galaxies which accurately determines cluster membership. The most accurate method to measure redshifts is to obtain the spectra of the galaxy and compare the spectral lines of the object to the rest-frame predictions (Fig. 2.2). This is however rather time consuming and is difficult for surveys where hundreds of thousands of galaxies are observed. A less resource-intensive method to measure redshifts is to use photometry, wherein the measurement of the flux of the object through different filters gives an estimation of the redshift of the object (e.g. Koester et al. 2007). The errors on photometric redshifts at times however are substantially larger than spectroscopic redshifts (e.g. Bolzonella et al. 2000).

The luminosity distribution of the galaxies in a cluster can be well described by the Schechter luminosity function (Schechter 1976) as follows:

$$n(L) = \left(\frac{N^*}{L^*}\right)\left(\frac{L}{L^*}\right)^{-\alpha} \exp\left(-\frac{L}{L^*}\right) \tag{2.1}$$

where L^* is a characteristic luminosity of the galaxies and N^* is a normalisation ($\sim 10^{-2}h^3\mathrm{Mpc}^{-3}$) for L^*. The powerlaw index α varies from 0.8 to 1.3. The function demonstrates that the number of galaxies decreases for increasing luminosity, i.e. there are more galaxies of a lower luminosity than a higher one (Fig. 2.3).

Most galaxies in clusters are elliptical E and lenticular i.e. S0 type (Dressler 1980, 1984; Oemler 1992). In the centres of most relaxed clusters are massive galaxies which are generally the brightest galaxy in the system and are thus assigned the nomenclature BCG—brightest cluster galaxy. These are usually supergiant ellipticals (cD type in the Yerkes galaxy classification system, Fig. 2.4), have an extremely extended outer envelope, and are thought to be the remnants of the mergers of smaller galaxies into a larger one (e.g. Dubinski 1998). Despite consisting of older, more "red" stars, the BCGs

[2] Baryons in this context always refers to the intracluster medium and galaxies

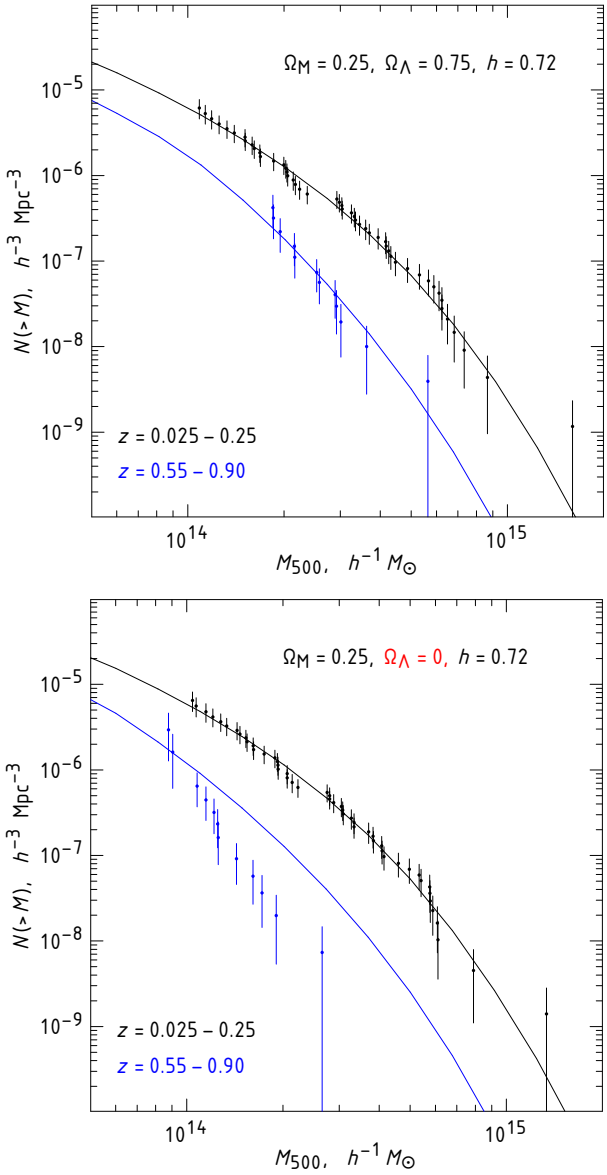

Figure 2.1: Predicted galaxy cluster mass function (number density of clusters as a function of mass) for two samples of clusters in two different redshifts, and for different cosmological parameters, plotted with data points from the Chandra observations. The plot also indicates the sensitivity of the choice of cosmological model on the mass function. From Vikhlinin et al. (2009b).

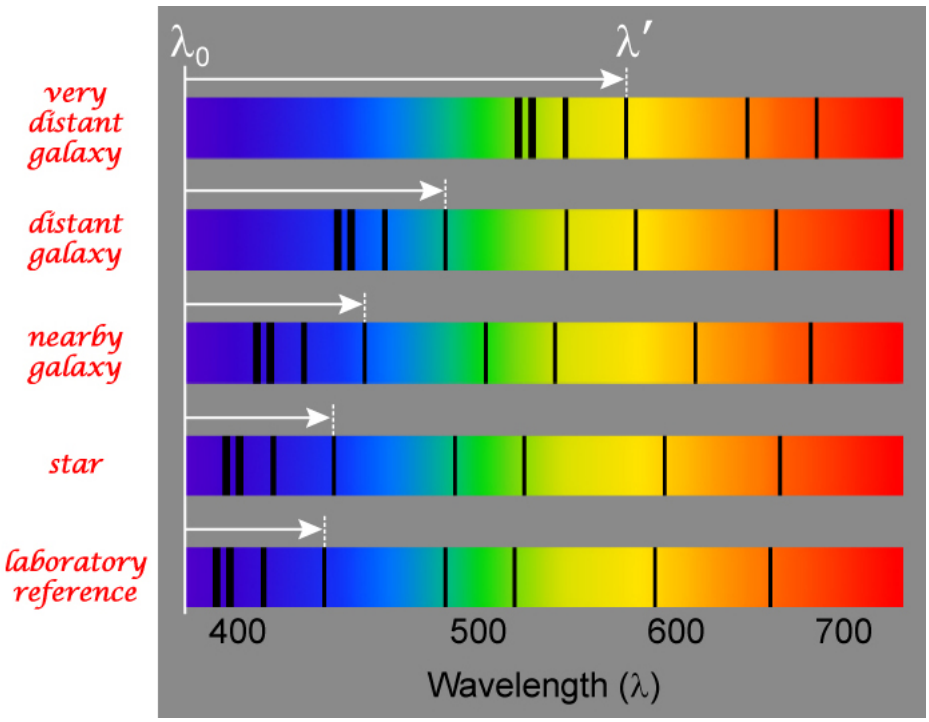

Figure 2.2: Simple pictorial representation of redshift. Notice that greater the distance of the object from us, more is the spectral line shifted to the right, i.e. the red part. Figure from http://planck.caltech.edu/epo/epo-cmbDiscovery1.html

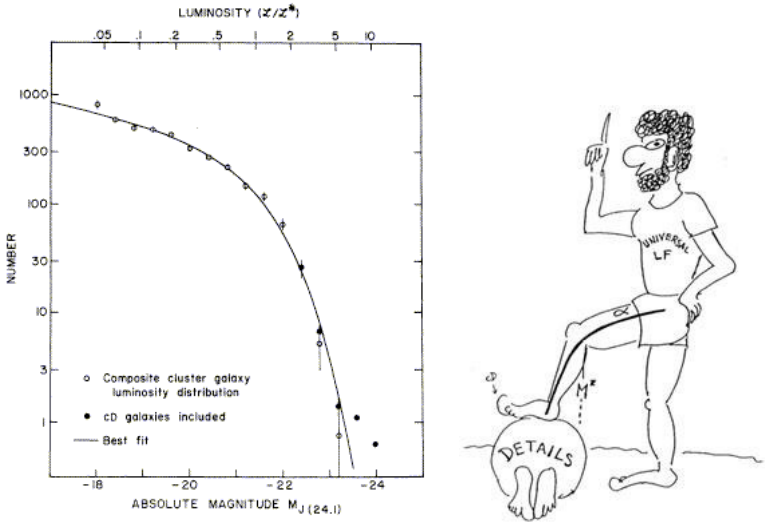

Figure 2.3: *Left*: Schechter luminosity function (Schechter 1976). The plot shows that the number of galaxies increases toward the lower brightness end. *Right:* A cartoon by Bingelli (1987) which shows that the original luminosity function does not quite explain the details on why it has this form.

Figure 2.4: The supergiant elliptical (cD) galaxy M87, which is located at the centre of the Virgo cluster. This galaxy is actually the second brightest one in this galaxy cluster consisting of $\sim$ 1000 galaxies. Image credit: Anglo-Australian observatory.

in some cooling flow clusters (Sect. 2.6) show traces of recent star formation (e.g. Hicks et al. 2010) which can be estimated e.g. through Hα spectra (Kennicutt 1998).

2.3 Dark matter

The dominant mass in a galaxy cluster is in the invisible matter known as dark matter. Dark matter does not emit any electromagnetic radiation and its effect on baryonic matter can only be estimated through gravitational interaction. Zwicky (1933) was the first to postulate the existence of an invisible matter in galaxy clusters, when he concluded that the high mass-to-light ratio in the Coma cluster of galaxies could not be explained by just the galaxies[3]. One of the biggest outstanding questions in astrophysics today is the nature of dark matter itself, with weakly interacting massive particles (WIMPs) being the prime candidate (e.g. Blumenthal et al. 1984) over baryonic possibilities such as massive compact halo objects (MACHOs, Griest 1991) and robust association of massive baryonic objects (RAMBOs, Moore & Silk 1995). In order to study dark matter, astronomers exploit its gravitational potential via gravitational lensing. Some details are presented in the next section.

2.3.1 Gravitational lensing

When light from a distant object (e.g. galaxy) travels to us, it is affected by the gravitational field of an intermediate mass distribution (e.g. galaxy cluster) and gets deflected, hence the name gravitational lensing (Fig. 2.5). Gravitational lensing can be broadly classified into two types, strong and weak lensing. Strong lensing results in multiple images and arcs of the background galaxies (Fig. 2.6). Weak lensing, as the name suggests, is a much weaker effect and results in weak magnification (convergence) and elliptical distortions (shear) of the images of background galaxies by the foreground mass distributions. Note that background galaxies have an intrinsic ellipticity called "shape noise" which needs to be accounted for when measuring the lensing shear (Fig. 2.7).

The major advantage of gravitational lensing for determining the total mass distribution in galaxy clusters is the lack of any strong assumptions such as hydrostatic equilibrium, which is generally considered for other methods such as X-rays. Moreover, considering that the lensing effect is agnostic to the

[3] Though at that time the ICM was not know, and some of the missing matter is in the hot X-ray gas

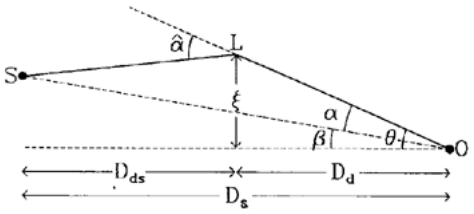

Figure 2.5: Ray geometry of gravitational lensing. S represents the source (background galaxy), L the lens (foreground cluster), and O is the observer. D_d, D_s, D_{ds} are the respective distances (angular diameter distances). Figure credit: http://ned.ipac.caltech.edu/level5/Blandford/Blandford3.html

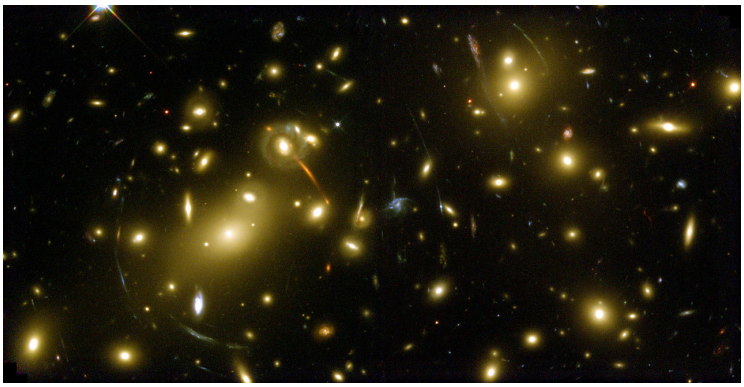

Figure 2.6: The galaxy cluster Abell 2218. The arcs visible in the image are background galaxies which are lensed by the foreground galaxy cluster. Image credit: NASA, ESA, A. Fruchter and the ERO Team (STScI, ST-ECF)

nature of the matter in the cluster, and X-rays map out only the dominant baryonic component, a combined lensing/X-ray analysis, can accurately map out the total baryonic and non-baryonic composition of the cluster. Such a combined analysis has provided one of the strongest astronomical evidences for dark matter, namely the famous bullet cluster (Markevitch et al. 2002). Fig. 2.8 shows the bullet cluster with the projected mass distribution (from lensing) overlaid with the distribution of the hot X-ray gas. The high significance of the spatial offset of the centre of the total mass of the object from the centre of the baryonic mass peaks is a clear indicator of the presence of dark matter (Clowe et al. 2006).

2.4 The intracluster medium

The intracluster medium (ICM) is a highly rarefied plasma with densities typically between 10^{-4}–10^{-1} cm^{-3}, temperatures between 1 and 10 keV, and highly luminous in the X-ray band with bolometric luminosities between 10^{43}–10^{45} erg/s. It comprises up to 20% of the total matter in the cluster and is the dominant baryonic component in high-mass clusters, which however, is not necessarily true for low-mass groups (Schindler 2004; Giodini et al. 2009). The origin of the gas is still somewhat unclear, though the presence of heavy elements makes it unlikely that the gas is purely primordial. A possibility is that the gas bound to the individual galaxies which had been metal-enriched by the supernovae within the galaxies (Arnaud et al. 1992), was stripped from the galaxy as it fell into the cluster potential well (e.g. Schindler 2004). The most widely accepted mechanism for the stripping of the gas in the galaxy is ram-pressure stripping (Gunn & Gott 1972), which is essentially the stripping of the gas caused by the pressure exerted on the galaxy as it moves through the fluid ICM. Another possibility is galactic

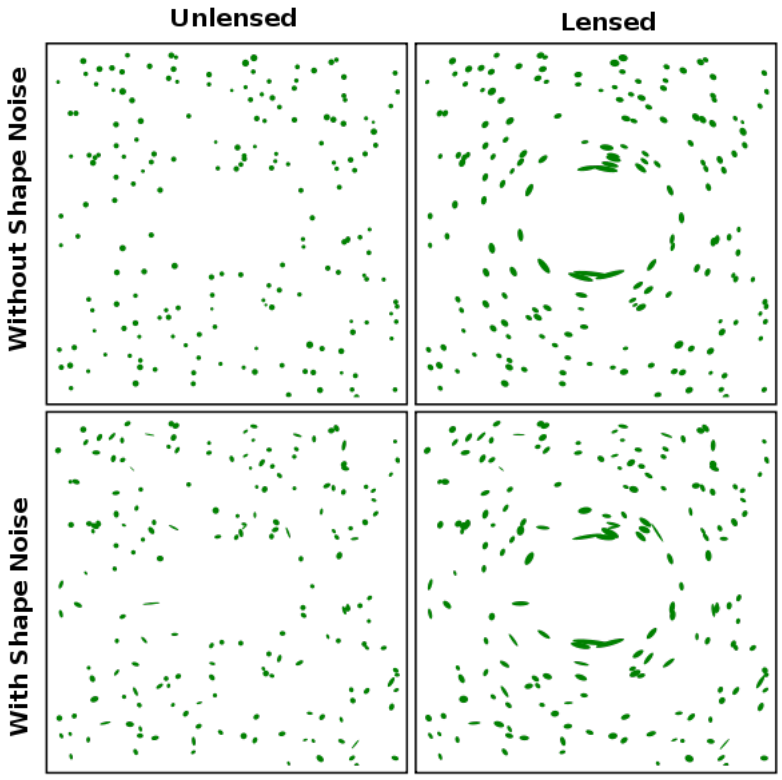

Figure 2.7: An over-simplified pictorial representation of weak lensing. The top left image shows circular unlensed "sources", while the top right image shows the effect of a foreground mass distribution on the images of these sources. Notice the distortion on the sources into elliptical shapes. The bottom left image shows a more "realistic" distribution of galaxies with an intrinsic ellipticity and the effect of lensing is seen on the right. Figure credit: http://upload.wikimedia.org/wikipedia/commons/thumb/9/9c/Shapenoise.svg/400px-Shapenoise.svg.png

Figure 2.8: The galaxy cluster IE0657-56, a.k.a., the bullet cluster. The weak lensing mass distribution is shown in blue and the X-ray emission is shown in red. The spatial offset of the two components provides a strong indication for dark matter. Image credit: NASA/CXC/CfA/M.Markevitch et al. for X-ray image, NASA/STScI; ESO WFI; Magellan/U.Arizona/D.Clowe et al. for lensing map, NASA/STScI; Magellan/U.Arizona/D.Clowe et al. for optical image

winds, which is argued as a better alternative to ram-pressure stripping to explain the nearly constant metallicity observed at the virial radii for some objects (e.g. Fujita et al. 2008; Werner et al. 2013).

The ICM can be studied via two different techniques, namely through the Sunyaev-Zeldovich (SZ) effect and through X-ray observations.

2.4.1 Studying the ICM using the Sunyaev-Zeldovich effect

The cosmic microwave background (CMB) is used to signify photons from an era of the Universe when the photons decoupled from primordial matter and are visible at the present epoch in the millimetre wavelength in the entire sky (Fig. 2.9). As these photons travel to the observer, they pass through galaxy clusters and experience inverse Compton (IC) scattering by the electrons of the ICM and this is referred to as the Sunyaev-Zeldovich effect (Sunyaev & Zeldovich 1972). This IC scattering is visible as a decrease in the CMB intensity below 218 GHz and an increase in intensity above it (Fig. 2.10). The signal arising due to the Sunyaev-Zeldovich effect is redshift independent making it an excellent tool in discovering high-redshift clusters (e.g. Birkinshaw 1999; Carlstrom et al. 2002). However, it is strongly dependent on the mass of the object (e.g. Motl et al. 2005) making it difficult to discover and study low-mass groups with this method.

2.4.2 ICM in X-rays

Given their high temperatures, the primary wavelength to observe and study the ICM are X-ray wavelengths. There are two main emission processes, namely thermal Bremsstrahlung and line emission which characterise the X-ray spectrum of the ICM (Fig. 2.11).

In order to understand the emission processes more clearly, we need to define some common terminology such as flux, luminosity and emissivity.

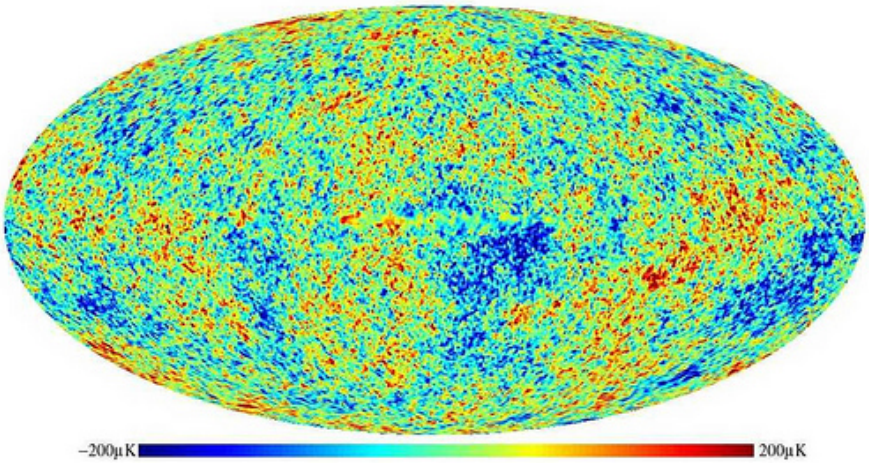

Figure 2.9: Temperature fluctuations of the cosmic microwave background as observed by the WMAP satellite. Image credit: NASA/WMAP.

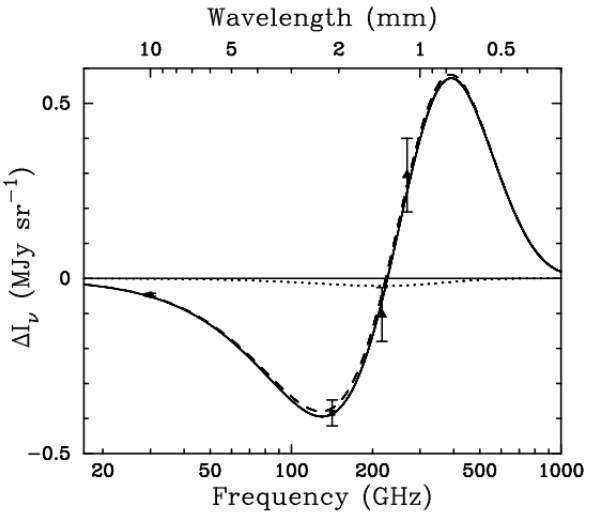

Figure 2.10: Example of the Sunyaev-Zeldovich effect for the cluster Abell 2163. There is a decrease in the CMB intensity below 218 GHz and an increase above it. The dashed and dotted lines represent the thermal and kinetic SZ effect respectively, with the solid line representing the combined effect. Figure credit: Carlstrom et al. (2002).

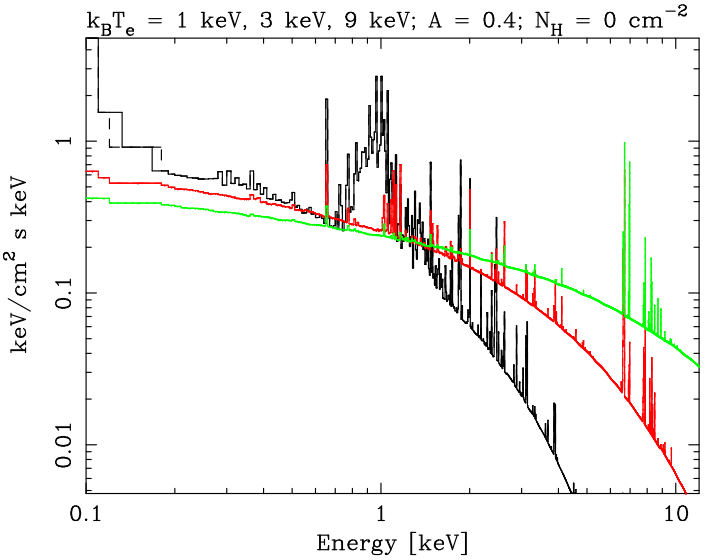

Figure 2.11: Typical spectra for the ICM of a galaxy cluster (Bremsstrahlung with line emission). Black, red, and green correspond to objects with temperatures of 1 keV, 3 keV, and 9 keV respectively. As the temperature of the cluster increases, the Bremsstrahlung cut-off moves to higher energies. Figure credit: Reiprich et al. (2013).

Terminology in X-rays

The amount of energy (dE) per area (dA) per time (dt) interval is defined as the X-ray flux (f_X) of the object. As is the convention in X-ray astronomy, in CGS units the flux would be expressed in erg/s/cm^2.

The X-ray luminosity (L_X) i.e., the energy emitted per unit time (erg/s in CGS units) would then be defined as:

$$L_X = 4\pi f_X d^2, \tag{2.2}$$

where d is the distance to the object. It must be noted that in cosmological scales, this distance is the luminosity distance (D_L).

The emissivity ϵ is the energy per unit time per volume, or expressed mathematically:

$$\epsilon = \frac{\mathrm{d}L_X}{\mathrm{d}V}, \tag{2.3}$$

where V is the volume. ϵ takes the units erg/s/cm^3 in CGS units.

When one wishes to talk about a specific emission process, the emissivity can be defined as a function of frequency, i.e. $\epsilon_\nu = \mathrm{d}L_X/\mathrm{d}V/\mathrm{d}\nu$.

Mathematical formalism of X-ray emission of the ICM

Broadly speaking, one can define the emission from the ICM, which is collisionally ionised, in two different temperature ranges, above and below 2 keV. The dominant emission process differs in both cases. For ICM temperatures above 2 keV it is thermal Bremsstrahlung. The emissivity for this emission can be expressed as follows:

We start with the assumption that the electrons are in thermal equilibrium in the ICM and that it

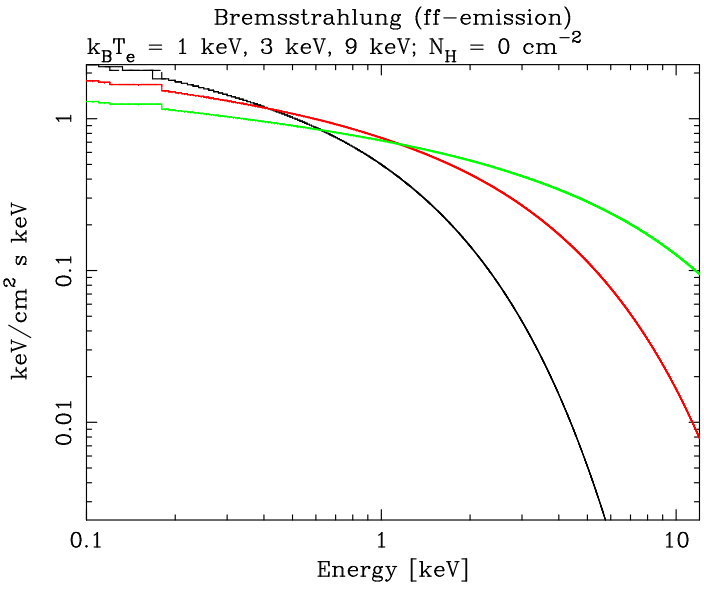

Figure 2.12: Bremsstrahlung spectra as a function of temperature for an optically thin plasma. Once again, black, red, and green correspond to objects with temperatures of 1 keV, 3 keV, and 9 keV respectively. For higher energies, the exponential cut-off moves to higher energies. Here, the densities are kept constant for all three temperatures. Figure credit: http://www.astro.uni-bonn.de/~reiprich/act/gcs/Spectra/.

follows a Maxwell-Boltzmann distribution, i.e.

$$f(v) = \left(\frac{m}{2kT}\right)^3 4\pi v^2 \exp\left(\frac{-mv^2}{2kT}\right), \tag{2.4}$$

where v is velocity and m is mass of the particle, T is the thermodynamic temperature and k is the Boltzmann's constant. Integrating over the velocity distribution and writing in terms of frequency ν, one can express the emissivity as

$$\epsilon_\nu = (6.8 \times 10^{-38}) Z^2 \, n_e n_i g_{ff}(Z, T, \nu) T^{-\frac{1}{2}} e^{-\frac{h\nu}{kT}}, \tag{2.5}$$

where n_e and n_i is the electron and ion number density, respectively, Z is the ion charge, and g_{ff} is the gaunt factor, a correction for quantum mechanical effects.

Integrating over the entire frequency range, we get the total emissivity as

$$\epsilon^{ff} = \int_0^\infty \epsilon_\nu \, d\nu \tag{2.6}$$

$$\implies \epsilon^{ff} \propto n_e^2 T^{-\frac{1}{2}} \int_0^\infty e^{-\frac{h\nu}{kT}} \, d\nu \tag{2.7}$$

$$\implies \epsilon^{ff} \propto n_e^2 T^{\frac{1}{2}}. \tag{2.8}$$

Thus, for Bremsstrahlung emission, the emissivity increases with increasing temperature and increasing density (Fig. 2.12).

For temperatures below 2 keV, line emission dominates over Bremsstrahlung emission. In general,

the most prominent line emission in ICM spectra is the Iron-L and Iron-K shell complexes at 1 and 6 keV, respectively (Fig. 2.11). The emissivity for plasmas of temperature below 2 keV as a function of electron density and temperature can be roughly expressed as (e.g. Sutherland & Dopita 1993)

$$\epsilon^{\text{line}} \propto n_{\text{e}}^2 T^{-\frac{1}{2}}. \tag{2.9}$$

Thus, at lower temperatures, the emissivity *increases* with decreasing temperature. This makes line emission a crucial feature in the analysis of spectra of low-mass galaxy groups.

X-ray data of galaxy clusters gives an excellent insight into the density and temperature distribution of the cluster. In the next two subsections this is presented in some detail.

2.4.3 Density and surface brightness profile of the ICM

The density of the X-ray emitting gas is closely related to the X-ray surface brightness of the galaxy cluster which is demonstrated here. Starting from the radial galaxy density profile (ρ_{gal}) and using the King approximation for an isothermal sphere (King 1966, 1972)

$$\rho_{\text{gal}}(r) = \rho_{\text{gal}}(0)\left(1 + \frac{r^2}{r_{\text{c}}^2}\right)^{-\frac{3}{2}}, \tag{2.10}$$

where r_{c} is the core radius. Further assuming that the gas is ideal, isothermal and in hydrostatic equilibrium, with the galaxies having an isotropic velocity dispersion, it follows (e.g. Cavaliere & Fusco-Femiano 1976; Sarazin & Bahcall 1977; Sarazin 1986)

$$\rho_{\text{gas}} \propto \rho_{\text{gal}}^{\beta}, \tag{2.11}$$

where ρ_{gas} is the gas density, and β is the ratio of energy per unit mass in galaxies to the energy per unit mass in gas

$$\beta = \frac{\mu m_{\text{p}} \sigma^2}{kT}. \tag{2.12}$$

Here μ is the mean molecular weight, m_{p} is the mass of the proton, σ is the velocity dispersion of the cluster, T is the temperature of the gas. The gas density profile can be expressed as

$$\rho_{\text{gas}}(r) = \rho_{\text{gas}}(0)\left(1 + \frac{r^2}{r_{\text{c}}^2}\right)^{-\frac{3\beta}{2}}. \tag{2.13}$$

As the gas density ρ_{gas} is proportional to the electron density n_{e} one can write

$$n_{\text{e}}(r) = n_{\text{e}}(0)\left(1 + \frac{r^2}{r_{\text{c}}^2}\right)^{-\frac{3\beta}{2}}. \tag{2.14}$$

In a soft X-ray band such as the *ROSAT* band (0.1–2.4 keV), the emissivity for plasmas does not strongly depend on temperature for ICM temperatures above 2 keV. Therefore, one can approximate the above equation for emissivity

$$\epsilon_{0.1-2.4\text{keV}} \propto n_{\text{e}}^2. \tag{2.15}$$

The surface brightness of an extended source S_X is defined as the flux (f_X) per solid angle (Ω). Hence,

$$S_X = \frac{f_X}{\Omega} \tag{2.16}$$

$$\implies S_X = \frac{L_X}{\Omega\, 4\pi D_L^2} \tag{2.17}$$

$$\implies S_X = \frac{\int_V \epsilon \, dV}{\Omega\, 4\pi D_L^2} \tag{2.18}$$

$$\implies S_X = \frac{\int_A dA \int_{-\infty}^{\infty} \epsilon \, dl}{\Omega\, 4\pi D_L^2}. \tag{2.19}$$

$$\tag{2.20}$$

Here, we assume there is no dependence of ϵ on A, and A can be expressed as $\Omega\, D_A^2$, where D_A is the angular diameter distance. The equation can now be written as

$$S_X = \frac{\Omega\, D_A^2 \int_{-\infty}^{\infty} \epsilon \, dl}{4\pi\, \Omega\, D_L^2} \tag{2.21}$$

$$\implies S_X = \frac{D_A^2 \int_{-\infty}^{\infty} \epsilon \, dl}{4\pi\, D_L^2}. \tag{2.22}$$

D_A and D_L are related to each other through the redshift z as $D_L^2 = (1+z)^4\, D_A^2$. Hence, substituting it in the above equation we get the following expression for S_X:

$$S_X = \frac{1}{4\pi\, (1+z)^4} \int_{-\infty}^{\infty} \epsilon \, dl \tag{2.23}$$

Substituting for ϵ from Eq. (2.13), we get

$$S_X \propto \int_{-\infty}^{\infty} n_e^2 \, dl \implies S_X \propto \int_{-\infty}^{\infty} \left(1 + \frac{r^2}{r_c^2}\right)^{-3\beta} dl. \tag{2.24}$$

Thus, the final expression for the surface brightness profile can be expressed as

$$S_X = S_X(0) \left(1 + \frac{R^2}{r_c^2}\right)^{-3\beta + \frac{1}{2}}, \tag{2.25}$$

where R is the projected distance from the centre of the cluster. As demonstrated, we see a clear relation between the surface brightness profile and the density profile of the cluster, and hence, a good model fit to the surface brightness profile can recover the density profile with reasonable accuracy. It must be noted that the single beta model, though a good approximation at large radii, is not very good at fitting data in the cores of the clusters. This is generally due to the presence of cooler X-ray gas in the centres which has a higher density than gas in the other regions of the cluster (Fig. 2.13).

2.4.4 Temperature distribution of the ICM

The temperature of the ICM is determined by fitting models to the observed spectra (convolved with the instrument response). Initially, the finite spatial and spectral resolution of X-ray telescopes meant

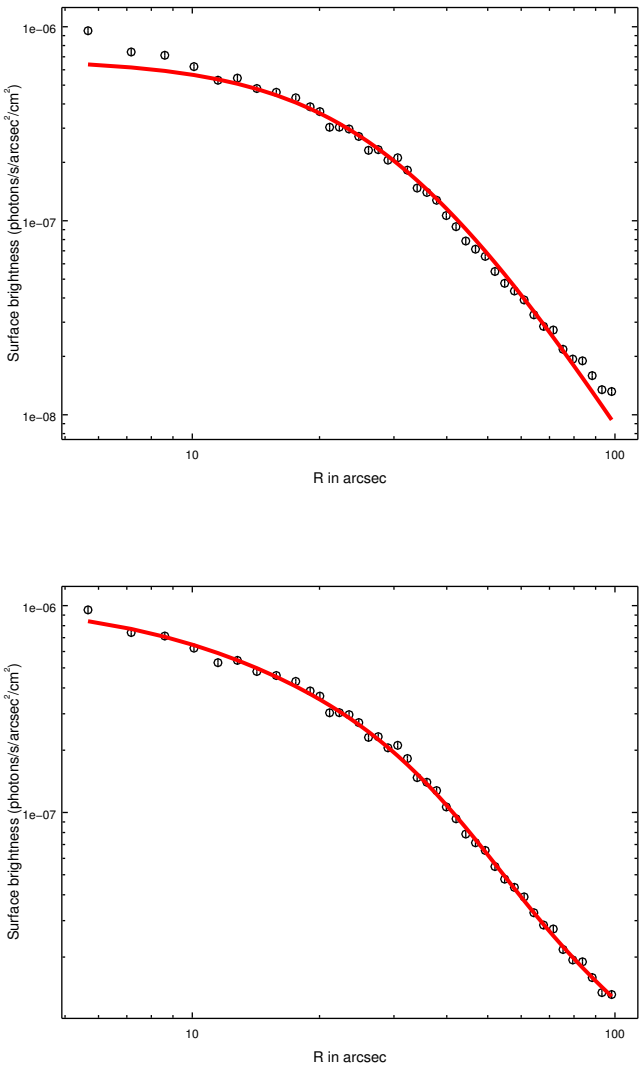

Figure 2.13: Single (top) and double (bottom) beta fits to a surface brightness profile of a galaxy cluster. The double beta model accounts for the central regions better than the single beta model and is a better description of the surface brightness distribution.

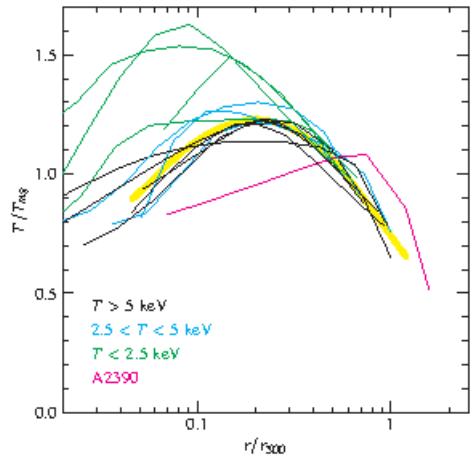

Figure 2.14: Scaled temperature profiles of galaxy clusters classified according to their temperatures. A2390 is plotted separately as the temperature profile is affected by the activity of the central AGN. From Vikhlinin et al. (2006).

that only a single temperature of the ICM could be determined, falsely identifying clusters as isothermal objects. With newer instruments such as Chandra, XMM-Newton and Suzaku, this has been proven incorrect as the temperature of clusters and groups depends on the radius. There is no "universal" temperature profile for a cluster and it is strongly dependent on various processes acting on the ICM such as AGN feedback, galactic winds, mergers etc. For centrally dense clusters with peaked surface brightness profiles (the so called cool-core clusters, Sec. 2.6), the temperature profile decreases inwards and increases outwards, ultimately flattening out or decreasing at large radii (Fig. 2.14). Low-temperature galaxy groups in general seem to show a more peaky profile than clusters (e.g. Sun 2012, Fig. 2.14).

An accurate determination of the temperature profile is important to not only understand the thermal structure of galaxy clusters, but also to determine the mass of the cluster/group using the hydrostatic equation (e.g. Fabricant et al. 1984)

$$M(< r) = -\frac{kTr}{G\mu m_{\rm p}}\left(\frac{{\rm d}\,\ln\rho_{\rm gas}}{{\rm d}\,\ln r} + \frac{{\rm d}\,\ln T}{{\rm d}\,\ln r}\right). \tag{2.26}$$

The hydrostatic equation depends on the gas density gradient, the temperature gradient, and the temperature of the ICM. Using the above equation however requires high-quality X-ray data, which in turn translates to long observations with X-ray telescopes, something that is not always available. Especially for X-ray surveys such as eROSITA, most galaxy clusters and groups will have a very low number of X-ray photons which would make a spectral and/or surface-brightness analysis difficult and even an isothermal temperature determination would be impossible (Borm et al. 2014). Hence, the use of X-ray scaling relations becomes relevant for such datasets.

2.5 X-ray scaling relations

In astronomy, scaling relations refer to a relationship between physical quantities such as luminosity, temperature, mass of an object of interest. In X-ray cluster science, these scaling relations are motivated from the self-similar model (Kaiser 1986). The theory assumes that galaxy clusters and groups form

when the matter density exceeds a certain critical density and that all clusters are relaxed and in virial equilibrium, resulting in simple power-law predictions for the scaling relations. Starting from the virial theorem, one can write the virial temperature T of a cluster as

$$T \propto M_\Delta / r_\Delta, \tag{2.27}$$

where M_Δ is the mass and r_Δ is the radius of the cluster. Δ is used to represent the mean density of a galaxy cluster calculated at a fiducial radius where the density is a multiple (typically 200 or 500) of the critical density $\rho_c = \frac{3H^2}{8\pi G}$, where H is the Hubble parameter and G is the gravitational constant. Now,

$$M_\Delta \propto r_\Delta^3. \tag{2.28}$$

Thus, combining the above two equations, we get the M–T scaling relation,

$$M \propto T^{3/2}. \tag{2.29}$$

Assuming Bremsstrahlung emission, the X-ray luminosity can be written as,

$$L_X \propto \int n_e n_i T^{1/2} \mathrm{dV}. \tag{2.30}$$

where n_i is the ion number density. Knowing that $\rho_{gas} \propto n_i \propto n_e$[4], the above equation can be simplified as,

$$L_X \propto \rho_{gas}^2 T^{1/2} r_\Delta^3 \tag{2.31}$$

$$\implies L_X \propto \rho_{gas}^2 T^{1/2} M. \tag{2.32}$$

$\rho_{gas} \propto M_{gas} r_\Delta^{-3}$ and the gas fraction $f_{gas} = M_{gas}/M$, where M_{gas} is the mass of the cluster in the ICM, and M is the total mass of the cluster. Combining these two expressions, and using the M–T relation one would get

$$L_X \propto f_{gas}^2 T^2, \tag{2.33}$$

$$L_X \propto f_{gas}^2 M^{4/3}. \tag{2.34}$$

Thus, by measuring the X-ray luminosity one can estimate the virial temperature and the total mass of the cluster. Note that L_X here is the bolometric luminosity, whereas typically, X-ray luminosities are measured in a much narrower energy band (e.g. 0.1–2.4 keV for the ROSAT all sky survey), changing the slope for the scaling relation accordingly.

Deviations of observed scaling relations from the self-similar model and the intrinsic scatter provide great insight on the various gravitational and non-gravitational processes at work in the ICM. In the next section, two such processes, namely cooling flows and feedback from AGN are presented, which is the primary focus of the science carried out in this dissertation.

[4] For sake of simplicity we assume n_e and consequently ρ_{gas} is constant here. In reality this is not true, see Sec. 2.4.3

2.6 Cooling flows, cool-cores and AGN feedback

The cooling time of the ICM can be defined as the ratio of internal energy density to the emissivity. If the internal energy density is denoted by u then the cooling time t is given by,

$$t = \frac{u}{\epsilon}. \tag{2.35}$$

The internal energy density u can be expressed as a function of the pressure P as,

$$u = \frac{3}{2}P = \frac{3}{2}(n_{\rm e} + n_{\rm i})k_{\rm B}T, \tag{2.36}$$

where $n_{\rm e}$ is the electron number density and $n_{\rm i}$ is the ion number density. For clusters with dominant Bremsstrahlung emission, $\epsilon \propto n_{\rm e}^2 T^{\frac{1}{2}}$, and the above equation can be simplified as

$$t \approx 8.5 \times\ 10^{10}\ {\rm yr}\left(\frac{n_{\rm e}}{10^{-3}\ {\rm cm}^{-3}}\right)^{-1}\left(\frac{T}{10^{8}\ {\rm K}}\right)^{\frac{1}{2}}. \tag{2.37}$$

This equation however does not strictly hold true for low-temperature plasma ($\leq$ 2 keV) due to the dominance of line emission. A generalised expression for the cooling time can be written as,

$$t = \frac{3}{2}\frac{(n_{\rm e} + n_{\rm i})k_{\rm B}T}{n_{\rm e}^2\,\Lambda(T, Z)}, \tag{2.38}$$

where $\Lambda(T, Z)$ is the so-called cooling function, which depends on temperature T and the metallicity Z of the ICM.

In low-density regions, such as cluster outskirts, the cooling time is extremely high (larger than the age of the Universe). In the centres of clusters though, the cooling times drop to much lower values (order of a few Gyr or lower) and the gas "cools" via X-ray emission. As the gas cools, it is pushed inward, towards the centre of the cluster, by the pressure of the hotter, overlying gas, generating what is termed as a "cooling flow" (Fabian et al. 1984). Thus, the centres of galaxy clusters consist of cooler gas, relative to non-central regions. This is visible in the temperature profile of the cluster, wherein "temperature drops" are observed in the central regions (Fig. 2.14). Assuming no other process, cool gas should be observed down to the lowest temperatures ($<$ 1 keV), implying that X-ray line emission should be prominently visible. The high spectral resolution of the reflection grating spectrometer (RGS) instrument on XMM-Newton however conclusively proved that the observed mass deposition rates for clusters fall short of expected rates by up to an order of magnitude (e.g. Peterson et al. 2001). Though a fraction of the cooling gas forms stars, the observed star formation rates from optical and UV data are much lower than the expected rates, making it unlikely that all of the cooling gas is fuelling star formation (e.g. McNamara & O'Connell 1989). In recent years, centrally dense galaxy clusters were accorded a new nomenclature, i.e. cool-core clusters (Molendi & Pizzolato 2001).

To explain the lack of cool gas, ICM heating via various processes were explored such as thermal conduction (e.g. Voigt & Fabian 2004), supernovae (e.g. Mathews & Brighenti 2003), and AGN feedback. In recent years, self-regulated AGN feedback has emerged as the prime heating mechanism in the cores of galaxy clusters (e.g. Churazov et al. 2002; Voit & Donahue 2005).

2.6.1 Active galactic nuclei-AGN

Active galactic nuclei (AGN) are a class of highly luminous objects (across wavelengths) located in the centres of galaxies. They are objects that are powered by matter accreting onto a supermassive black hole (SMBH). The characteristics of AGNs are as follows:

- Extremely luminous (bolometric luminosities up-to 10^{47} erg/s, e.g. Woo & Urry 2002) with most of the emission coming from a very small region (order of a parsec).
- Emission across wavelengths from radio to gamma rays.
- Variability across wavelengths.
- A small fraction of AGNs may show radio jets with superluminal motion.

Active galactic nuclei come in different forms, and are accorded different names depending on their physical and spectral characteristics. Broadly speaking, they can be classified as follows:

- Radio galaxies: These are elliptical galaxies with strong core activity and high luminosity in the radio wavelength.
- Seyfert galaxies: These are presumably spiral galaxies with core activity. There are two main sub-classifications of Seyferts, namely, type I and type II. Type I shows broad and narrow emission lines in the optical wavelength. Type II Seyferts show only narrow emission lines.
- Blazars: These are extremely bright AGNs with relativistic jets which are oriented very close to the line of sight of the observer. They are sub-classified as optically violent variables (OVVs) and BL Lacertae (BL Lacs). BL Lacs lack strong emission and absorption lines as compared to OVVs.
- Quasars: Quasi-stellar radio sources are AGNs detected in the radio wavelength with an optical point-like counterpart.
- Quasi-stellar objects (QSOs): These are similar to Quasars but are radio-quiet. The nomenclature Quasar and QSOs is used interchangeably in recent times for the most optically luminous AGNs.

In recent years, studies have indicated that the different types of AGNs are in fact similar objects all powered by a SMBH, with differences arising due to the line of sight with respect to the observer, and the differences in the Eddington ratio (Urry & Padovani 1995, Fig. 2.15).

2.6.2 AGN feedback

The ubiquity of central radio AGNs in galaxy cluster and group samples (Mittal et al. 2009; Bharadwaj et al. 2014) and their high energy outputs ($> 10^{62}$ erg, e.g. Rafferty et al. 2006) make them excellent candidates to offset ICM cooling. For the highest X-ray flux galaxy clusters sample (HIFLUGCS, Reiprich & Böhringer 2002), Mittal et al. (2009) show that all strong cool-core clusters (SCCs; with central cooling time < 1 Gyr) have a radio-loud AGN at their centres, while this decreases to 45% for non cool-core clusters (central cooling time > 7.7 Gyr) (Fig. 2.16). Additionally, an anti-correlation trend is seen between the central cooling time and the radio output of the AGN (however with high scatter for SCCs, Fig. 2.17). The details of this self-regulated AGN feedback are however not very clear to this day. Some possibilities are:

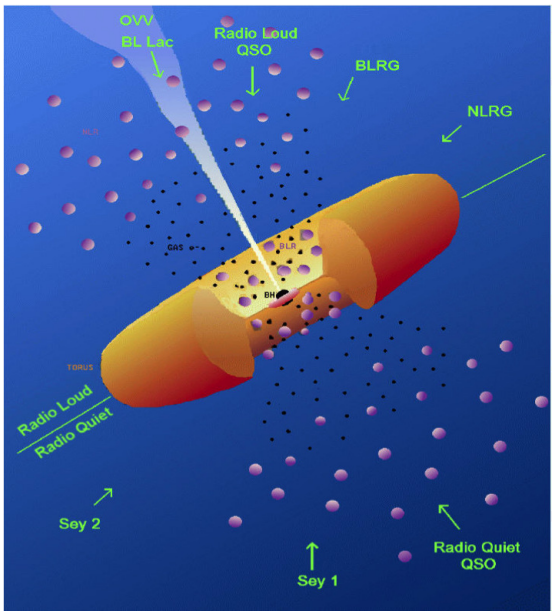

Figure 2.15: Schematic representation of the AGN unification model (Urry & Padovani 1995). The image shows that the same physical object is classified into different categories depending on how one observes them. Image credit: NASA

- Strong shock heating with very high Mach numbers (e.g. Heinz et al. 1998). These strong shocks are expected close to the centre of the SMBH and it is hard to detect them due to the limited spatial resolution of the current generation of X-ray telescopes.
- Heating through sound waves and weak shocks (e.g. Fabian et al. 2003, Fig. 2.18).
- Heating through cosmic rays injected by the SMBH (e.g. Guo & Oh 2008).
- Heat redistribution through mixing and uplifting of gas via "bubbles" (Churazov et al. 2001, Fig. 2.19).

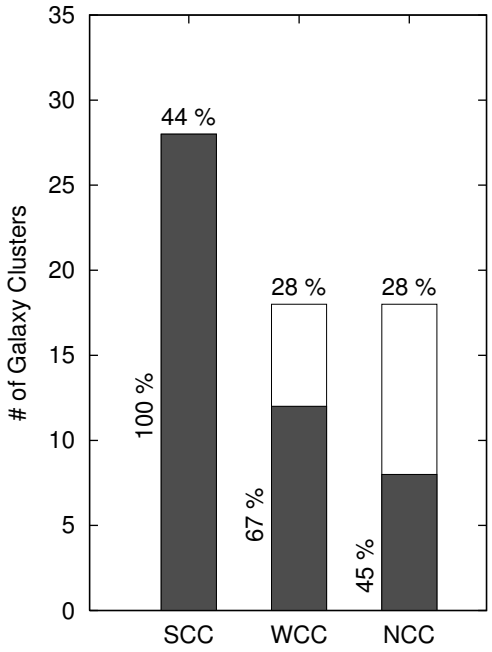

Figure 2.16: Radio loud AGN fractions in the HIFLUGCS galaxy cluster sample (Reiprich & Böhringer 2002). Shaded portion represents the AGN fraction. The clusters are divided into SCC, WCC, and NCC classes according to their central cooling time. The clusters with the shortest CCTs (the SCC class) all have a radio AGN, and this clearly drops with an increase in the CCT. From Mittal et al. (2009).

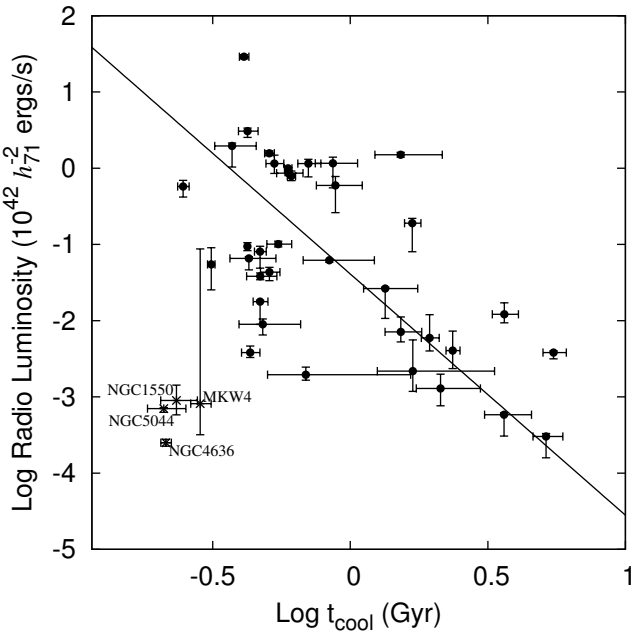

Figure 2.17: Correlation between central cooling time and the radio output of the central AGN. The labeled data points are galaxy groups which were excluded while determining the best-fit line. From Mittal et al. (2009).

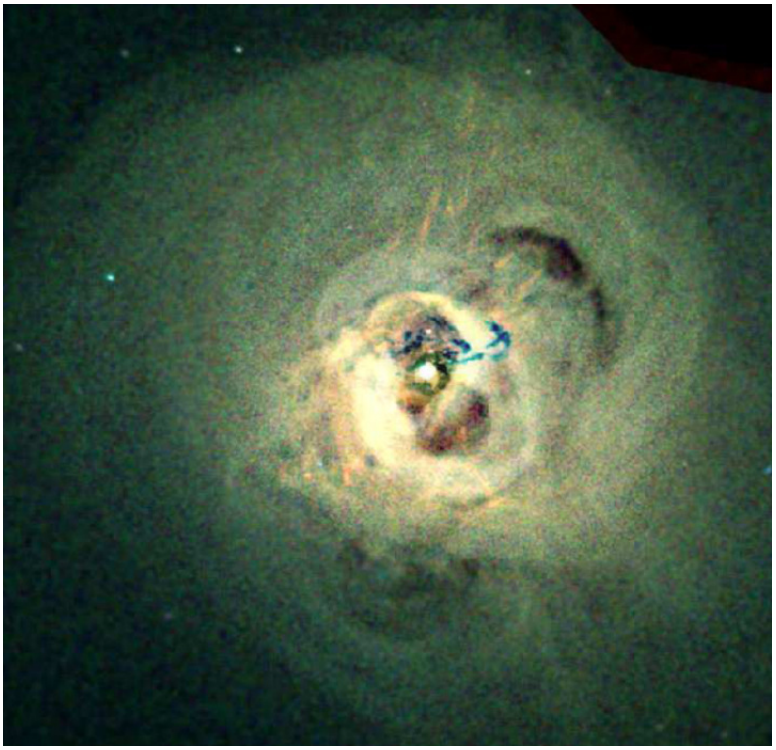

Figure 2.18: Perseus observations from Chandra telescope which shows evidence of sound waves and weak shocks. Image credit: NASA/CXC/IoA/A.Fabian et al.

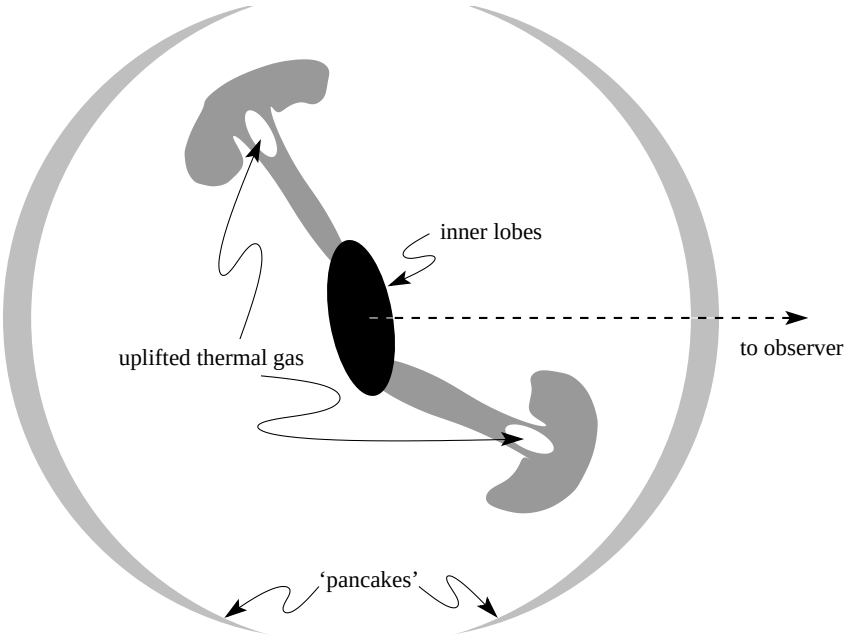

Figure 2.19: Diagrammatic representation of possible geometry of AGN feedback through rising bubbles. From Churazov et al. (2001).

CHAPTER 3

X-ray astronomy

3.1 Components of X-ray telescopes

Broadly speaking, modern X-ray telescopes consist of two components, namely mirrors and detectors. Conventional optics cannot be used for mirrors to probe the X-ray wavelength as the photons would not be reflected and simply pass through the mirror or get absorbed. This can be mitigated by the principle of grazing incidence, wherein X-ray photons can be reflected through a very small incidence angle off a metal surface and into a detector[1]. The critical angle α below which grazing incidence can be achieved is given by (Aschenbach 1985)

$$\alpha \approx 5.6\lambda\sqrt{\rho}, \tag{3.1}$$

where α is the critical angle in arcmin, λ is the wavelength in units of angstroms, and ρ is the density of the material of the reflecting surface (typically used are gold and platinum). For typical values of λ (a few angstroms), and ρ (20 g/cm^3), the critical angle is about 1 degree. To achieve grazing incidence, X-ray mirrors have to be built in specific configurations, with the Wolter type-I configuration (Fig. 3.1) being the most common one used (e.g. Chandra, XMM-Newton, ROSAT, eROSITA). Currently, most telescopes show a degradation in performance for off-axis observations, which is a considerable drawback especially for survey missions. It is expected that future X-ray missions, will use more advanced optics such as the "polynomial optics" design[2](Burrows et al. 1992) that will improve off-axis performance significantly (Conconi et al. 2010).

Detectors for X-ray satellites come in different forms such as proportional counters, microchannel plate detectors, and charge coupled devices (CCDs). Older X-ray missions such as ROSAT used proportional counters, while newer X-ray instruments, starting with the advanced satellite for cosmology and astrophysics (ASCA), use CCDs. CCDs have a higher spectral resolution (order of 100 eV) and a better spatial resolution (order of arcsecs) than proportional counters making them the ideal detector in modern X-ray instruments. In fact, the spectral resolution can be improved substantially (down to a few eV), by using gratings, though they do have the drawback of having poor spatial resolutions and low efficiencies. Micro-calorimeters such as the one on the upcoming Astro-H mission will offer a spectacular energy resolution (order of 7 eV) at moderate spatial resolution, and will be a considerable improvement over present-day gratings (Takahashi et al. 2014).

[1] A good analogy is shooting a bullet off a wall at a very narrow angle.
[2] Though for polynomial optics this would be somewhat at the expense of on-axis performance.

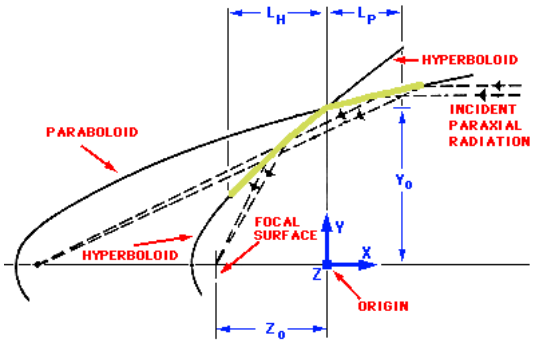

Figure 3.1: Wolter type I design used commonly in X-ray telescopes. Figure credit: http://imagine.gsfc.nasa.gov/docs/science/how_l2/xtelescopes_systems.html.

3.2 The X-ray background

While analysing X-ray data sets, particularly for galaxy clusters and groups, it is extremely important to remove unwanted background events which could impede the extraction of useful information from the source of interest. This X-ray background can be broadly divided into two categories, namely, the particle background and cosmic X-ray background (CXB). The particle background is caused by the interaction of high energy particles with the detectors, and the spectrum is characterised by fluorescence emission lines imposed on a continuum (Bartalucci et al. 2014). Subtraction of this background can be done by using observations that are not exposed to the sky (called stowed data sets for Chandra) ensuring that all the detected photons are only due to the particle background.

The CXB on the other hand, has different components which contribute to its flux and can be modelled. The different components are as follows:

- Extragalactic, unresolved X-ray sources such as AGN: The spectra of these sources can be modelled using a power law with a photon index of 1.41. This is the so-called "hard" CXB, dominating over 2 keV (e.g. Hickox & Markevitch 2006).
- Local hot bubble: This emission is galactic in origin and refers to the emission emanating from a region of the local interstellar medium (ISM) filled with hot X-ray gas (Cox & Reynolds 1987). It can be described by a thermal component with typical temperatures of 0.1 keV.
- Galactic halo emission: This background emission can also be described by a thermal component with temperatures of 0.25–0.3 keV (e.g. Snowden et al. 2008).

On a practical level, background subtraction can also be done by using "blank-sky" datasets, which are taken in regions of the sky where the emission is mostly from the CXB. This method, though popular, and sometimes the only available method for low-quality science data, does have the disadvantage of using an "averaged" sky background to account for the CXB. The more accurate method to account for the background would be to model the CXB using the spectral models described above, after subtracting the particle background from the stowed datasets.

3.3 Steps involved in X-ray data analysis

Analysing X-ray data is a challenging enterprise and several steps have to be performed to obtain useful information from the raw data. Though this section shall specifically address the steps involved in

Chandra data analysis as carried out for the science in this dissertation, broadly speaking, these steps are generally followed for data analysis of extended sources such as clusters from other telescopes as well. For all the results in this dissertation, the Chandra Interactive Analysis of Observations (CIAO) software[3] provided by the Chandra X-ray Center (CXC) was used.

3.3.1 Reprocessing event files

The data products available for scientific analysis have already undergone a basic processing before being delivered to scientists. Nevertheless, it is prudent to reprocess the data to account for e.g. changes in calibration. This particular step in Chandra data analysis was done using the `chandra_repro` task. This task corrects for charge transfer inefficiency (loss of charge as it is shifted from pixel to pixel during readout), creates an observation-specific bad pixel file[4], applies the latest calibration, and removes afterglows (residual charges in the CCDs due to cosmic ray interactions). Fig. 3.2 shows a comparison between the original events file and the reprocessed events file. For the rest of the analysis, the reprocessed events file was used.

3.3.2 Cleaning of light curves

The interaction of soft protons with the X-ray detectors result in periods of high count rates, called flares, which need to be excluded. A plot of the count rate vs. time is called a "light curve" and removing flares is called "cleaning the light curve". To perform this task for Chandra data, we used the `lc_clean` algorithm which estimates the mean count rate in a given events file and excludes time periods with too high (or too low) count rates. All light curves were also visually checked afterwards for residual flaring. Fig. 3.3 shows an example of a cleaned light curve.

3.3.3 Removing point sources

X-ray observations for extended sources are "contaminated" with many point sources (mostly AGN) which are not of interest in this work, and could affect the spectra of the object of interest. These point sources must thus be excluded before extracting spectra and surface-brightness profiles. This was done using the `wavdetect` tool which correlates potential source pixels with "Mexican hat" wavelet functions, and outputs a list of point source candidates with an elliptical region around it, that were excluded from further analysis. Fig. 3.4 shows examples of point sources detected for an observation.

3.3.4 Spectral analysis

For extracting spectra, concentric annuli were first defined by centring on the peak of X-ray emission, or the X-ray emission weighted centre, with the choice of annuli based on some criteria such as a minimum source counts threshold. Spectra were then extracted from these annular regions using the `specextract` task. Along with the spectra, for each region, two additional files were created, namely the redistribution matrix file (RMF) and the auxiliary response file (ARF). The ARF is the product of the effective area of the telescope and the detector quantum efficiency as a function of energy, and when folded with a spectrum of a source, gives the counts distribution as seen by a detector with infinite energy resolution. Detectors are of course not perfect, and have a finite resolution, which is accounted for by the RMF. Spectra were also extracted from relevant background files for background subtraction. To estimate

[3] http://cxc.harvard.edu/ciao/

[4] "bad" pixels are essentially CCD pixels which will not respond properly to incident photons due to various reasons, see http://cxc.harvard.edu/ciao/dictionary/bpix.html for details

the ICM properties, models were fit to the extracted spectra using the program *Xspec*[5]. Throughout this work, the astrophysical plasma emission code (APEC) was used, which is a model for an optically thin plasma in collisional ionisation equilibrium, with temperature, metal abundance, redshift, and the normalisation as its parameters. The redshift of all objects was always frozen to their literature values. Photoelectric absorption from the milky way also had to be accounted for, which was done by using absorption models such as *wabs* or *phabs*, with the galactic hydrogen column density (N_H) as the sole parameter. The N_H value was either taken from literature, or in some cases left as a free parameter during the spectral fit.

Depending on the project the background subtraction was performed either by using the blank-sky files, or by using the stowed files to subtract the particle background, and modelling the CXB. Note that the particle background does not remain constant with time, and therefore before the background subtraction was performed, any background file was rescaled to match the science data by comparing the count rates in the 9.5–12 keV energy band in the science and the background files. In this high energy band, the effective area of Chandra is extremely low (Fig. 3.7) and most of the recorded events are from the particle background. In case of using the blank-sky background files, the total background (particle and CXB) was automatically subtracted from the source spectra in *Xspec* and no further background treatment was performed. If only the stowed files were used, then only the particle background was automatically subtracted, and the CXB was modelled via a simultaneous spectral fit to the Chandra data and the ROSAT all-sky survey data (taken in an annulus far from the group centre). Three models were used as mentioned in Sec. 3.2; the local hot bubble emission modelled with an unabsorbed APEC model, the galactic halo emission modelled with an absorbed APEC model, and the hard X-ray background with an absorbed power law with a frozen photon index of 1.41.

3.3.5 Surface brightness analysis

As pointed out in Sec. 2.4.3, the surface brightness profile (SBP) is required for determining the density profile. Obtaining the SBP directly from the X-ray counts image of a cluster will not give an accurate description of the true surface brightness distribution due to instrumental artefacts in the image. In order to convert the counts distribution into a flux image, and remove these position and energy dependent artefacts, an exposure-correction needs to be performed. The position and movement (dithering, to smooth over pixel variations and chip gaps) of the telescope is stored in the aspect solution (telescope pointing position vs. time) which was first binned into a 3D histogram called the aspect histogram. Instrument maps, which gives the product of the mirror effective area and the quantum efficiency of the detector, were then generated and combined with the aspect histogram to generate the exposure map. The counts image was divided by this exposure map to obtain the exposure-corrected image. As the effective area of the telescope is energy dependent, 10 sub-exposure maps within our defined energy range were created, which was then used to obtain 10 exposure-corrected images, all of which were later combined into a single exposure-corrected image. This final combined image was used to obtain the SBP. Throughout this work, we obtained exposure-corrected images in an energy band of 0.5–2.0 keV, and the above steps were achieved using the `fluximage` tool. Concentric annuli centred on the X-ray peak of the exposure-corrected image were then used to obtain the SBP, background was subtracted from it, and single or double beta models were fit to it to constrain the beta-profile parameters which were later used to obtain the density profiles.

[5] http://heasarc.gsfc.nasa.gov/xanadu/xspec/

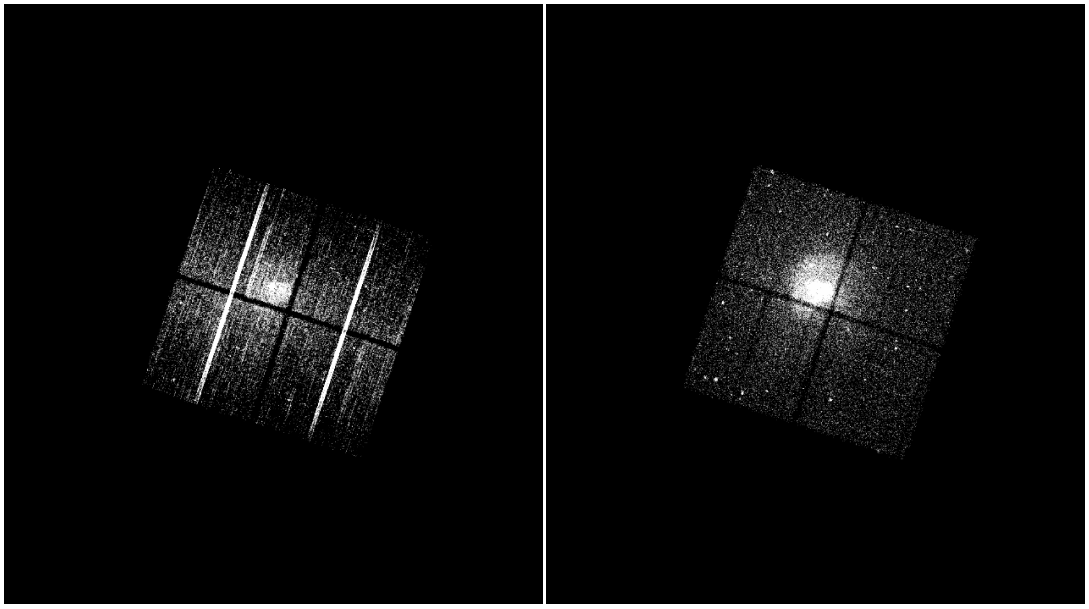

Figure 3.2: Chandra images created from events files before (left) and after reprocessing (right). The bad columns are clearly removed after the reprocessing step.

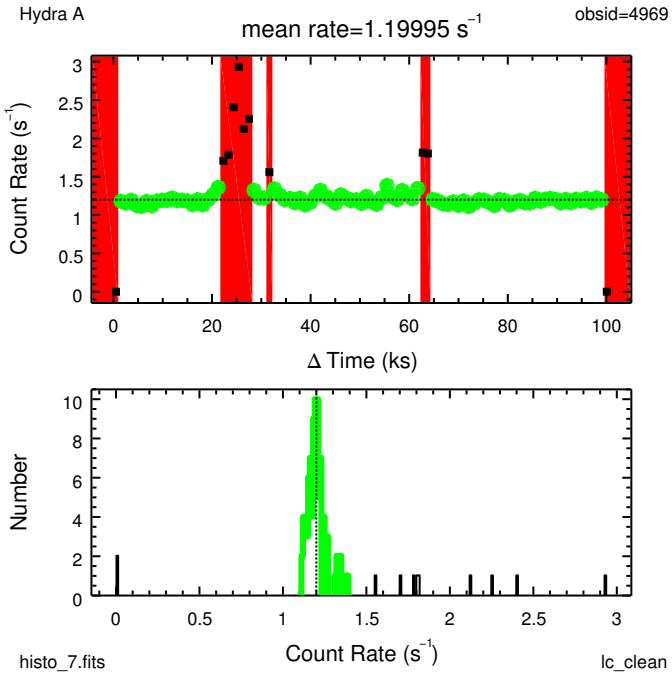

Figure 3.3: An example of cleaning a light curve. The black points in the top plot are periods which are excluded by the filtering algorithm. The bottom plot shows a histogram of the count rate values. Green points are those that are selected by the filtering algorithm. Figure credit: G. Schellenberger.

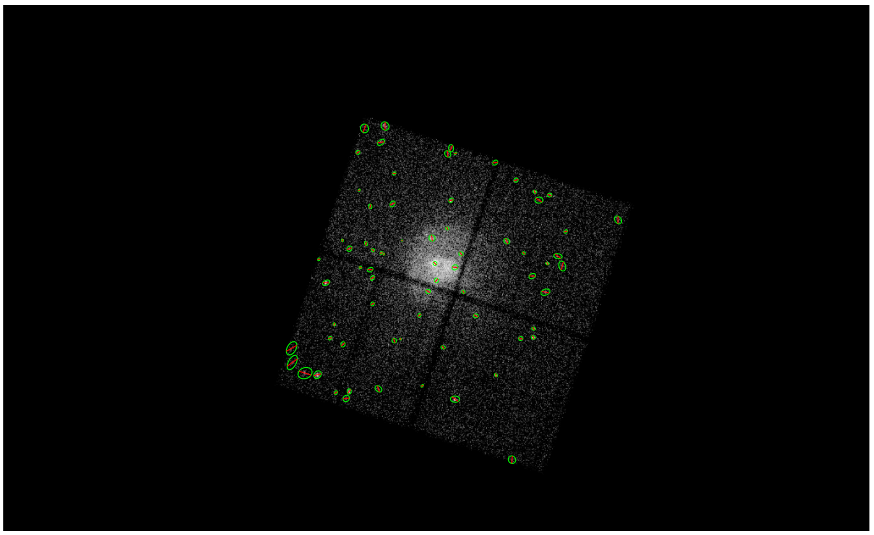

Figure 3.4: Point sources detected by the wavdetect algorithm, denoted by the green ellipses.

3.4 The Chandra X-ray telescope

Most of the scientific results presented in this dissertation were based on data from the Chandra X-ray telescope. A brief overview about this instrument is presented here, which along with the Hubble Space Telescope (HST), the Compton Gamma ray Observatory (CGRO) and the Spitzer Space Telescope (SST), made up NASA's "Great Observatories" program.

Originally called the Advanced X-ray Astrophysics Facility (AXAF), the Chandra X-ray telescope is an US-American mission which was launched in 1999. Named after Nobel laureate Subrahmanyan Chandrasekhar, the uniqueness of this telescope is its outstanding spatial resolution of 0.5 arcsec, which is unrivalled to this day for X-ray instruments. The key components of the Chandra observatory are as follows:

- The high resolution mirror assembly (HRMA).
- The advanced CCD imaging spectrometer (ACIS).
- The high resolution camera (HRC).
- The objective transmission gratings — High energy (HETG) and low energy (LETG).

Figure 3.5 shows a schematic drawing of the Chandra observatory.

3.4.1 The ACIS instrument

The Chandra instrument that was used throughout this work is the ACIS. Figure 3.6 shows a schematic drawing of the ACIS CCDs. Summarising succinctly, the ACIS CCDs are divided into two arrays, the I and S configurations with array sizes of $16.9\times$ 16.9 and $8.3\times$ 50.6 arcmin^2 respectively. The S1 and S3 chips are back-illuminated (i.e. the gate structure of the chips are facing away from the mirrors), while

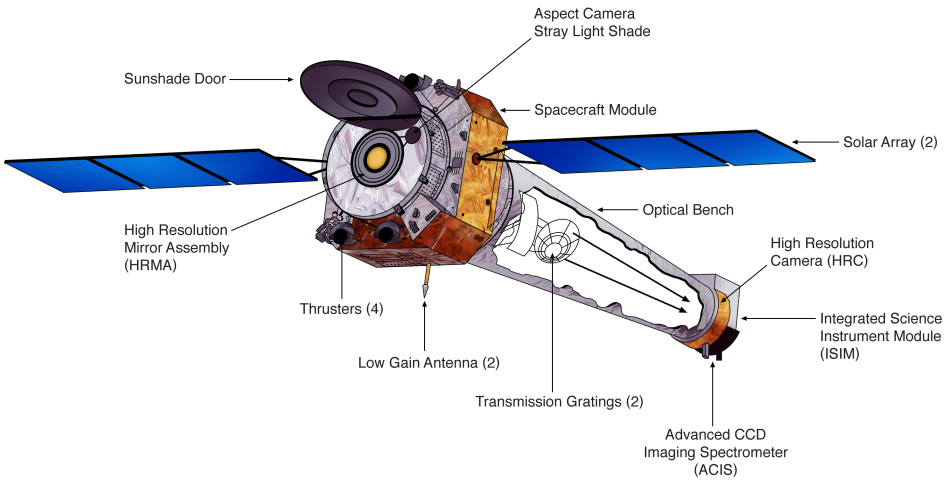

Figure 3.5: Schematic of the Chandra X-ray observatory. Figure credit: http://chandra.harvard.edu/resources/illustrations/craft_labeledD_300.jpg

the others are front-illuminated. The effective area of the HRMA combined with the ACIS is highest between 1 and 2 keV and drops drastically above 7 keV (Fig. 3.7).

3.5 The eROSITA telescope

The extended Roentgen survey with an imaging telescope array (eROSITA) is the primary instrument on board the Spectrum-Roentgen-Gamma (SRG) satellite, a German-Russian mission to be launched in 2016. eROSITA will perform only the second ever X-ray imaging all-sky survey, with the primary scientific goal of understanding the nature of dark energy using galaxy clusters (Predehl et al. 2010; Merloni et al. 2012). eROSITA will consist of seven identical Wolter-I mirror modules with each module consisting of 54 nested mirror shells (Fig. 3.8). The CCD system to be used in eROSITA will be similar to the pn-CCDs currently in use in XMM-Newton (Meidinger et al. 2011). The eROSITA all-sky survey will achieve a remarkable sensitivity (20 times greater than the ROSAT all-sky survey) unlike any other instrument before and is expected to detect 10^5 galaxy clusters and groups out to $z \sim 1$ (Pillepich et al. 2012). Moreover, it will also perform the very first imaging survey in the hard X-ray band (2-10 keV). Following the four year all-sky survey, the mission is expected to last an additional 3.5 years (at least) for pointed observations. In the pointed mode, the on-axis spatial resolution and effective area at lower energies of eROSITA are comparable to XMM-Newton with a wider field of view, making it one of the best X-ray telescopes in operation until the launch of Athena in 2028. Fig. 3.9 shows the performance of eROSITA for galaxy cluster surveys in comparison to other telescopes.

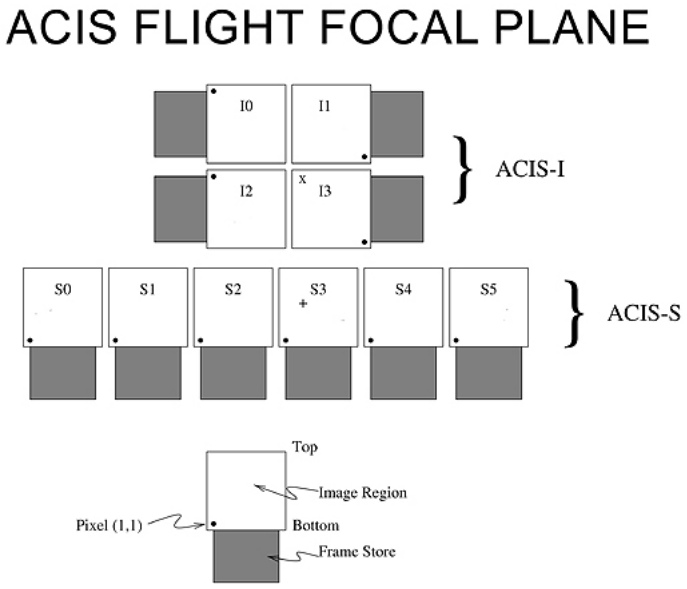

Figure 3.6: Schematic of the ACIS instrument. Figure credit: http://chandra.harvard.edu/resources/illustrations/instrumentsSchema.html

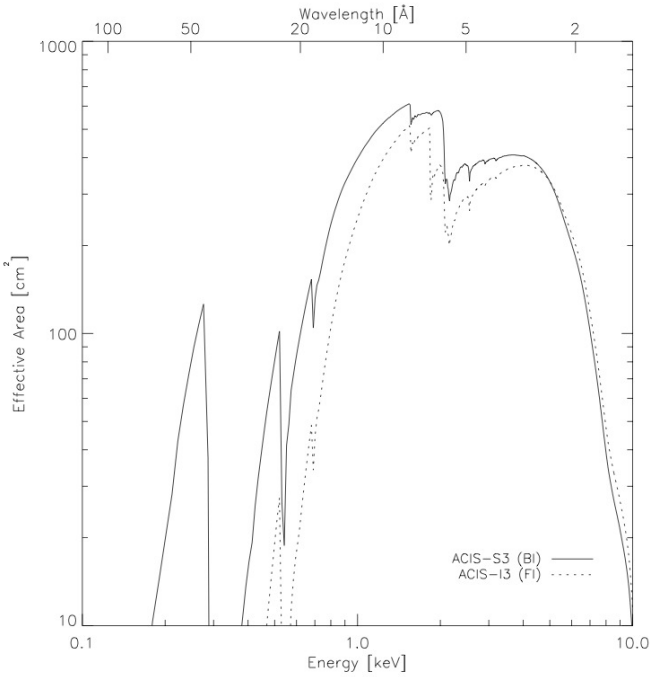

Figure 3.7: Effective area of the ACIS instrument. BI stands for back-illuminated, while FI stands for front-illuminated. Figure credit: http://cxc.harvard.edu/proposer/POG/html/chap6.html

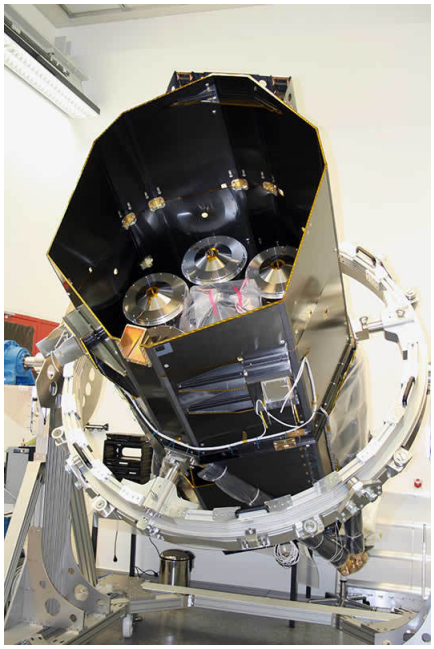

Figure 3.8: An image of the eROSITA telescope currently under construction in MPE Garching. Image credit: http://www.mpe.mpg.de/497281/mech_eRosita.

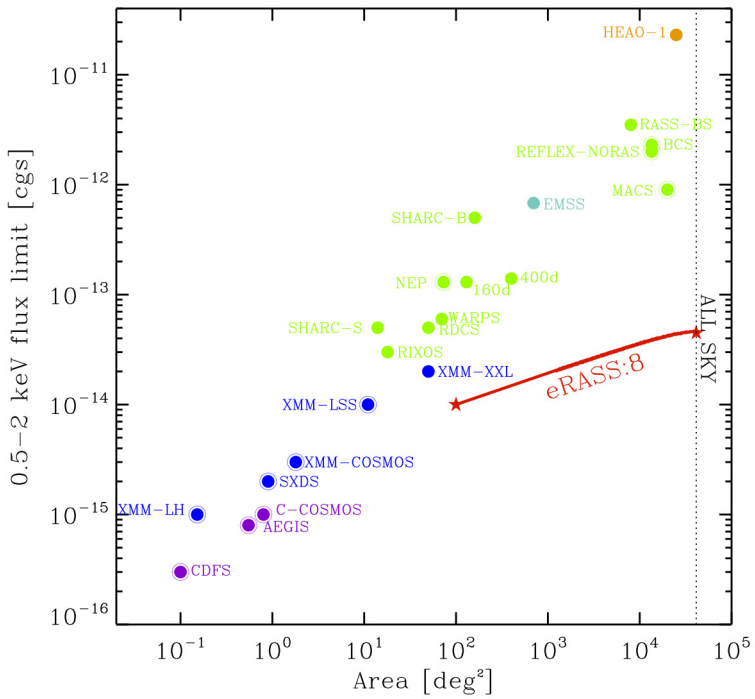

Figure 3.9: Planned eROSITA survey area vs. the cluster flux limit compared to existing surveys. Figure credit: http://www.mpe.mpg.de/455784/science.

CHAPTER 4

ICM cooling, AGN feedback and BCG properties of galaxy groups: Five properties where groups differ from clusters

This chapter was presented as a research paper in the journal Astronomy and Astrophysics, and was published in the December 2014 edition of the journal (Bharadwaj et al. 2014)[1]. Here, the interplay between the cooling of the intracluster medium, feedback from the supermassive black hole and the properties of the brightest cluster galaxy in galaxy groups is discussed. Section 4.1 gives the reader an introduction to the state of the art on the subject. Section 4.2 describes the data and analysis methods. Section 4.3 presents the results of the study which are discussed in Sec. 4.4, and a summary is presented in Sec. 4.5. The text is reproduced largely unmodified from the original article, with minor changes mostly for typographical and grammatical reasons.

4.1 Introduction

The discovery that the cooling time of the intracluster medium (ICM) in the centres of many clusters, the so-called cool-core clusters, is much shorter than the Hubble time (e.g. Lea et al. 1973; Cowie & Binney 1977; Fabian & Nulsen 1977) led to the development of the cooling flow model. In this model, as the gas cools hydrostatically, it is compressed by the hot, overlying gas, generating a cooling flow (see Fabian 1994 for a review). After early indications from the advanced satellite for cosmology and astrophysics, i.e. ASCA (e.g. Makishima et al. 2001), the high-spectral resolution data from the reflection grating spectrometer (RGS) instrument on XMM-Newton have shown that the actual mass deposition rates fall short of the predictions by an order of magnitude. These data showed that not enough cool gas was present in the cool-core clusters (e.g. Peterson et al. 2001; Xu et al. 2002; Tamura et al. 2001; Kaastra et al. 2001; I. Sakelliou et al. 2002; Peterson et al. 2003; Peterson & Fabian 2006; Sanders et al. 2008). Optical and UV data revealed the same level of discrepancy between the expected and observed star formation rates (e.g. McNamara & O'Connell 1989; Allen 1995; Edge & Frayer 2003; Rafferty et al. 2006, 2008).

Several different criteria have been used in the literature to distinguish between cool-core (CC) and non-cool-core (NCC) clusters, making it difficult to compare results. Some of the parameters used are

[1] http://www.aanda.org/articles/aa/pdf/2014/12/aa22684-13.pdf

central entropy (e.g. Voit et al. 2008, Cavagnolo et al. 2009, Rossetti et al. 2011), central temperature drop (e.g. Sanderson et al. 2006, Burns et al. 2008), classical mass deposition rate (e.g. Chen et al. 2007), and central cooling time (e.g. Hudson et al. 2010). Hudson et al. (2010) analysed 16 parameters using the HIFLUGCS sample (Reiprich & Böhringer 2002) and concluded that for low-z clusters, the central cooling time (CCT) was the best parameter to use to distinguish between CC and NCC clusters.

The classical cooling flow model does not consider any heating mechanism in addition to radiative cooling of the intracluster gas. In recent years, several models incorporating heating mechanisms have been explored, such as heating by supernovae, thermal conduction, and active galactic nuclei (AGN). Self-regulated AGN feedback has gained favor in recent years (e.g. Churazov et al. 2002; Roychowdhury et al. 2004; Voit & Donahue 2005). Excellent correlations between X-ray deficient regions in the ICM, i.e. cavities and radio lobes, have given credence to this hypothesis (e.g. Böhringer et al. 1993; McNamara et al. 2000; Blanton et al. 2001; Clarke et al. 2004; Bîrzan et al. 2004, 2008). Mittal et al. (2009) showed that the likelihood of a cluster hosting a central radio source (CRS) increases as the CCT decreases. The *exact* details of the heating mechanism through AGN are still unclear. Possibilities include heat transfer through weak shocks or sound waves (e.g. Fabian et al. 2003; Jones et al. 2002; Mathews et al. 2006), cosmic ray interaction with the ICM (Guo & Oh 2008), and the PdV work done by the expanding radio jets on the ICM (e.g. Ruszkowski et al. 2004, see also McNamara & Nulsen 2007 for a review).

Trying to understand the correlation between gas cooling in the intracluster medium (ICM)[2] and feedback processes on the galaxy group scale is fundamental to our understanding of the exact differences between clusters and groups. Galaxy groups, being systems not as massive as clusters, have long been considered scaled-down versions of clusters. The definition of a group and cluster is extremely loose and a rule of thumb definition is to designate systems comprising less than 50 galaxies as a group and above 50 as a cluster, but in recent years there has been some suggestion that groups cannot be simply treated as scaled-down versions of clusters. For example, in clusters the ICM usually dominates the baryonic budget, whereas in groups the combined mass of the member galaxies may exceed the baryonic mass in the ICM (e.g. Giodini et al. 2009). Furthermore, the main cooling mechanism in groups (line emission) differs from that in clusters (thermal bremsstrahlung). In principle, feedback from an AGN would have a greater impact on the group because of the smaller gravitational potential.

Randall et al. (2011) show that shock heating perpetuated by an AGN explosion alone is enough to balance radiative losses in the galaxy group NGC 5813. Groups such as HCG 62 (Gitti et al. 2010) show radio lobes corresponding to X-ray cavities, which could indicate that the ICM cooling/AGN feedback on the group regime is similar to that in galaxy clusters. However, as pointed out by Sun (2009), this is not so trivial and the situation is complicated even more by the presence of the so-called coronae class of kpc-sized objects representing emission from individual galaxies, likely harbouring a supermassive black hole (SMBH). Gaspari et al. (2011) argue through simulations that AGN feedback on the group regime is persistent and delicate unlike in clusters. It is worth stating here that the multitude of cool-core definitions used to define clusters and comparisons between the cool-core properties has not been thoroughly tested on the group regime with an objectively selected group sample. Thus, it becomes highly imperative to see how groups are different to clusters within the cool-core/feedback paradigm and to what extent; motivated by the basic fact that groups of galaxies are more numerous than clusters (as evident from the shape of the cluster mass function). Most of the 10^5 clusters to be detected by the upcoming eROSITA X-ray mission will be groups of galaxies or low-mass clusters (Pillepich et al. 2012). The aim of upcoming cluster missions, eROSITA in particular, is to perform precision cosmology using clusters as cosmological probes. The processes of ICM cooling and AGN feedback could easily

[2] We refrain from using the abbreviation IGM in order to avoid confusion with the intergalactic medium.

cause scaling relations to diverge from their norm (e.g. Mittal et al. 2011), which in turn could undermine their utility in cosmological applications.

The brightest cluster galaxies (BCGs) have a special role in the aforementioned paradigm. These are highly luminous galaxies, usually of giant elliptical and cD type, and are generally located quite close to the X-ray peak ($< 50h^{-1}$kpc in 88% of the cases, Hudson et al. 2010). Elliptical galaxy properties, like the optical bulge luminosity and velocity dispersion, have well defined scaling relations, allowing one to indirectly estimate the mass of the SMBH (e.g. Kormendy & Richstone 1995, Ferrarese & Merritt 2000), which may be compared to the AGN activity (e.g. Fujita & Reiprich 2004; Mittal et al. 2009). Brightest cluster galaxies also help in studying the role of cooling gas in fueling star formation where the cooling gas at least partially forms new stars (e.g. Hicks et al. 2010). Mittal et al. (2009) also allude to the possibility of different growth histories for SCC BCGs than for non-SCC BCGs. An investigation of BCGs on the group regime and comparison to cluster BCGs, factoring in the CC/NCC paradigm has not yet been carried out.

In this paper, we attempt to address several questions related to gas cooling properties, AGN feedback and BCG properties on the galaxy group scale. It is organised as follows: Section 4.2 deals with the sample selection and data analysis. Section 4.3 contains the results. A discussion of our results is carried out in Sect. 4.4. A short summary is presented in Sect. 4.5. Throughout this work, we assume a ΛCDM cosmology with $\Omega_m = 0.3$, $\Omega_\Lambda = 0.7$, and $h = 0.71$, where $H_0 = 100h$ km/s/Mpc. Correlations between different physical parameters were quantified with the help of linear regression analysis using the BCES bisector code by Akritas & Bershady (1996), and the degree of the correlations was estimated using the Spearman rank correlation coefficient. All errors are quoted at the 1σ level unless stated otherwise.

4.2 Sample selection and data analysis

4.2.1 Sample selection

The group sample used in this work is the same as used by Eckmiller et al. (2011). The main aim of that study was to test scaling relations on the galaxy group scale. The groups were selected from the following three catalogues:

- NORAS: Northern ROSAT All Sky galaxy cluster survey by Böhringer et al. (2000).
- REFLEX: ROSAT-ESO Flux Limited X-ray galaxy cluster survey by Böhringer et al. (2004).
- HIFLUGCS: Highest X-ray Flux Galaxy Cluster Sample by Reiprich & Böhringer (2002).

An upper-cut on the luminosity of $2.55 \cdot 10^{43} h_{70}^{-2}$ erg s^{-1} in the ROSAT band was applied to select only groups, and a lower redshift cut of $z > 0.01$ was applied to exclude objects too close to be observed out to a large enough projected radius in the sky. This yielded a statistically complete sample of 112 groups. However, not all of them have high-quality X-ray data, and so only those groups with Chandra observations were selected, giving a sample of 27 galaxy groups. One group, namely IC 4296 was excluded as the observations were not suitable for ICM analysis, which resulted in a final sample of 26 groups. More details about the sample are provided in Eckmiller et al. (2011).

4.2.2 Data reduction

For the data reduction we used the CIAO software package[3] in version 4.4 with CALDB 4.5.0. Following the suggestions on the Chandra Science Threads, we reprocessed the raw data (removing afterglows,

[3] http://cxc.harvard.edu/ciao

creating the bad-pixel table, applying the latest calibration) by using the `chandra_repro` task. Soft-proton flares were filtered by cleaning the lightcurve with the `lc_clean` algorithm (following the steps in the Markevitch cookbook [4]). All lightcurves were also visually inspected afterwards for any residual flaring. Point sources were detected by the `wavdetect` wavelet algorithm (the images were visually inspected to ensure that the detected point sources were reasonable) and excluded from the spectral and surface-brightness analysis. The regions used for the spectral analysis were selected by a count threshold of at least 2500 source counts and fit by an absorbed (*wabs*) APEC model, centred on the emission peak (EP), determined using the tool *fimgstat*. Table 1 gives the co-ordinates of the EP in RA/DEC. The Anders & Grevesse (1989) abundance table was used throughout.

Background subtraction

For the background subtraction we followed the steps illustrated by e.g. Zhang et al. (2009) and Sun et al. (2009) with some minor modifications.

The particle background, i.e. the highly energetic particles that interact with the detector, was estimated from stowed events files distributed within the CALDB. The astrophysical X-ray background was estimated from a simultaneous spectral fit to the Chandra data and data from the ROSAT all-sky survey (RASS) provided by Snowden's webtool[5], using the X-ray spectral fitting package *Xspec*. The components used to fit the background were an absorbed power law with a spectral index of 1.41 (unresolved AGN), an absorbed APEC model (Galactic halo emission) and an unabsorbed APEC model (Local Hot Bubble emission; see Snowden et al. 1998). The RASS data were taken from an annulus far away from the group centre, where no group emission would be present. On average we found temperatures of 0.25 keV for the Galactic halo component and 0.11 keV for the Local Hot Bubble emission.

The background for the surface-brightness analysis was estimated from the fluxes of the background models plus that from the particle background estimated from the stowed events files (weighted for each region according to the ACIS chips used, and exposure corrected with the exposure maps created for the galaxy groups in an energy range of 0.5–2.0 keV). These values were then subtracted from the surface brightness profiles (SBPs), which were also obtained from an exposure corrected image in an energy range of 0.5–2.0 keV.

4.2.3 Surface brightness profiles and density profiles

Centered on the EP, the SBP was fitted with either a single or a double β model given by

$$\Sigma = \Sigma_0 \left[1 + \left(\frac{x}{x_c}\right)^2\right]^{-3\beta+1/2} \tag{4.1}$$

or

$$\Sigma = \Sigma_{01} \left[1 + \left(\frac{x}{x_{c_1}}\right)^2\right]^{-3\beta_1+1/2} + \Sigma_{02} \left[1 + \left(\frac{x}{x_{c_2}}\right)^2\right]^{-3\beta_2+1/2}, \tag{4.2}$$

[4] http://cxc.harvard.edu/contrib/maxim/acisbg/COOKBOOK
[5] http://heasarc.gsfc.nasa.gov/cgi-bin/Tools/xraybg

respectively (Cavaliere & Fusco-Femiano 1976). Here, x_{c_i} is the core radius. The density profile for both the models is given by:

$$n = n_0 \left[1 + \left(\frac{r}{r_c}\right)^2\right]^{\frac{-3\beta}{2}}, \tag{4.3}$$

$$n = \left(n_{01}^2 \left[1 + \left(\frac{r}{r_{c_1}}\right)^2\right]^{-3\beta_1} + n_{02}^2 \left[1 + \left(\frac{r}{r_{c_2}}\right)^2\right]^{-3\beta_2}\right)^{1/2}, \tag{4.4}$$

where $n_0 = \sqrt{n_{01}^2 + n_{02}^2}$ is the central electron density and r_c is the physical core radius. The central electron density n_0 can be directly determined using the formulae (Hudson et al. 2010):

$$n_0 = \left(\frac{10^{14} 4\pi D_A D_L \zeta N}{\mathrm{EI}}\right)^{\frac{1}{2}}, \tag{4.5}$$

$$n_0 = \left[\frac{10^{14} 4\pi (\Sigma_{12}\mathrm{LI}_2 + \mathrm{LI}_1) D_A D_L \zeta N}{\Sigma_{12}\mathrm{LI}_2\mathrm{EI}_1 + \mathrm{LI}_1\mathrm{EI}_2}\right]^{\frac{1}{2}}. \tag{4.6}$$

Here, N is the normalisation of the APEC model in the innermost annulus; ζ is the ratio of electrons to protons (~ 1.2); Σ_{12} is the ratio of the central surface brightness of model-1 to model-2; D_A and D_L are the angular diameter distance and the luminosity distance, respectively; EI_i is the emission integral for model-i and is defined as

$$\mathrm{EI} = 2\pi \int_{-\infty}^{\infty}\int_{0}^{R} x \left(1 + \frac{x^2 + l^2}{x_c^2}\right)^{-3\beta} \mathrm{d}x\mathrm{d}l\,, \tag{4.7}$$

where R is the radius of the innermost annulus and LI_i is the line emission measure for model-i and is defined as

$$\mathrm{LI}_i = \int_{-\infty}^{\infty} \left(1 + \frac{l^2}{x_{c_i}^2}\right)^{-3\beta_i} \mathrm{d}l\,. \tag{4.8}$$

More details can be found in Hudson et al. (2010).

4.2.4 Cooling times and central entropies

The major focus of our work is connected to the CCT. This is calculated using the formula

$$t_{\mathrm{cool}} = \frac{3}{2}\frac{(n_e + n_i)kT}{n_e n_H \Lambda(T, Z)},$$

$$\mathrm{CCT} = t_{\mathrm{cool}}(0) = \frac{3}{2}\zeta\frac{(n_{e0} + n_{i0})kT_0}{n_{e0}^2 \Lambda(T_0, Z_0)}. \tag{4.9}$$

where n_{i0} and n_{e0} are the central ion and electron densities, respectively, and T_0 is the central temperature. We note that a bias due to different physical resolutions could be introduced arising because of different distances of the galaxy groups. Hence, we took any parameter (except the central temperature) calculated at $r = 0$ to be the value at $r = 0.004 r_{500}$. The central temperature T_0 is simply the temperature in the innermost bin in the temperature profile. As in Hudson et al. (2010), r_{500} was calculated from a

scaling relation by Evrard et al. (1996) and is given by

$$\left(\frac{r_{500}}{h_{71}^{-1}\,\mathrm{Mpc}}\right) = 2 \times \left(\frac{kT_{\mathrm{vir}}}{10\,\mathrm{keV}}\right)^{\frac{1}{2}}, \tag{4.10}$$

where the virial temperature was taken from Eckmiller et al. (2011) to calculate the r_{500}.

To ensure that the determination of the CCT is not strongly biased because of selection of annuli on the basis of a counts threshold, we performed tests for a few cases where the temperature and surface brightness annuli were increased by a factor of $\sim$ 3–4. We did not identify any strong bias that could drastically affect our results.

The central entropy K_0, another important CC parameter, is calculated as:

$$K_0 = kT_0 n_{\mathrm{e0}}^{-2/3}\,. \tag{4.11}$$

4.2.5 Radio data and analysis

All the radio data required for this work was either compiled from existing radio catalogues or literature (references in Table 4.6). We obtained data at several frequencies between 10 MHz and 15 GHz. The major catalogues used for this study were the NVSS (1.4 GHz)[6], SUMSS (843 MHz)[7], and VLSS (74 MHz)[8] catalogues.

Since this study involves radio sources associated with BCGs at the centre of the dark matter halo, it is imperative to set a criterion for whether or not a group has a central radio source. Based on the work of Edwards et al. (2007), Mittal et al. (2009) suggest that a central radio source must be located within 50 h_{71}^{-1} kpc of the X-ray peak in order for it to be categorised as a central radio source (CRS). We adopted the same criterion in this work and discovered that most CRSs lie close to the EP (within a few kpc). Appendix D shows the location of the CRS with radio contours overlaid on the optical images with the X-ray emission peak also marked for most of the groups. For CRSs with extended emission, we considered the radio emission from the lobes as well, since our goal is to obtain a correlation between the CCT and the total radio emission from the central AGN.

Radio emission by AGN is characterised by synchrotron radiation expressed as a power law relation given by $S_\nu \propto \nu^{-\alpha}$, where S_ν is the flux density at frequency ν and α is the spectral index. Much of the synchrotron emission comes from the lower frequencies ($<$ 1.4 GHz), making it highly important to obtain data on these frequency scales. Moreover, a full radio spectral energy distribution is advantageous since that allows spectral breaks and turn-overs to be discovered. Spectral breaks indicate spectral ageing and turn-overs indicate self-absorption. Self-absorption is characterized by a negative spectral index, particularly at lower frequencies. The integrated radio luminosity between a pair of frequencies ν_i and ν_{i+1} is given by

$$L_{i+1} = 4\pi D_L^2 \frac{S_0 \nu_0^{\alpha_{i+1,i}}}{1-\alpha_{i+1,i}} \left(\nu_{i+1}^{1-\alpha_{i+1,i}} - \nu_i^{1-\alpha_{i+1,i}}\right), \tag{4.12}$$

where S_0 is the flux density at either frequency $\nu_{i+1,i}$ or ν_i, $\alpha_{i+1,i}$ is the spectral index between the two frequencies, and D_{L} is the luminosity distance. To calculate the total radio luminosity between 10 MHz and 15 GHz, the spectral index at the lowest observed frequency was extrapolated to 10 MHz, and the spectral index at the highest observed frequency was extrapolated to 15 GHz. The integrated radio luminosity was then calculated as $L_{\mathrm{tot}} = \Sigma L_{\mathrm{i+1}}$. In the case of unavailability of multi-frequency data, we

[6] NRAO VLA Sky Survey-http://www.cv.nrao.edu/nvss/
[7] Sydney University Sky Survey-http://www.physics.usyd.edu.au/sifa/Main/SUMSS
[8] VLA Low frequency Sky Survey-http://lwa.nrl.navy.mil/VLSS/

assumed a spectral index of 1 throughout the energy range (e.g. Mittal et al. 2009). This had to be done for 11 CRSs in the sample. Table 4.6 summarises the radio data.

4.2.6 BCG data and analysis

For the BCG analysis, we followed the same methodology as explained in Mittal et al. (2009) and describe it here briefly.

The BCG near-infrared (NIR) K-band magnitudes ($km_{\rm ext}$) are obtained from the 2MASS Extended Source Catalog (Jarrett et al. 2000; Skrutskie et al. 2006), i.e. the XSC. Redshifts were obtained from the NASA/IPAC Extragalactic Database (NED). The magnitudes were corrected for Galactic extinction using dust maps by Schlegel et al. (1998). As these are extremely low-redshift galaxies, no k-correction was applied. The magnitudes were then converted to luminosities under the Vega system, assuming an absolute K-band solar magnitude equal to 3.32 mag (Colina & Bohlin 1997).

Studies like Marconi & Hunt (2003) and Batcheldor et al. (2007) have established well-defined scaling relations between galaxies' NIR bulge luminosity and the SMBH mass, consistent with results obtained from velocity dispersions (e.g. Tremaine et al. 2002). We use the scaling relation from Marconi & Hunt (2003) to obtain the SMBH mass,

$$\log_{10}\left(\frac{M_{\rm BH}}{M_\odot}\right) = a + b\left[\log_{10}\left(\frac{L_{\rm BCG}}{L_\odot}\right) - 10.9\right], \tag{4.13}$$

where $a = 8.21 \pm 0.07$ and $b = 1.13 \pm 0.12$. The derived SMBH mass was compared to the integrated radio luminosity. The BCG luminosities were compared to the global cluster properties, like the total X-ray luminosity $L_{\rm X}$ and mass M_{500}.

4.3 Results

4.3.1 Cool-core and non-cool-core fraction

Hudson et al. (2010) analysed 16 parameters using Kaye's Mixture Mode (KMM) algorithm as described by Ashman et al. (1994), where the CCT showed a strong trimodal distribution. Thus, the authors divided the clusters into three categories: strong cool-core (SCC) clusters with CCTs below 1 Gyr, weak cool-core (WCC) clusters with CCTs between 1 Gyr and 7.7 Gyr, and non-cool-core (NCC) clusters with CCT above 7.7 Gyr. Using the same classification system, we present our sample classified as SCC, WCC, and NCC groups in Table 4.1. This table also shows the central electron density and the central entropy (Sect. 4.3.3). The observed SCC fraction is 50%, the WCC fraction is 27%, and the NCC fraction is 23% (Fig. 4.1). A histogram showing the distribution of the CCTs is shown in Fig. 4.2.

4.3.2 Temperature profiles

The temperature profiles for all the groups, centered on the emission peak, are shown in Appendix B. We clearly see that there is no universal inner temperature profile and the magnitude of the central temperature drop, if present, varies considerably. Hudson et al. (2010) clearly showed that *all* SCC clusters had a central temperature drop, indicating the presence of a cool core. However, for our group sample, we find cases where despite extremely short cooling times, a central temperature *rise* in the innermost region is seen. This stark contrast to the properties of clusters is discussed in detail in Sect. 4.4.2.

Table 4.1: Properties of the group sample. The columns are (1) group name, (2) co-ordinates (J2000) of the EP, (3) central electron density, (4) central temperature, (5) central cooling time, (6) central entropy, (7) cool-core type, and (8) presence or absence of a central radio source.

Group name	EP (RA/DEC)	n_0 (10^{-2} cm^{-3})	T_0 keV	CCT (in Gyr)	K_0 (keVcm^2)	CC type	CRS?
A0160	01 : 12 : 59.67 + 15 : 29 : 29.11	$0.380^{+0.068}_{-0.068}$	$2.38^{+0.218}_{-0.218}$	$8.04^{+1.26}_{-1.83}$	$97.7^{+10.1}_{-13.7}$	NCC	YES
A1177	11 : 09 : 44.38 + 21 : 45 : 32.81	$0.600^{+0.130}_{-0.130}$	$1.63^{+0.08}_{-0.08}$	$3.77^{+0.67}_{-1.04}$	$49.4^{+6.05}_{-8.73}$	WCC	NO
ESO55	04 : 54 : 52.31 − 18 : 06 : 54.29	$0.760^{+0.14}_{-0.14}$	$1.88^{+0.13}_{-0.13}$	$2.70^{+0.40}_{-0.57}$	$48.6^{+5.18}_{-7.07}$	WCC	NO
HCG62	12 : 53 : 06.00 − 09 : 12 : 11.57	$3.80^{+1.23}_{-1.23}$	$0.813^{+0.008}_{-0.008}$	$0.214^{+0.0523}_{-0.1023}$	$7.19^{+1.23}_{-2.14}$	SCC	YES
HCG97	23 : 47 : 23.03 − 02 : 18 : 00.49	$1.44^{+0.19}_{-0.19}$	$0.992^{+0.015}_{-0.015}$	$0.977^{+0.114}_{-0.149}$	$16.8^{+1.33}_{-1.66}$	SCC	NO
IC1262	17 : 33 : 03.07 + 43 : 45 : 34.88	$4.12^{+0.13}_{-0.13}$	$1.63^{+0.03}_{-0.03}$	$0.504^{+0.015}_{-0.016}$	$13.7^{+0.280}_{-0.295}$	SCC	YES
IC1633	01 : 09 : 56.07 − 45 : 55 : 52.28	$0.38^{+0.0883}_{-0.0883}$	$2.82^{+0.13}_{-0.13}$	$8.20^{+1.54}_{-2.48}$	$115^{+15.1}_{-22.3}$	NCC	YES
MKW4	12 : 04 : 27.14 + 01 : 53 : 45.18	$3.91^{+0.34}_{-0.34}$	$1.57^{+0.02}_{-0.02}$	$0.258^{+0.0207}_{-0.0246}$	$13.6^{+0.737}_{-0.852}$	SCC	YES
MKW8	14 : 40 : 42.99 + 03 : 27 : 56.98	$0.34^{+0.0453}_{-0.0453}$	$3.69^{+0.18}_{-0.18}$	$10.1^{+1.19}_{-1.56}$	$163^{+13.0}_{-16.3}$	NCC	YES
NGC326	00 : 58 : 22.82 + 26 : 51 : 51.26	$0.34^{+0.079}_{-0.079}$	$1.87^{+0.09}_{-0.09}$	$7.77^{+1.46}_{-2.35}$	$82.7^{+10.8}_{-15.9}$	NCC	YES
NGC507	01 : 23 : 39.93 + 33 : 15 : 21.98	$1.09^{+0.13}_{-0.13}$	$1.22^{+0.02}_{-0.02}$	$1.22^{+0.13}_{-0.16}$	$24.8^{+1.79}_{-2.19}$	WCC	YES
NGC533	01 : 25 : 31.45 + 01 : 45 : 32.69	$4.67^{+0.68}_{-0.68}$	$0.889^{+0.011}_{-0.011}$	$0.191^{+0.0244}_{-0.0327}$	$6.85^{+0.59}_{-0.758}$	SCC	YES
NGC777	02 : 00 : 14.94 + 31 : 25 : 46.28	$4.99^{+1.17}_{-1.17}$	$1.21^{+0.05}_{-0.05}$	$0.167^{+0.0318}_{-0.0513}$	$8.92^{+1.17}_{-1.74}$	SCC	YES
NGC1132	02 : 52 : 51.81 − 01 : 16 : 28.85	$1.21^{+0.11}_{-0.11}$	$1.17^{+0.04}_{-0.04}$	$1.08^{+0.11}_{-0.09}$	$22.2^{+1.25}_{-1.46}$	WCC	YES
NGC1550	04 : 19 : 38.37 + 02 : 24 : 38.92	$5.53^{+0.35}_{-0.35}$	$1.21^{+0.007}_{-0.007}$	$0.231^{+0.014}_{-0.016}$	$8.34^{+0.334}_{-0.371}$	SCC	YES
NGC4325	12 : 23 : 06.52 + 10 : 37 : 15.52	$3.39^{+0.25}_{-0.25}$	$0.899^{+0.009}_{-0.009}$	$0.244^{+0.017}_{-0.019}$	$8.58^{+0.398}_{-0.449}$	SCC	NO
NGC4936	13 : 04 : 17.08 − 30 : 31 : 35.37	$0.620^{+0.14}_{-0.14}$	$0.949^{+0.039}_{-0.039}$	$1.54^{+0.26}_{-0.45}$	$28.1^{+3.57}_{-5.23}$	WCC	YES
NGC5129	13 : 24 : 10.08 + 13 : 58 : 37.06	$3.30^{+0.74}_{-0.74}$	$0.894^{+0.026}_{-0.026}$	$0.298^{+0.054}_{-0.086}$	$8.69^{+1.10}_{-1.60}$	SCC	YES
NGC5419	14 : 03 : 38.77 − 33 : 58 : 41.81	$0.210^{+0.086}_{-0.086}$	$2.09^{+0.097}_{-0.097}$	$13.1^{+9.16}_{-3.81}$	$127^{+26.1}_{-53.6}$	NCC	YES
NGC6269	16 : 57 : 58.01 + 27 : 51 : 15.07	$2.10^{+0.37}_{-0.37}$	$1.53^{+0.07}_{-0.07}$	$0.914^{+0.137}_{-0.197}$	$20.1^{+2.06}_{-2.77}$	SCC	YES
NGC6338	17 : 15 : 22.99 + 57 : 24 : 39.06	$5.43^{+0.36}_{-0.36}$	$1.27^{+0.02}_{-0.02}$	$0.252^{+0.0157}_{-0.0179}$	$8.86^{+0.371}_{-0.414}$	SCC	YES
NGC6482	17 : 51 : 48.81 + 23 : 04 : 18.19	$7.35^{+1.43}_{-1.43}$	$0.940^{+0.021}_{-0.021}$	$0.134^{+0.0218}_{-0.0323}$	$5.36^{+0.599}_{-0.831}$	SCC	NO
RXCJ1022	10 : 22 : 09.98 + 38 : 31 : 22.32	$0.93^{0.17}_{-0.17}$	$1.99^{+0.07}_{-0.07}$	$2.45^{+0.38}_{-0.55}$	$45.0^{+4.76}_{-6.48}$	WCC	NO
RXCJ2214	22 : 14 : 45.95 + 13 : 50 : 23.76	$1.09^{+0.23}_{-0.23}$	$1.12^{+0.05}_{-0.05}$	$1.47^{+0.39}_{-0.25}$	$22.8^{+2.73}_{-3.89}$	WCC	YES
S0463	04 : 29 : 07.54 − 53 : 49 : 39.44	$0.12^{+0.0270}_{-0.0270}$	$3.50^{+0.48}_{-0.48}$	$32.6^{+5.99}_{-9.47}$	$309^{+39.2}_{-57.4}$	NCC	YES
SS2B153	10 : 50 : 26.12 − 12 : 50 : 41.32	$7.5^{+1.29}_{-1.29}$	$0.997^{+0.012}_{-0.012}$	$0.103^{+0.0151}_{-0.0214}$	$5.61^{+0.563}_{-0.752}$	SCC	YES

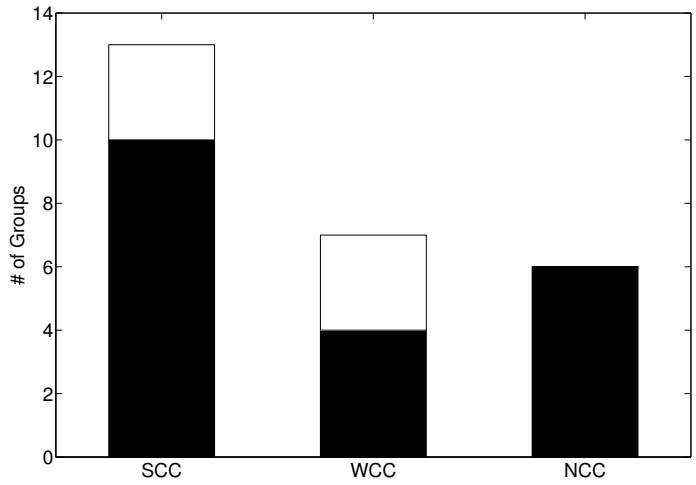

Figure 4.1: Fraction of SCC, WCC, and NCC groups. Shaded regions are groups with central radio sources (see Sect. 4.3.4)

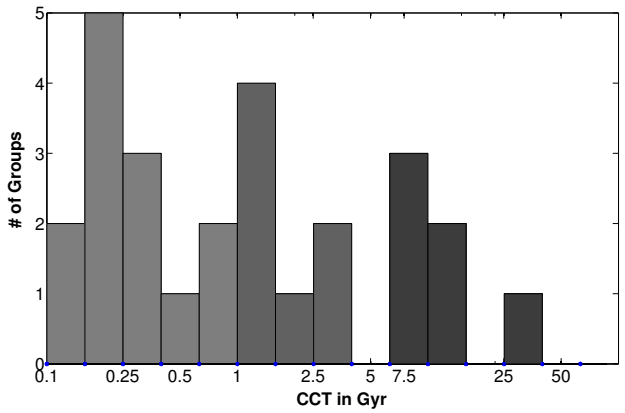

Figure 4.2: Histogram of central cooling time. The increasing shade of grey indicates increasing cooling time. Light grey represents SCC groups, medium grey is for WCC groups, and dark grey is for NCC groups.

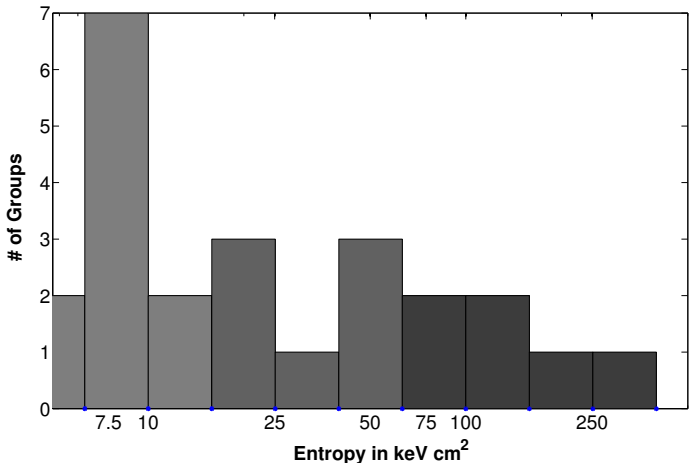

Figure 4.3: Histogram of the central entropy. Light grey represents SCC groups, medium grey represents WCC groups, dark grey represents NCC groups.

4.3.3 Central entropy K_0

The central entropy is another parameter often used to classify CC/NCC clusters (e.g. Rafferty et al. 2008) and displays a tight correlation with the CCT (Hudson et al. 2010). This is not surprising since the cooling time, $t_{\rm cool}$, is related to the gas entropy, K, through the relation $t_{\rm cool} \propto K^{3/2}/T$ for pure Bremsstrahlung. We also show a histogram of the distribution of the central entropy in Fig. 4.3. The entropy values are given in Table 4.1.

The plot of the CCT and K_0 values is shown below in Fig. 4.4. As expected, we see an excellent correlation between the two quantities with a Spearman rank correlation coefficient of 0.99, 0.99, and 0.96 for all, SCC, and non-SCC groups respectively. A CCT of 1 Gyr corresponds to $\approx$ 20 keV cm^2.

4.3.4 Radio properties

CRS fractions-CC/NCC dichotomy

Table 4.1 also lists whether or not there is a central radio source present in a group. We see that while *all* NCC groups have a CRS, the fractions of SCCs and WCCs containing a CRS are 77% and 57%, respectively. The overall CRS fraction for CC groups is 70%. Figure 4.1 shows the CRS fractions in the group sample.

Total radio luminosity vs. central cooling time

Mittal et al. (2009) show that there is an anti-correlation trend between the CCT and the total radio luminosity for CC clusters (correlation coefficient of −0.63), which breaks down for cooling times shorter than 1 Gyr.

Figure 4.5 shows the same plot for groups. We do not find indications of a trend between the two quantities. Here we show the best fit obtained for the CC clusters from Mittal et al. (2009) to highlight the difference between clusters and groups. The power-law fit for the CC clusters from Mittal et al. (2009) is given by:

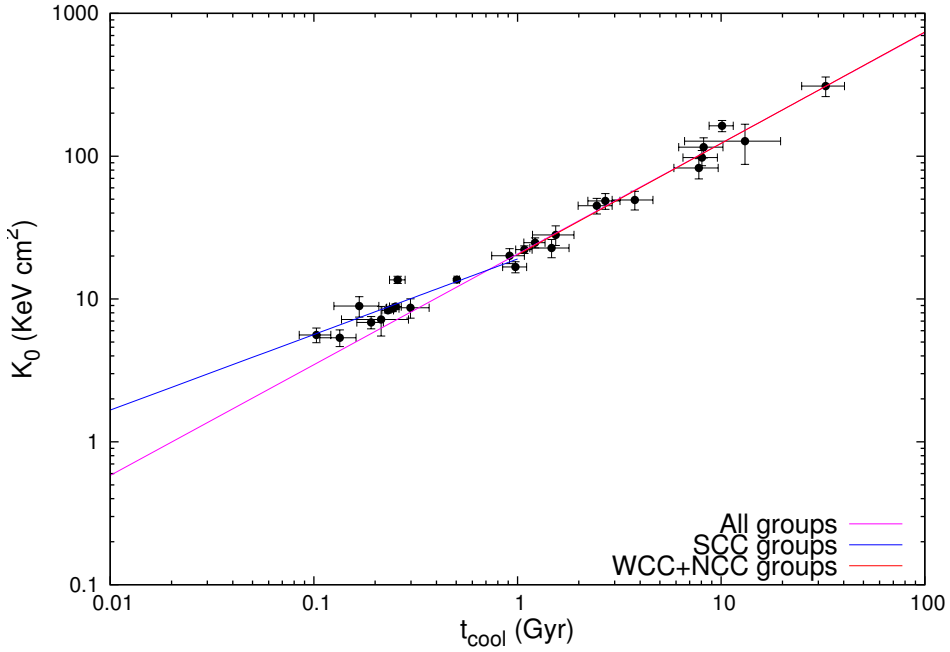

Figure 4.4: K_0 vs. CCT. Magenta is the best fit for all groups, blue for only SCC groups and red for WCC+NCC groups.

$$\left(\frac{L_{\rm tot}}{10^{42}\ h_{71}^{-2}{\rm erg\ s^{-1}}}\right) = (0.041 \pm 0.016) \times \left(\frac{t_{\rm cool}}{\rm Gyr}\right)^{-3.16\pm0.38} . \tag{4.14}$$

It is interesting to note that *all* SCC groups and most of the WCC groups show a much lower radio output than the best fit for clusters. This was first alluded to in Mittal et al. (2009), where the groups in that sample (all SCC) were clear outliers and we confirm this for the first time with a large sample of groups. We discuss this in detail in Sect. 4.4.3.

Total radio luminosity vs. SMBH mass

The total radio luminosity shows no trend with the SMBH mass (Fig. 4.5). Classifying the sample as SCC, WCC, and NCC also does not yield any discernible correlations. This is in contrast with the HIFLUGCS sample, which shows a weak correlation for the SCC clusters (correlation coefficient of 0.46). We calculate a correlation coefficient of 0.29 for all groups and 0.20 for only SCC groups. In Table 4.2 we present the mean SMBH masses and radio luminosities for the different CC types along with their standard errors to investigate whether different CC groups have systematically different masses and/or luminosities. We observe that the NCC groups have a systematically higher SMBH mass and radio luminosity than the SCC and WCC groups.

4.3.5 BCG properties

We present the scaling relation between the BCG and the cluster/group X-ray luminosity and mass in Figs. 4.6 and 4.7. The fits shown here are for a combined relation for groups and clusters. The details are summarized in Table 4.3. The derivation of the scatter is explained in Appendix A. We observe

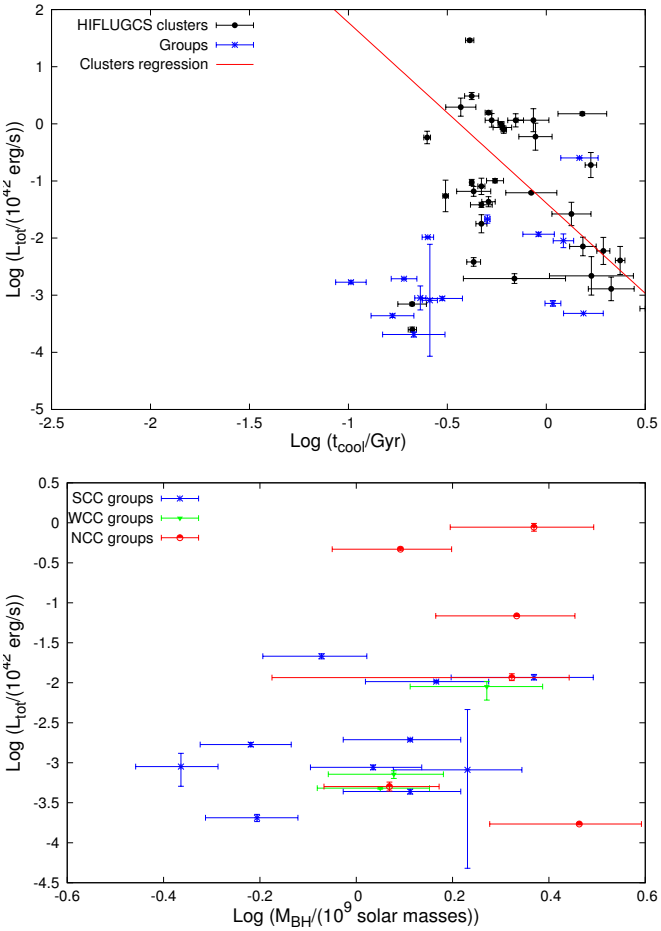

Figure 4.5: Top: Total radio luminosity vs. CCT with best-fit line for ccol-core *clusters* from Mittal et al. (2009). Bottom: Total radio luminosity vs. mass of SMBH. The blue asterisks represent SCC groups, the green triangles represent WCC groups, and the red circles represent NCC groups.

Table 4.2: Mean SMBH masses and radio luminosities for different CC groups.

Group	Mean SMBH mass (10^9 solar masses)	Mean radio luminosity (10^{42} erg/s)
SCC	1.17±0.18	0.0050±0.0023
WCC	1.39±0.24	0.0034±0.0028
NCC	1.98±0.27	0.24±0.15

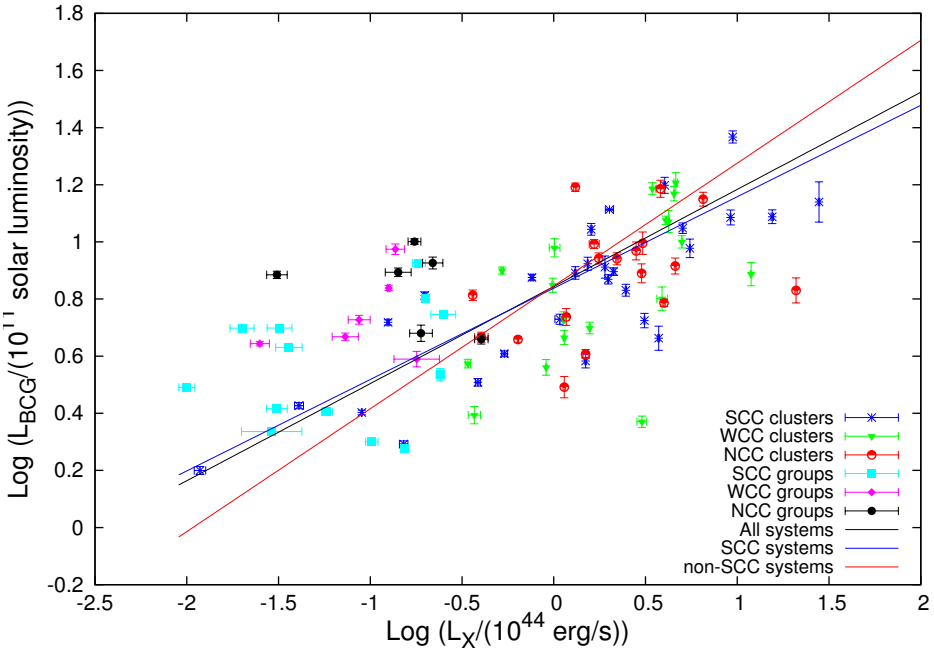

Figure 4.6: BCG luminosity vs. X-ray luminosity. The black line is the best fit for all systems, the blue line for only SCC systems, and the red line for non-SCC systems.

that most group BCGs lie above the best-fit relations. Additionally, extending the scaling relations from clusters to groups leads to a higher intrinsic scatter in most cases.

BCG luminosity vs. X-ray luminosity

Figure 4.6 shows the relation between the two quantities for both the HIFLUGCS clusters and the groups, with fits for all the members, SCC members, and non-SCC members. The correlation coefficients are 0.65, 0.79, and 0.46 for all, SCC, and non-SCC systems, respectively.

It is seen that most group BCGs have a higher luminosity than expected from the derived scaling relation. The best-fit power-law relation is given by

$$\left(\frac{L_{\rm BCG}}{10^{11}L_{\odot}}\right) = c \times \left(\frac{L_{\rm X}}{10^{44}{\rm ergs/s}}\right)^{m} , \tag{4.15}$$

where $m = 0.34 \pm 0.03$ and $c = 6.98 \pm 0.16$ for all systems, $m = 0.32 \pm 0.03$ and $c = 6.89 \pm 0.20$ for SCC systems, and $m = 0.43 \pm 0.09$ and $c = 7.01 \pm 0.30$ for non-SCC systems. We observe that when the relations are extended to the group regime, there is no significant difference in slopes and normalisations for the subsets.

BCG luminosity vs. M_{500}

Figure 4.7 shows that the luminosity of the BCG grows with the cluster/group mass. The correlation coefficients are 0.65, 0.86, and 0.44 for all, SCC, and non-SCC systems respectively. The best-fit power-

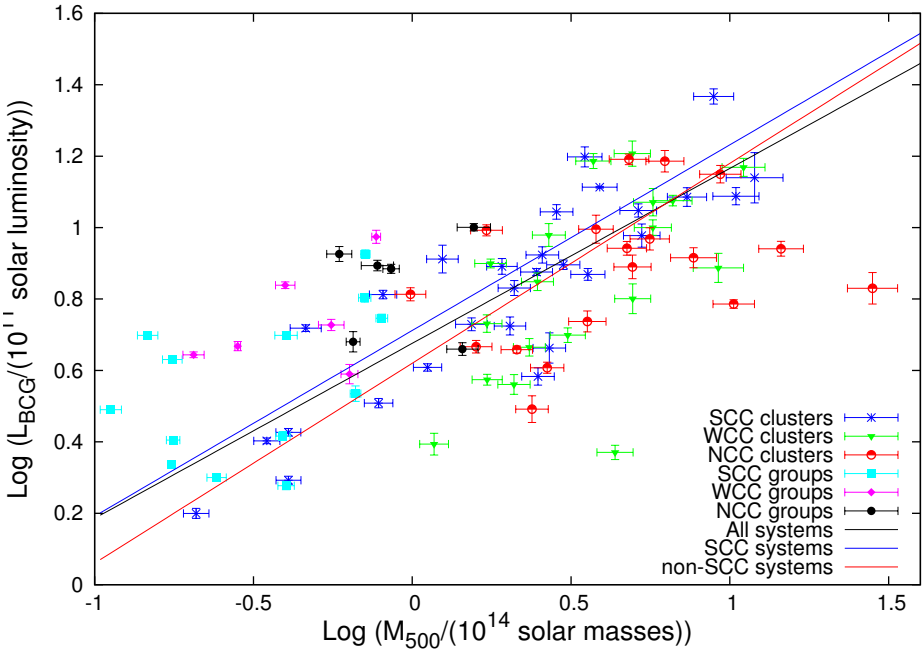

Figure 4.7: BCG luminosity vs. M_{500}. The black line is the best fit for all systems, the blue line for only SCC systems, and the red line for non-SCC systems.

law relation is given by

$$\left(\frac{L_{\rm BCG}}{10^{11}L_{\odot}}\right) = c \times \left(\frac{M_{500}}{10^{14}M_{\odot}}\right)^{m} , \tag{4.16}$$

where $m = 0.49 \pm 0.03$ and $c = 4.74 \pm 0.12$ for all systems, $m = 0.52 \pm 0.04$ and $c = 5.15 \pm 0.14$ for SCC systems, and $m = 0.56 \pm 0.08$ and $c = 4.17 \pm 0.03$ for non-SCC systems. We see that the normalisations for the SCC systems are around 23% higher than those for non-SCC systems.

The total mass M_{500} was calculated from the virial temperature (taken from Mittal et al. 2011 and Eckmiller et al. 2011 for the clusters and groups, respectively) through the scaling relation given in Finoguenov et al. (2001):

$$\left(\frac{M_{500}}{10^{13}h_{71}^{-1}M_{\odot}}\right) = (2.5 \pm 0.2)\left(\frac{kT_{\rm vir}}{1{\rm keV}}\right)^{1.676\pm0.054} . \tag{4.17}$$

4.4 Discussion of results

4.4.1 Cool-core fraction and physical properties

A comparison between the group sample and the HIFLUGCS sample with respect to cool-core fractions is presented in Table 4.4.

We notice that the observed fraction of CC groups is similar to that of clusters. It is worth recalling that the Malmquist bias results in higher observed CC cluster fractions and this should qualitatively extend to the group sample. Simulations have shown that SCC systems are selected preferentially because of their higher luminosity at a given temperature and correcting this bias reduces the fraction of SCC systems

Table 4.3: Best-fit results and scatter for BCG-cluster scaling relations: "stat" refers to statistical scatter and "int" refers to intrinsic scatter.

Category	**Slope**	**Normalisation**	$\sigma_{\mathrm{int},L_X}$	$\sigma_{\mathrm{stat},L_X}$	$\sigma_{\mathrm{int},L_{BCG}}$	$\sigma_{\mathrm{stat},L_{BCG}}$
L_X–L_{BCG} Clusters	0.36±0.03	4.54±0.34	0.67	0.07	0.24	0.03
L_X–L_{BCG} Clusters+Groups	0.34±0.03	6.98±0.16	0.85	0.08	0.21	0.03
L_X–L_{BCG} Clusters (SCC)	0.32±0.03	5.15±0.38	0.64	0.08	0.21	0.02
L_X–L_{BCG} Clusters+Groups (SCC)	0.32±0.03	6.89±0.20	0.57	0.08	0.18	0.02
L_X–L_{BCG} Clusters (NSCC)	0.50±0.07	3.49±5.09	0.61	0.06	0.21	0.03
L_X–L_{BCG} Clusters+Groups (NSCC)	0.43±0.09	7.01±0.30	0.64	0.07	0.29	0.03
			$\sigma_{\mathrm{int},M_{500}}$	$\sigma_{\mathrm{stat},M_{500}}$	$\sigma_{\mathrm{int},L_{BCG}}$	$\sigma_{\mathrm{stat},L_{BCG}}$
M_{500}–L_{BCG} Clusters	0.62±0.05	3.52±0.28	0.30	0.07	0.19	0.04
M_{500}–L_{BCG} Clusters+Groups	0.49±0.03	4.74±0.12	0.40	0.07	0.20	0.03
M_{500}–L_{BCG} Clusters (SCC)	0.62±0.01	4.30±0.29	0.21	0.07	0.13	0.04
M_{500}–L_{BCG} Clusters+Groups (SCC)	0.52±0.04	5.15±0.14	0.31	0.06	0.16	0.03
M_{500}–L_{BCG} Clusters (NSCC)	0.75±0.09	2.55±0.36	0.31	0.07	0.23	0.05
M_{500}–L_{BCG} Clusters+Groups (NSCC)	0.56±0.08	4.17±0.03	0.53	0.07	0.29	0.03

Table 4.4: Comparison between observed HIFLUGCS and group sample fractions.

Point of Distinction	**Group sample**	**HIFLUGCS**
% of CC systems (SCC+WCC)	77	72
% of SCC systems	50	44
% of WCC systems	27	28
% of NCC systems	23	28

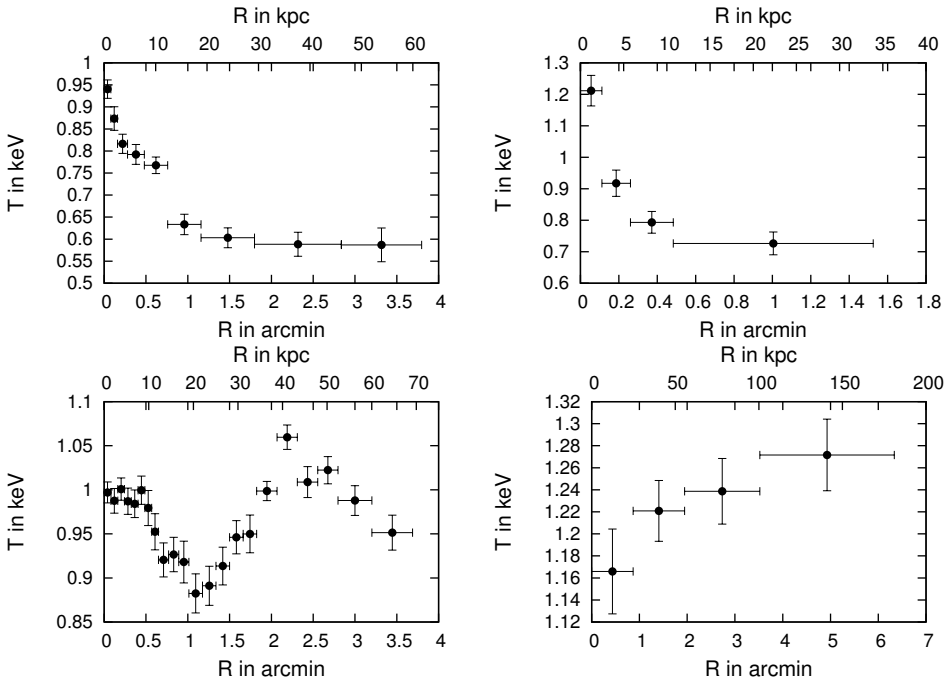

Figure 4.8: Temperature profiles for NGC 6482, NGC 777 (top, both SCC), SS2B153, and NGC 1132 (bottom, SCC and WCC, respectively).

by about 25% (Hudson et al. 2010; Mittal et al. 2011). Eckert et al. (2011) show that the CC bias due to steeper surface brightness profiles increases for less luminous systems such as groups. Additionally, as this group sample is compiled from Chandra archives, it is statistically incomplete like most other group samples, and therefore in this case could also suffer from an archival bias, possibly resulting in a preferential selection of CC objects. These biases will be quantified with access to a complete sample (e.g. Lovisari et al. 2015). Here, we conclude that there is no significant difference in SCC, WCC, and NCC fractions between clusters and groups.

The strong correlation between CCT and K_0 highlights that the central entropy may also serve as a good proxy to quantify the CC/NCC nature. Studies like Voit et al. (2008), Cavagnolo et al. (2009), and Rossetti et al. (2011) make use of the central entropy as the defining parameter for a CC system. This tight relation also ensures that systems defined by either parameter can be compared reasonably accurately for both clusters and groups.

4.4.2 Temperature profiles

A central temperature drop in the HIFLUGCS sample was a clear indication of cool gas in the centre, corroborated with short cooling times and high surface brightnesses, particularly for the SCC clusters. We find, however, that there are some SCC groups that do not have a central temperature drop, indicating the absence of cool gas; despite having centrally peaked surface brightnesses and very short cooling times. We note that adding an additional power law to the spectral fit to account for possible low-mass X-ray binary emission does not improve the quality of the fit and also does not change this behaviour of the temperature profile.

The temperature profiles of three groups that show this feature are shown in Fig. 4.8. The group NGC 6482 has been confirmed as a fossil group by Khosroshahi et al. (2004), who argue the shape

of the temperature profile could be obtained through a steady state cooling flow solution (Fabian et al. 1984), although not ruling out heating mechanisms such as supernovae or AGN, despite the lack of a clear radio source. O'Sullivan et al. (2007) argue that SS2B153 is a group whose core has been partially reheated by a currently quiescent AGN in the past, and essentially that the system is currently being observed at a stage when the effects of both heating and cooling are visible. in principle, this could also be the explanation for NGC 6482 and NGC 777.

We notice that by X-ray morphology, NGC 777 and SS2B153 are quite similar in appearance to NGC 6482, the fossil group (Fig. 4.9). In the optical band, all three systems are dominated by a bright elliptical galaxy and few other galaxies. Thus, NGC 777 and SS2B153 could also be classified as fossil groups, but we are unable to confirm this because of the lack of magnitude information. The next question that arises is if fossil groups might be a special class of systems. In the current sample, we also have NGC 1132, another confirmed fossil group (Mulchaey & Zabludoff 1999) with a CCT of 1.08 Gyr (making it a WCC, but it could be a SCC within errors), a CRS, and an almost flat temperature profile with a barely significant central temperature drop (Fig. 4.8). Thus, we speculate that fossils in general could have the features described here, i.e. a partially heated cool-core. There is at least one fossil group for which this has been shown to be the case (Sun et al. 2004). It is also worth stating here that Hess et al. (2012) show that 67% of fossil groups from their sample have CRSs. However, Démoclès et al. (2010) present fossil groups that do not show a central temperature rise. These are intriguing results that we are currently investigating with a sample of fossil groups.

Some studies, such as Sanderson et al. (2006) and Burns et al. (2008), define a CC cluster through a central temperature drop. This has never been a problem until now as it was corroborated with short CCTs and low central entropies. We have shown, however, that this may not always be the case and caution must be exercised while using the central temperature drop as a CC diagnostic, particularly on the group regime.

4.4.3 AGN activity

One of the most important conclusions of the study of the HIFLUGCS sample by Mittal et al. (2009) was that as the CCT decreases, the likelihood of a cluster hosting a CRS increases. *All* the SCC clusters contain a CRS and this fraction drops to 45% for the NCC clusters. The fraction of groups and clusters with a CRS, classified on the basis of the CCT, is shown in Table 4.5. We see that, unlike clusters, the CRS fraction in groups does not scale with decreasing CCT.

Figure 4.5 shows that almost all CC groups have a very low radio luminosity compared to CC clusters. Quantitatively, we find that the median of the radio luminosity of the CC groups is 0.169×10^{40} erg/s compared to 6.21×10^{40} erg/s for CC clusters. This is more than an order of magnitude difference between clusters and groups. Assuming that gas cooling is responsible for the radio output of the AGN, such a low value implies that not enough gas is being accreted onto the SMBH. This could simply be due to groups having less gas than clusters to accrete onto the SMBH. We note that the gas mass for clusters is also an order of magnitude higher than that for groups (Fig. 4.10), making it possible that the reason for a lower radio output for groups is simply a lack of enough cooling gas, but, we also note that the correlation between the gas mass and the radio luminosity is weak (0.43 for a combined sample of clusters and groups), raising the question whether this simple explanation is sufficient to explain the low radio output. What role does star formation play here? We discuss this in Section 4.4.5.

The correlation coefficient between SMBH mass and radio output is very low, leading one to suspect that there is no correlation between these two quantities. This correlation has always been contentious, with studies leading to conflicting results. Franceschini et al. (1998) and Lacy et al. (2001) show a correlation between L_{5GHz} and the mass of the SMBH, whereas Liu et al. (2006) show the absence of

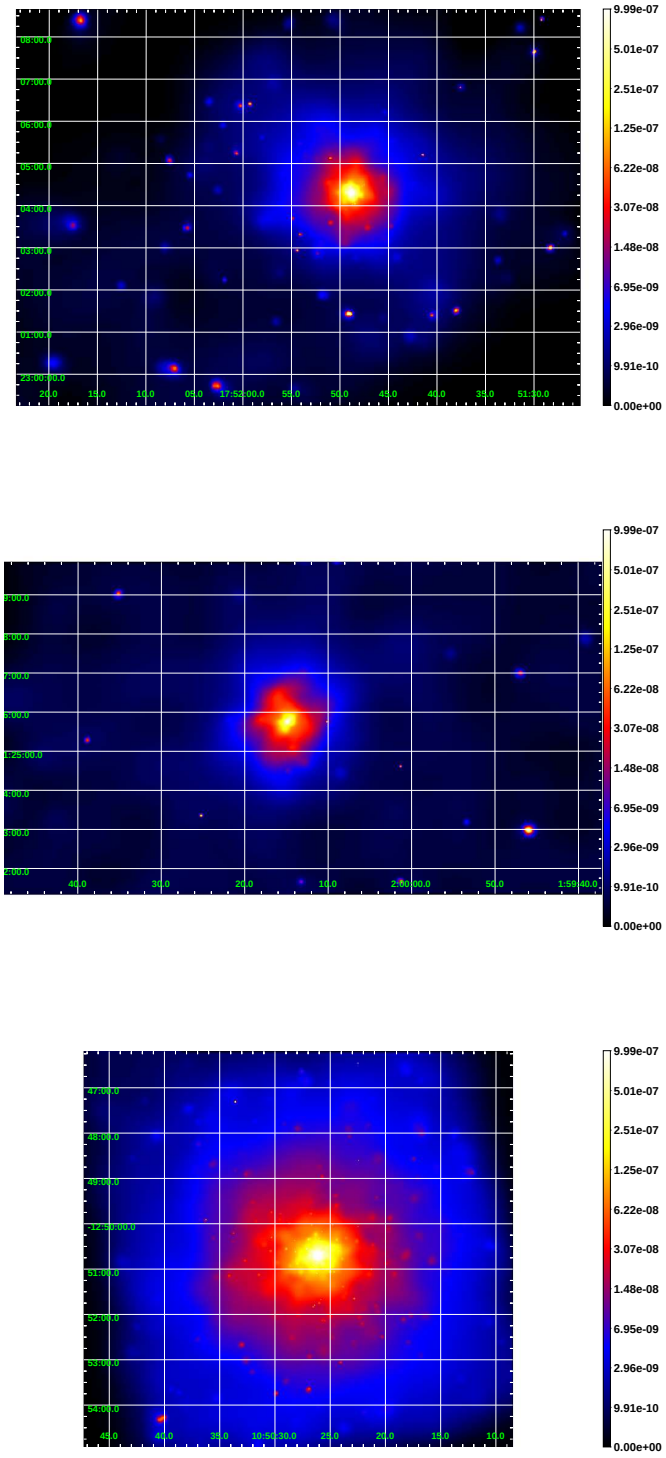

Figure 4.9: X-ray images of NGC 6482 (top), NGC 777 (middle), and SS2B153 (bottom). The images are adaptively smoothed and exposure corrected in energy bands of 0.5–2.0 keV.

Table 4.5: CRS fractions.

Point of Distinction	**Group sample**	**HIFLUGCS sample**
% of CC systems with CRS	70	75
% of NCC systems with CRS	100	45
% of WCC systems with CRS	57	67
% of SCC systems with CRS	77	100

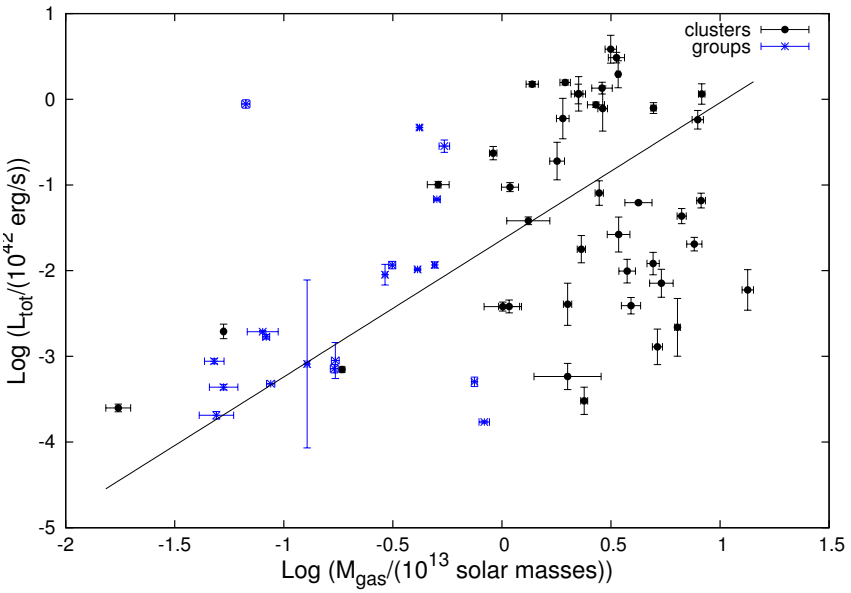

Figure 4.10: Total radio luminosity vs. gas mass. The gas masses presented here are within r_{500} and are taken from Zhang et al. (2011) and Eckmiller et al. (2011) for clusters and groups, respectively.

one. Interestingly, the NCC SMBH masses are systematically higher than the other SMBHs, raising the possibility that these objects might probably be subjected to stronger radio outbursts from larger SMBHs which might have destroyed their cool core. Though a tantalizing possibility, it could also simply be a selection effect and might have nothing to do with the CC nature of these objects.

4.4.4 BCG and cluster properties

Figures 4.6 and 4.7 show a clear trend that the BCG luminosity increases with the system mass/X-ray luminosity, but with a large amount of intrinsic scatter. Combined with the HIFLUGCS sample, there are 85 clusters and groups spanning nearly four orders of magnitude in X-ray luminosity and three orders of magnitude in cluster mass, one of the largest comparisons carried out with CC/NCC distinction. Unlike Mittal et al. (2009), who find a segregation between SCC clusters and non-SCC clusters in the M_{500}–$L_{\rm BCG}$ relation with different slopes and normalisations, a combined fit to groups and clusters does not yield statistically significant different slopes (although it does yield different observed normalisations). The higher normalisations and flatter slopes obtained by extending these relations suggest that groups in general have more luminous BCGs than clusters relative to $L_{\rm X}$ or M_{500}. Quantifying this further, we observe that $\langle \log L_{\rm BCG} - \log L_{\rm X} \rangle$ ($\langle \log L_{\rm BCG} - \log M_{500} \rangle$) is 1.7334 for groups (1.0252) vs. 0.6375 for clusters (0.3740).

To illustrate this point further, the same relations are presented again with only the fits for groups in

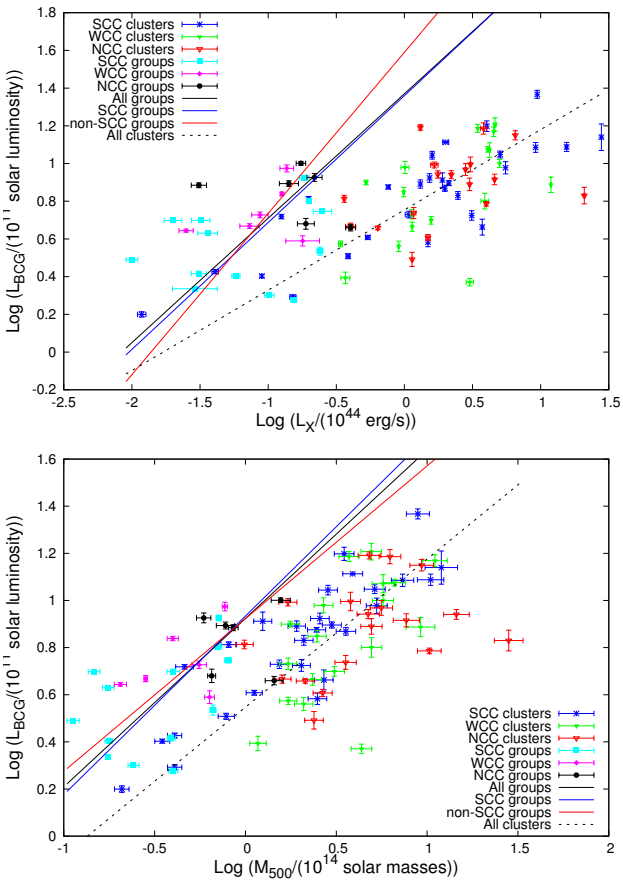

Figure 4.11: L_X–L_{BCG} and M_{500}–L_{BCG} relations. The black line is the best fit for all groups, the blue line for SCC groups, and the red line for non-SCC groups. The dotted line shows the fit for all clusters.

Fig. 4.11. For the complete group sample, the normalisation for the L_X–L_{BCG} relation increases by more than a factor of 5 (23.4 ± 15.2 vs 4.54 ± 0.34) and by more than a factor of 2 for the M_{500}–L_{BCG} relation (8.39 ± 0.80 vs 3.52 ± 0.28) compared to that for clusters only. There are also indications that the slope is steeper, but not significantly so (0.66 ± 0.27 for the L_X–L_{BCG} and 0.72 ± 0.10 for the M_{500}–L_{BCG} relation). Assuming that the NIR luminosity is a good stellar mass proxy (e.g. Bell & de Jong 2001), all the above points hint that groups have relatively more stellar mass in their BCGs than clusters.

4.4.5 The role of star formation

When trying to understand the relation between gas cooling and AGN feedback in groups, one cannot ignore the role of star formation. As pointed out by authors like Laganá et al. (2011), Lin et al. (2003), and Laganá et al. (2008), less massive cold clusters/groups are more prolific star forming environments. Rafferty et al. (2008) show that for groups and clusters, star formation kicks in when the central entropy is below 30 keV cm^2, with the requirement that the X-ray and galaxy centroids are within 20 kpc. In our sample, all our CC BCGs are within 20 kpc of the X-ray EP, and all SCC groups and a few WCC groups have a central entropy well below the entropy limit, thus fulfilling these criteria for star formation. Hicks et al. (2010) use UV data from GALEX to show that there is a good correlation between gas cooling time and star formation rate (SFR) for CC cluster BCGs, such that the SFR increases with decreasing

cooling time. Additionally, in most cases the classical mass deposition rates for our CC groups is not too high (a rough estimate yields a median of < 10 $M_\odot$/yr calculated at a radius where the cooling time is 7.7 Gyr) which means that one cannot rule out the possibility that star formation is being fueled by most of the cooling gas. This is of course a hypothesis, and confirmation of this can be provided if stronger correlations between the cooling times and star formation rates are seen for groups than for clusters. Therefore, we plan to acquire Hα data for the group BCGs to constrain SFRs.

4.5 Summary and conclusions

With a sample of 26 Chandra galaxy groups we have peformed a study of the ICM cooling, AGN feedback and the BCG properties on the galaxy group scale. The major results of our study are as follows.

- The group sample has SCC, WCC, and NCC fractions similar to the HIFLUGCS cluster sample.
- We find that 23% of the groups that have CCT $\leq$ 1 Gyr do not show a central temperature drop. We speculate that this could be due to a partial reheating of the cool core in the past. Additionally, we also speculate that this might be a characteristic feature of fossil groups.
- An increase in the CRS fraction with decreasing CCT is *not* seen, unlike for the HIFLUGCS sample. This is the first indication of differences between clusters and groups in the AGN heating/ICM cooling paradigm.
- There is no correlation seen between the CCT and the integrated radio luminosity of the CRS. We notice that CRSs for the SCC groups, in particular, have a much lower radio luminosity than clusters.
- We extend the scaling relations between $L_{\rm BCG}$ and global cluster properties ($L_{\rm X}$ and M_{500}) into the group regime. Most group BCGs have a BCG luminosity above the best fit and we think this may be due to a higher stellar mass content in group BCGs than in cluster BCGs, for a given $L_{\rm X}$ and M_{500}.
- We have speculated that star formation is a possible, effective answer to the fate of the cool gas in groups where, because of fueling star formation, not enough gas (low as it is) is being fed to the SMBH and hence the radio output of the CRSs is not as high. This could also explain why some SCC groups do not show a CRS.

In conclusion, we have demonstrated differences between clusters and groups vis-a-vis ICM cooling, AGN feedback, and BCG properties. These results lend support to the idea that groups are not simply scaled-down versions of clusters. In the future, it would be interesting to study the impact of these processes on scaling relations for galaxy groups.

Table 4.6: Radio data for CRS. The columns are (1) Cluster name, (2) Frequency, (3) Flux density at particular frequency, (4) radio luminosity at 1.4 GHz, (5) total radio luminosity, (6) whether spectral index of 1 assumed

Cluster	ν (GHz)	Flux density (mJy)	$L_{1.4\mathrm{GHz}}(10^{32}$ erg/s/Hz)	$L_{\mathrm{tot}}10^{42}$ (erg/s)	SI of 1
A0160	1.4[†] 0.408[a]	1042.8±35.7 1660±60	$0.44847^{+0.0154}_{-0.0153}$	$0.4676^{+0.0147}_{-0.0276}$	
HCG62	1.4[†]	4.9±0.5	$0.000195^{+0.00002}_{-0.00002}$	$0.000205^{+0.00002}_{-0.000021}$	YES
IC1262	1.4[†]	87.6±6.3	$0.021156^{+0.001521}_{-0.005625}$	$0.0215^{+0.0015}_{-0.0016}$	YES
IC1633	1.4[b]	1.59±0.039	$0.00015891^{+0.000005}_{-0.000005}$	$0.00017142^{+0.000005}_{-0.000005}$	YES
MKW4	1.4[c] 4.86[c]	2.40±0.5 0.35±0.1	$0.00213^{+0.000045}_{-0.000045}$	$0.000815^{+0.003810}_{-0.000767}$	
MKW8	1.4[†] 4.86[c]	2.54±0.1 2.09±0.15	$0.000402^{+0.000025}_{-0.000025}$	$0.000504^{+0.000088}_{-0.000031}$	
NGC 326	1.4[†] 0.174[♠] 0.074[‡]	1802±59 5100±510 12320±1440	$0.85239^{+0.0279}_{-0.0279}$	$0.880^{+0.095}_{-0.101}$	
NGC 507	1.4[†] 0.074[‡]	120.5±6.0 3250.0±490.0	$0.007150^{+0.000354}_{-0.000354}$	$0.008970^{+0.001430}_{-0.002890}$	
NGC 533	1.4[†]	28.6±1.0	$0.00183^{+0.00006}_{-0.00006}$	$0.00194^{+0.000069}_{-0.000066}$	YES
NGC 777	1.4[†]	7.0±0.5	$0.000413^{+0.000029}_{-0.000029}$	$0.000437^{+0.000031}_{-0.000031}$	YES

Cluster	ν (GHz)	Flux density (mJy)	$L_{1.4\mathrm{GHz}}(10^{32}$ erg/s/Hz)	$L_{\mathrm{tot}}10^{42}$ (erg/s)	SI of 1
NGC 1132	1.4†	5.4±0.6	$0.000667^{+0.00007}_{0.00007}$	$0.000717^{+0.00008}_{0.00008}$	YES
NGC 1550	1.4† 2.38[d] 0.074‡	16.6±1.6 8.0±3.0 670.0±177.0	$0.000547^{+0.000053}_{-0.000053}$	$0.00089^{+0.00015}_{-0.00004}$	
NGC 4936	1.4† 0.843♣	39.8±1.6 35.2±1.9	$0.00117^{+0.00005}_{-0.00005}$	$0.00048^{+0.00001}_{-0.00002}$	
NGC 5129	1.4†	7.2±0.5	$0.00082^{+0.00006}_{-0.00006}$	$0.00088^{+0.00006}_{-0.00006}$	YES
NGC 5419	1.4† 0.843♣ 0.074‡	349.2±12.2 529.3±16 1580±240	$0.01536^{+0.00064}_{-0.00064}$	$0.01162^{+0.00097}_{-0.00114}$	
NGC 6269	1.4† 0.074‡	50±1.9 560±100	$0.012532^{+0.00048}_{-0.00048}$	$0.01166^{+0.00079}_{-0.00104}$	
NGC 6338	1.4†	57±1.8	$0.0095806^{+0.00030}_{-0.00030}$	$0.01034^{+0.00033}_{-0.00033}$	YES
RXCJ2214	1.4†	1604.7±50.7	$0.24691^{+0.00780}_{-0.00780}$	$0.2530^{+0.0051}_{-0.0051}$	YES
S0463	0.843♣	314±9.6	-	$0.0687^{+0.0003}_{-0.0003}$	YES
SS2B153	1.4†	31.9±1.4	$0.00160^{+0.00009}_{-0.00009}$	$0.00169^{+0.00010}_{-0.00010}$	YES

† NVSS-Condon et al. (1998) ‡ VLSS-Cohen et al. (2007)
♠ 4C catalog-Pilkington & Scott (1965) ♣ SUMSS-Bock et al. (1999)
a Robertson & Roach (1990) b Hopkins et al. (2000)
c From Mittal et al. (2009), based on data from the VLA (Very Large Array) Archive
d Dressel & Condon (1978)

CHAPTER 5

Extending the L_X–T relation from clusters to groups: Impact of cool core nature, AGN feedback, and selection effects

This chapter was presented as a research paper in the journal Astronomy and Astrophyiscs and was published in the January 2015 edition of the journal (Bharadwaj et al. 2015)[1]. Here the impact of the cool-core nature, AGN feedback and selection effects on the scaling relation between the X-ray luminosity (L_X) and temperature (T) on the galaxy group regime is discussed. Section 5.1 gives an introduction to the L_X–T relation and some other relevant information. Section 5.2 discusses the sample of galaxy groups and the steps involved in constructing a bias-corrected L_X–T relation. Section 5.3 presents the results and a discussion on the scaling relation. A short summary is presented in Sec. 5.4. The text is reproduced largely unmodified from the original article, with minor changes mostly for typographical and grammatical reasons.

5.1 Introduction

A naive starting point when defining groups of galaxies is to simply call them scaled down versions of galaxy clusters. This is not entirely out of context, as the distinction between "groups" and "clusters" is quite loose and no universal definition exists in the literature. However, groups and clusters have some notable differences, such as a lack of dominance of the intracluster medium (ICM) over the galactic component (e.g. Giodini et al. 2009). Moreover, because of the shallower gravitational potential of groups, one would expect processes like active galactic nuclei (AGN) heating and galactic winds to leave stronger imprints on the group ICM than in the cluster ICM. As a result of the shape of the cluster mass function (e.g. Tinker et al. 2008, Vikhlinin et al. 2009a), most "clusters" are in fact groups of galaxies, and consequently, most galaxies in the local Universe are present in groups. The upcoming X-ray telescope eROSITA (Predehl et al. 2010) on the Spektrum-Roentgen-Gamma (SRG) mission promises to detect 10^5 clusters, most of which will be galaxy groups (Pillepich et al. 2012). Most of these systems would lack sufficient X-ray counts to be able to measure temperature and mass accurately (Borm et al. 2014), meaning an observable proxy, such as luminosity, or external constraints, such as weak lensing follow-up (Merloni et al. 2012), would have to be used to constrain these properties. In

[1] http://www.aanda.org/articles/aa/pdf/2015/01/aa24586-14.pdf

order to achieve this, the construction of robust, precise, and unbiased scaling relations using existing data gains paramount importance.

Scaling relations such as L_X–M_{tot}, L_X–T and M_{tot}–T have been well established for different samples of galaxy clusters (e.g. Allen et al. 2001; Reiprich & Böhringer 2002, Vikhlinin et al. 2006; see Giodini et al. 2013 for a review). The validity of cluster scaling relations on the group scale has led to conflicting viewpoints, with Ponman et al. (1996) suggesting variations for galaxy groups, and e.g. Sun et al. (2009) refuting any discrepancy between clusters and groups. Eckmiller et al. (2011) show that there is a good agreement between clusters and groups for most scaling relations, albeit with increased intrinsic scatter on the group regime, which is not totally unexpected due to the complicated baryonic physics at play in low-mass systems. Recent results by Lovisari et al. (2015), however, argue that while the *observed* scaling relations for galaxy groups are in agreement with those obtained for galaxy clusters, the scaling relation obtained after corrections for selection effects are consistent with a gradual steepening towards the low-mass regime.

The L_X–T relation is one of the most contentious scaling relations. Self-similarity predicts that the bolometric L_X is proportional to T^2 (e.g. Eke et al. 1998) for clusters, but observations constrain a much steeper slope (e.g. Arnaud & Evrard 1999). Moreover, as compared to other scaling relations, the intrinsic scatter is also much larger (e.g. Pratt et al. 2009). A major contribution to the scatter in the scaling relation is the cooling gas in the cores of clusters, as shown by e.g. O'Hara et al. (2006). Mittal et al. (2011) in particular demonstrate that excising the core regions reduce the scatter in the L_X–T relation by 27%, additionally stating that cool cores cannot be the sole contributor to the scatter. They also speculate that while ICM cooling dominates the cluster regime, AGN feedback could have a greater effect on the scaling relation in groups, mainly due to the shallower gravitational potential of these systems.

This paper is the first systematic attempt to determine bolometric L_X–T relations to account for both the presence/absence of a strong cool-core and the presence/absence of a central radio loud AGN in galaxy groups. Additionally, we construct a bias-corrected bolometric L_X–T relation to objectively compare groups and clusters of galaxies for the first time. The overarching theme of this paper is to understand the impact of non-gravitational processes and the selection effects on the L_X–T relation.

A ΛCDM cosmology with $\Omega_m = 0.27$, $\Omega_\Lambda = 0.73$ and $h = 0.71$ where $H_0 = 100h$ km/s/Mpc is assumed throughout the paper, unless stated otherwise. All errors are quoted at the 68% level unless stated otherwise. Log is always base 10 here.

5.2 Data and analysis

5.2.1 Sample and previous work

We describe briefly the sample and methods that were used for this study. Detailed explanations about the sample and the data reduction can be found in Eckmiller et al. (2011) and Bharadwaj et al. (2014), respectively.

The sample of galaxy groups was compiled by Eckmiller et al. (2011) from three X-ray catalogues based on the ROSAT All-Sky Survey (RASS) in order to test scaling relations on the group regime. Essentially, an upper luminosity cut of $2.55 \times 10^{43} h_{70}^{-2}$erg s^{-1} and a lower redshift cut of 0.01 was applied to the northern ROSAT all-sky survey galaxy cluster survey (NORAS) catalogue (Böhringer et al. 2000), ROSAT-ESO flux-limited X-ray galaxy cluster survey (REFLEX) catalogue (Böhringer et al. 2004), and highest X-ray flux galaxy clusters (HIFLUGCS) (Reiprich & Böhringer 2002) to select a statistically complete sample from which a sub-sample of groups with Chandra data were used for analysis. In the end, 26 objects were used for testing scaling relations.

In a follow-up study, Bharadwaj et al. (2014) investigated the cores of these galaxy groups by determining the temperatures and densities to constrain their cool-core properties such as central cooling time (CCT) and central entropy. Using the CCT as the parameter of distinction, the sample was divided into the strong cool core (SCC with CCT < 1 Gyr), weak cool core (WCC with 1 Gyr ≤ CCT < 7.7 Gyr), and non-cool core (NCC with CCT ≥ 7.7 Gyr) classes, where the CCT was determined at $0.4\%r_{500}$, consistent with the work of Hudson et al. (2010) for the HIFLUGCS clusters. The fractions of SCC, WCC, and NCC groups were found to be similar to that of clusters. Using radio catalogue data, the presence of central radio sources (CRS) was identified and the radio output, which is a measure of the AGN activity, was determined. Furthermore, with the help of near-infrared data from the 2MASS XSC catalogue (Jarrett et al. 2000; Skrutskie et al. 2006), the brightest cluster galaxy (BCG) was also studied and linked to the ICM cooling and AGN heating, to give a complete picture of the cores of galaxy groups. When the results for the groups were compared to that of clusters, five important differences were identified, e.g. groups do not follow the trend of clusters to exhibit a higher AGN fraction with decreasing CCT.

5.2.2 Temperatures and luminosities

The data reduction in this work was performed using CIAO 4.4 with CALDB 4.5.0. The `chandra_repro` task was used to reprocess the raw data set and create a new level 2 event file. The `lc_clean` routine was used to filter out soft-proton flares. Point sources were detected and excluded using the `wavdetect` wavelet algorithm. These steps were exactly the same as was implemented in Bharadwaj et al. (2014). We extracted spectra in a single annulus centred on the emission weighted centre, excluding the core regions using the radii stated in Eckmiller et al. 2011, i.e. central region with a cooler temperature component indicated by a central temperature drop in the temperature profile, to get a core-excised temperature and to prevent biasing the temperature estimation to a lower value.

The background treatment was performed as in Bharadwaj et al. (2014). The particle background was estimated using the stowed events files distributed within the CALDB. For the astrophysical background, we performed a simultaneous spectral fit to the Chandra data and the RASS data (provided by Snowden's webtool[2]). The background components were an absorbed power law with a spectral index of 1.41 for unresolved AGN, an absorbed astrophysical plasma emission code (APEC) model for Galactic halo emission, and an unabsorbed APEC model for Local Hot Bubble emission (Snowden et al. 1998). The RASS data were taken from an annulus far away from the group centre, where no group emission would be present. The group emission was modelled with an absorbed APEC model, with the temperature and abundance free to vary. All absorption components were linked and modelled with the *phabs* model, and $N_{\rm H}$ values were taken from a webtool[3], which follows the method described in Willingale et al. (2013). In some cases, these were found to be too low, and they were left as free parameters in the spectral fit. This has the effect of lowering the temperatures, with the largest change being of the order of 6%. The Anders & Grevesse (1989) abundance table and AtomDB 2.0.2 was used throughout. Since we wished to study the bolometric $L_{\rm X}$–T relation, we had to convert the quoted ROSAT (0.1–2.4 keV) luminosities in Eckmiller et al. (2011) to the bolometric band (0.01–40 keV), for which we used the program *Xspec*. Using an APEC model frozen to the best-fit temperature, abundance, and redshift for the groups, we calculated the luminosities in the ROSAT band and the bolometric band. The ratio of the ROSAT and bolometric $L_{\rm X}$ gives us the conversion factor to transform between the two luminosities. This conversion factor largely depends on the temperature and slightly on the abundance of the ICM (Fig. 5.1). Given that most groups from the eROSITA all-sky survey would likely lack sufficient counts

[2] http://heasarc.gsfc.nasa.gov/cgi-bin/Tools/xraybg
[3] http://www.swift.ac.uk/analysis/nhtot/index.php

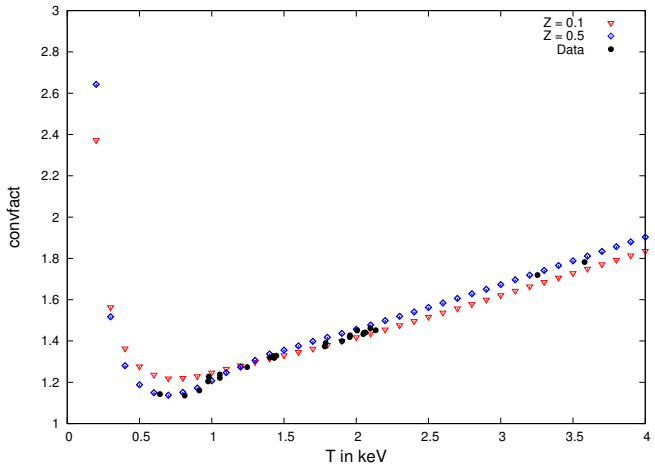

Figure 5.1: Plot of conversion factor between ROSAT and bolometric luminosities as a function of temperature. Red triangles are for metallicity of 0.1, blue diamonds are for metallicity of 0.5, black points represent the actual conversion factors used for the sample.

to resolve the core, we did not use core-excised luminosities. The temperatures, luminosities, and $N_{\rm H}$ values are listed in Table 5.1.

For getting the slope and normalisation of the best-fit scaling relation, we used the bivariate correlated errors and intrinsic scatter (BCES) (Y|X) code by Akritas & Bershady (1996). The fits were performed in log space for the fitting function:

$$\left(\frac{L_{\rm X}}{0.5\times10^{44}\ {\rm erg\ s^{-1}}}\right) = c\times\left(\frac{T}{3\ {\rm keV}}\right)^{m}. \tag{5.1}$$

We also calculated statistical ("stat"), total ("tot"), and intrinsic ("int") scatters with the following formulae[4]:

$$\sigma^{T}_{\rm stat} = \langle \log({\rm e})\cdot \Delta T/T\rangle, \tag{5.2}$$
$$\sigma^{L_{\rm X}}_{\rm stat} = \langle \log({\rm e})\cdot \Delta L_{\rm X}/L_{\rm X}\rangle, \tag{5.3}$$
$$\sigma^{T}_{\rm tot} = \left\langle (\log T - (\log L_{\rm X} - \log c)/m)^2\right\rangle^{1/2}, \tag{5.4}$$
$$\sigma^{L_{\rm X}}_{\rm tot} = \left\langle (\log L_{\rm X} - (m\cdot\log T + \log c))^2\right\rangle^{1/2}, \tag{5.5}$$
$$\sigma^{T}_{\rm int} = \left((\sigma^{T}_{\rm tot})^2 - (\sigma^{T}_{\rm stat})^2 - m^{-2}\cdot(\sigma^{L_{\rm X}}_{\rm stat})^2\right)^{1/2}, \tag{5.6}$$
$$\sigma^{L_{\rm X}}_{\rm int} = \left((\sigma^{L_{\rm X}}_{\rm tot})^2 - (\sigma^{L_{\rm X}}_{\rm stat})^2 - m^{2}\cdot(\sigma^{T}_{\rm stat})^2\right)^{1/2}. \tag{5.7}$$

The fits were performed for five different cases, which are presented in Table 5.2. To test the effects of ICM cooling on the relation, we sub-divided the sample into the SCC and non-strong cool core (NSCC; CCT $\geq$ 1 Gyr) cases. To test the effects of AGN feedback, we classified the systems as those with and without a central radio source (CRS and NCRS respectively), a CRS representative of the presence of a radio loud AGN.

[4] In log space, errors are expressed as $\Delta \log x = \log(e)\ (x^{+} - x^{-})/(2x)$ where x^{+} and x^{-} are the upper and lower boundary of the error range of the quantity x

Table 5.1: Temperatures, bolometric luminosities, and $N_{\rm H}$ for the galaxy groups. Starred entries represent fitted values for $N_{\rm H}$.

Group name	T keV	$L_{\rm X}$ 10^{43} erg/s	$N_{\rm H}10^{21}$ cm^{-2}
A0160	$1.90^{+0.09}_{-0.09}$	$2.69^{+0.38}_{-0.38}$	0.516
A1177	$1.79^{+0.07}_{-0.07}$	$1.22^{+0.17}_{-0.17}$	0.117
ESO55	$2.10^{+0.05}_{-0.07}$	$2.02^{+0.24}_{-0.24}$	1.02*
HCG62	$1.43^{+0.04}_{-0.05}$	$0.399^{+0.053}_{-0.053}$	1.03*
HCG97	$0.98^{+0.02}_{-0.02}$	$0.358^{+0.139}_{-0.139}$	1.56*
IC1262	$1.95^{+0.04}_{-0.05}$	$3.42^{+0.17}_{-0.17}$	0.416*
IC1633	$3.58^{+0.14}_{-0.14}$	$3.10^{+0.25}_{-0.25}$	0.200
MKW4	$2.01^{+0.03}_{-0.03}$	$2.86^{+0.05}_{-0.05}$	0.534*
MKW8	$3.25^{+0.08}_{-0.08}$	$6.92^{+0.58}_{-0.58}$	0.269
NGC326	$2.06^{+0.08}_{-0.09}$	$3.22^{+0.42}_{-0.42}$	1.07*
NGC507	$1.45^{+0.02}_{-0.02}$	$1.67^{+0.02}_{-0.02}$	0.638
NGC533	$1.43^{+0.04}_{-0.04}$	$0.413^{+0.066}_{-0.066}$	0.331
NGC777	$0.81^{+0.02}_{-0.02}$	$0.232^{+0.032}_{-0.032}$	0.570
NGC1132	$1.25^{+0.01}_{-0.01}$	$0.929^{+0.150}_{-0.150}$	0.556
NGC1550	$1.40^{+0.01}_{-0.01}$	$2.00^{+0.11}_{-0.11}$	1.62
NGC4325	$1.06^{+0.01}_{-0.01}$	$1.25^{+0.10}_{-0.10}$	1.41*
NGC4936	$0.97^{+0.01}_{-0.02}$	$0.293^{+0.040}_{-0.040}$	0.882
NGC5129	$1.05^{+0.01}_{-0.01}$	$0.445^{+0.076}_{-0.076}$	0.186
NGC5419	$1.96^{+0.12}_{-0.15}$	$0.444^{+0.064}_{-0.064}$	1.44*
NGC6269	$2.05^{+0.10}_{-0.12}$	$2.66^{+0.22}_{-0.22}$	0.849*
NGC6338	$2.13^{+0.10}_{-0.05}$	$3.63^{+0.56}_{-0.56}$	0.400*
NGC6482	$0.64^{+0.01}_{-0.01}$	$0.111^{+0.012}_{-0.012}$	1.04
RXCJ1022	$2.05^{+0.10}_{-0.12}$	$2.62^{+0.74}_{-0.74}$	0.653*
RXCJ2214	$1.43^{+0.06}_{-0.10}$	$0.602^{+0.109}_{-0.109}$	0.605
S0463	$1.78^{+0.29}_{-0.22}$	$1.98^{+0.33}_{-0.33}$	0.084
SS2B	$0.91^{+0.01}_{-0.01}$	$0.666^{+0.045}_{-0.045}$	1.66*

Table 5.2: Observed bolometric $L_{\rm X}$–T relation.

Category	slope, (m)	normalisation, (log c)	$\sigma_{\rm int,\ L_X}$	$\sigma_{\rm stat,\ L_X}$	$\sigma_{\rm int,\ T_{vir}}$	$\sigma_{\rm stat,\ T_{vir}}$
All Groups	2.17 ± 0.26	−0.01 ± 0.09	0.237	0.056	0.109	0.015
All HIFLUGCS clusters	2.97 ± 0.20	0.42 ± 0.04	0.264	0.010	0.089	0.013
SCC Groups	2.56 ± 0.22	0.17 ± 0.10	0.230	0.054	0.090	0.0099
SCC Clusters	3.46 ± 0.20	0.51 ± 0.05	0.234	0.0092	0.068	0.0093
NSCC Groups	2.00 ± 0.39	−0.09 ± 0.11	0.226	0.059	0.113	0.019
NSCC Clusters	2.76 ± 0.29	0.40 ± 0.05	0.240	0.011	0.087	0.015
CRS Groups	2.14 ± 0.31	−0.03 ± 0.11	0.253	0.049	0.118	0.015
CRS Clusters	3.31 ± 0.20	0.45 ± 0.04	0.237	0.011	0.072	0.012
NCRS Groups	2.29 ± 0.31	0.04 ± 0.09	0.169	0.081	0.074	0.013
NCRS Clusters	2.40 ± 0.37	0.41 ± 0.11	0.227	0.0082	0.095	0.014

5.2.3 Bias correction

Observed scaling relations can be affected by various selection biases, chief among which is the Malmquist bias. The Malmquist bias is the preferential detection of brighter objects for e.g. a given temperature, in a flux-limited sample due to intrinsic scatter. It is an effect that has been shown to affect scaling relations, namely resulting in higher observed normalisations as compared to the actual normalisations in scaling relations for clusters (e.g. Ikebe et al. 2002, Stanek et al. 2006, Pratt et al. 2009, Mantz et al. 2010, Lovisari et al. 2015). In this sample, we have applied an additional luminosity cut which could further contribute to the bias. Thus, in order to determine the "true" relation, one has to correct for these biases. To do this, we undertook simulations, the procedure of which we describe below.

For the simulations, we randomly generated samples of groups with temperatures between 0.6 and 3.6 keV. These groups were assigned luminosity distances such that the number of objects scaled as $D_{\rm L}^3$, between redshifts of 0.01 and 0.2, and temperatures corresponding to the X-ray temperature function (the XTF, Markevitch 1998, given by $\mathrm{d}N/\mathrm{d}V \sim T^{-3.2}$). Using different combinations of slopes, normalisations, and scatters, we assigned luminosities to these temperatures. The intrinsic scatter about $L_{\rm X}$ is log-normal and was introduced as such. Measurement errors were included for both $L_{\rm X}$ and T, which corresponded to the observed statistical scatter. For each set of parameters, we generated 100 samples and applied a flux cut of 2.5×10^{-12} erg s^{-1} cm^{-2} and an upper luminosity cut of $2.55 \times 10^{43} h_{70}^{-2}$ erg s^{-1} (both in the ROSAT band) to simulate the selection criteria, with each sample containing between 20-30 objects, similar to the actual group sample used in the study. To determine the best set of parameters, we defined a chi-squared:

$$\chi^2 \equiv \left(\frac{m_{\rm obs} - m_{\rm out}}{\Delta m_{\rm obs}}\right)^2 + \left(\frac{c_{\rm obs} - c_{\rm out}}{\Delta c_{\rm obs}}\right)^2 + \left(\frac{\sigma_{\rm obs} - \sigma_{\rm out}}{\Delta \sigma_{\rm obs}}\right)^2 . \tag{5.8}$$

Here m is slope, c is normalisation, σ is the intrinsic scatter in luminosity. Obs are the observed parameters, out is the output given by the simulation. The deltas represent the measured errors, from the BCES fit. For the scatter, we assumed that $\frac{\Delta\sigma_{\rm obs}}{\sigma_{\rm obs}} = 10\%$. Changing this value from 5 to 20% does not alter the results significantly. An example of this simulation is shown in Fig. 5.2.

Scaling relations for different cases, e.g. SCC and NSCC groups, may differ, therefore selection effects may differ for the different cases as well, making it imperative to determine bias corrections for the individual sub-cases. To do this, fresh simulations were run with the fractions of SCC/NSCC objects, and CRS/NCRS objects fixed to the observed values noted in Bharadwaj et al. (2014). We note that small changes in the SCC/NSCC fractions and the CRS/NCRS fractions do not drastically affect the determination of the bias-corrected slopes, normalisations, and scatters for the group sample.

Note that, despite our concerted efforts to correct for the selection biases, due to the incomplete nature of this sample compiled from the Chandra archives, we do not rule out the possibility of a potential 'archival bias', which could have a bearing on the results and which we cannot correct for.

5.2.4 Cluster comparison sample

To compare our results for groups to galaxy clusters, we decided to use the HIFLUGCS galaxy clusters (Reiprich & Böhringer 2002), a flux-limited sample with ROSAT (0.1–2.4 keV) flux $\geq 2{\times}10^{-11}$ erg s^{-1} cm^{-2}. For this study, we took the bolometric X-ray luminosities and virial temperatures quoted in Mittal et al. (2011). Since the temperatures were determined with CALDB version 3 (3.2.1) versus version 4 for the galaxy groups, we converted the quoted temperatures using the scaling relation quoted in Mittal et al. (2011), namely:

$$T_{4.1.1} = (0.875 \times T_{3.2.1}) + 0.251. \tag{5.9}$$

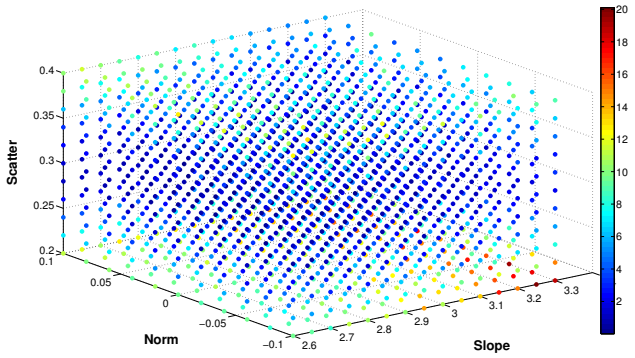

Figure 5.2: Slopes, normalisations, and intrinsic scatter for the "all groups" case. The plot is colour-coded to represent the value of chi-squared.

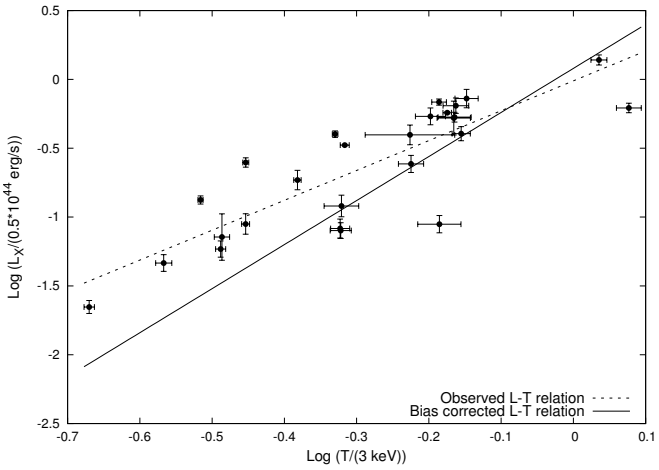

Figure 5.3: Observed and bias-corrected L_X–T relation for galaxy groups. The dotted line is the observed scaling relation and the solid line is the bias-corrected scaling relation.

Using this scaling relation has the effect of lowering the temperature, thereby raising the normalisation and steepening the observed cluster L_X–T relation. The change in slope and normalisation, however, are within the errors of that obtained with the older temperatures. Since the groups and the cluster samples have different selection criteria, bias corrections were performed for clusters as well, using the above flux limit to compare results accurately. For the sub-samples, we took the SCC/NSCC fraction and the CRS/NCRS fraction for the clusters from Hudson et al. (2010) and Mittal et al. (2009), respectively.

5.3 Results and discussion

5.3.1 Observed, bias-uncorrected L_X–T relation

The fit results for the observed data sets (both groups and clusters) are shown in Table 5.2. For all groups, the best-fit results are shown in Fig. 5.3.

The very first observation that one makes on comparing the observed L_X–T relation of groups to clusters is the flattening of the slope when one enters the group regime. Additionally, we observe that

Table 5.3: Bias corrected, bolometric L_X–T relation for groups, and clusters. Errors are the measurement errors from observations.

Sample	Category	Slope, (m)	Normalisation, (log c)	$\sigma_{\mathrm{int},\,L_X}$
Groups	ALL	3.20 ± 0.26	0.08 ± 0.09	0.32
HIFLUGCS	ALL	2.79 ± 0.20	0.21 ± 0.04	0.27
Groups	SCC	3.60 ± 0.22	0.30 ± 0.10	0.30
HIFLUGCS	SCC	3.45 ± 0.20	0.34 ± 0.05	0.26
Groups	NSCC	2.52 ± 0.39	−0.17 ± 0.11	0.30
HIFLUGCS	NSCC	2.68 ± 0.29	0.22 ± 0.05	0.26
Groups	CRS	3.60 ± 0.31	0.16 ± 0.11	0.36
HIFLUGCS	CRS	3.20 ± 0.20	0.26 ± 0.04	0.26
Groups	NCRS	3.20 ± 0.31	0.09 ± 0.09	0.30
HIFLUGCS	NCRS	2.40 ± 0.37	0.10 ± 0.11	0.30

for most cases, the slope of the observed L_X–T relation is consistent with the self-similar value of 2 expected for clusters within the errors. As we demonstrate in Sect. 5.3.2, this is due to the selection criteria applied to construct this sample, and is not a property of the underlying group population. Additionally, the observed L_X–T relation for the SCC groups shows indications of being higher in normalisation (by a factor of $\sim$ 2) and having a steeper slope as compared to the NSCC groups. For groups with a CRS, there is an indication that the normalisation is lower than for those groups without a CRS.

The statistical scatters in the temperature for both groups and clusters are in good agreement, but for the luminosity, we see an increase by around a factor of 5 as we go from the cluster to the group regime. This is expected, as groups, being low surface brightness systems, have a much larger error in their luminosity than is the case for clusters. Additionally, the luminosities for the galaxy groups come from the RASS data with very short exposure times, versus that of the clusters, which come from ROSAT position sensitive proportional counter (PSPC) pointed observations with much larger exposure times, leading to a much more precise determination of the cluster luminosities.

5.3.2 Bias-corrected L_X–T relation

We tabulate the bias corrected L_X–T relation for both groups and clusters in Table 5.3. As pointed out before, this is the first attempt to present a bias-corrected bolometric L_X–T relation for groups including their cool-core and central AGN properties, making comparisons between groups and clusters a lot easier than before.

Our very first observation is that correcting for selection effects has a significant impact on the L_X–T relation for the galaxy groups. Over most of the temperature range covered by the group sample, the bias corrected relation results in a lower L_X for a given T, and the bias-corrected slope steepens significantly from 2.17 to 3.20 (Fig. 5.3). With the corrections in place, the value of our slope agrees well with previous bolometric L_X–T slopes for galaxy groups observed for incomplete samples (e.g. Osmond & Ponman 2004), but is much lower than reported slopes of $\sim$ 5 (Helsdon & Ponman 2000; Xue & Wu 2000 at $> 5\sigma$ significance). The value of the corrected slope for groups shows indications of a steepening compared to clusters, but the two slopes are consistent within the errors (Fig. 5.4, Table 5.3). Qualitatively our results show the same trend as reported recently by Lovisari et al. (2015).

Sub-classifying the sample yields more interesting features. The L_X–T relation for the SCC and CRS groups is by far the steepest with the SCC groups having the highest normalisation for all the sub-samples at 3 keV. The slope of the bias-corrected L_X–T relation for the SCC groups is steeper than the NSCC slope by 43% and higher in normalisation by a factor of $\sim$ 3 at 3 keV (Fig. 5.5). The

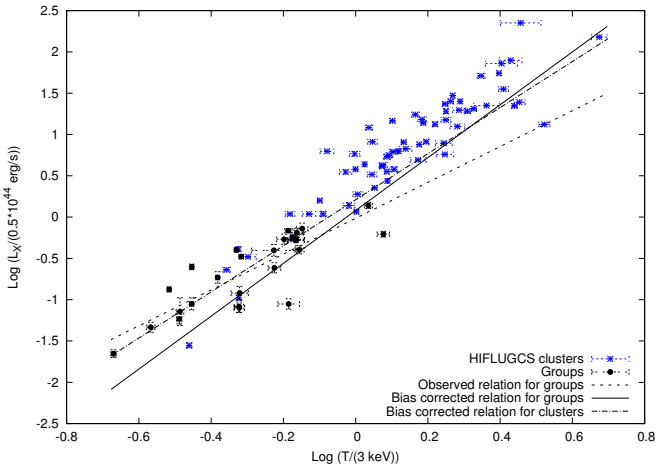

Figure 5.4: Observed and bias-corrected L_X–T relations. Clusters are represented by blue points and groups are represented by black points. Dotted line is observed relation for groups, solid line is bias-corrected relation for groups, dot-dash line is bias-corrected relation for clusters.

normalisations for the CRS groups and NCRS groups are in good agreement (within 17%, ignoring the errors), but there are indications of marginal steepening of the slopes for the CRS systems, albeit the large error bars make it hard to confirm. The bias-corrected slopes of most of the sub-samples for the groups and clusters are once again consistent within the errors. These numbers suggest a rather complicated scenario for the group regime and we discuss this in Sect. 5.3.3.

Our attempt to identify the bias-corrected scatter vs. the observed scatter for L_X to our best knowledge is a first for the L_X–T scaling relation. Interestingly, while the observed and the bias-corrected scatter for the complete cluster sample agree within 10%, the bias-corrected scatter for groups is higher by 35% as compared to the observed scatter. This statement also holds true qualitatively for most of the sub-samples that we fit here. The reason behind this could simply be due to the applied upper luminosity cut to select the group sample. The corrected intrinsic scatter increases by 19% as one moves down from the cluster to the group regime, with the largest change in intrinsic scatter between groups and clusters observed for the CRS case ($\sim$ 38%). We have demonstrated for the first time, that the bias-corrected intrinsic scatter in L_X seems to increase from the cluster to the group regime. This would indicate a stronger impact of non-gravitational processes on the group regime than the cluster regime, as one would expect. Interestingly, this conclusion of ours is somewhat different to the results of Lovisari et al. (2015), who conclude that the scatter decreases as one goes from the cluster to the group regime. We point out that their conclusion is based on the *observed* scatter as they do not explicitly try to obtain a bias-corrected scatter as we have done in this study. Nevertheless, the small sample sizes in both studies, the choice of X-ray luminosities (ROSAT band vs. bolometric band), the potential archival bias in our study, and different techniques in performing the bias correction could all have a potential impact on the determination of the "true" scatter.

Our simulations clearly demonstrate that selection criteria employing a flux and luminosity cut have a stronger impact on the L_X–T relation, particularly on the slope, than those with just a simple flux cut, as in e.g. the HIFLUGCS cluster sample. Additionally, we have also demonstrated that the bias corrections for sub-samples, especially SCC and NSCC sub-samples are not identical and have to be determined individually.

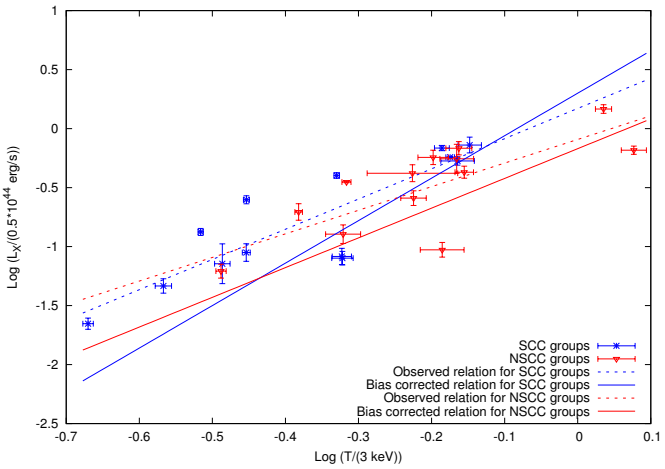

Figure 5.5: Observed and bias-corrected L_X–T relation for SCC and NSCC groups. Blue dotted line represents observed relation for SCC groups, blue solid line represents bias-corrected relation for SCC groups, red dotted line represents observed relation for NSCC groups, red solid line represents bias-corrected relation for NSCC groups.

5.3.3 A complete picture of the L_X–T relation

When one wishes to interpret observational results for scaling relations, a good starting point is to look at existing results from simulations. In recent times, the introduction of sophisticated code, which accounts for non-gravitational processes such as cooling and feedback, have made simulations much more accurate than before. It is all but clear that only simulation recipes with some form of AGN feedback can mitigate excessive gas cooling and high star formation rates that are inconsistent with observations (e.g. Borgani et al. 2004). Recent results by e.g. Puchwein et al. (2008) and McCarthy et al. (2010) argue that an L_X–T relation consistent with observations is obtained for groups only with AGN feedback. This simplified picture would seem to solve all problems, but observations seem to point to a more complex scenario.

Interpreting the high normalisations of the SCC groups is relatively straightforward; these are systems with the most centrally dense cores, and since the emissivity scales as the density squared, there is a boost given to their X-ray luminosities leading to a higher normalisation in the L_X–T relation compared to other sub-samples. The steepening could be explained as a higher increase in X-ray luminosity for relatively high temperature SCC groups ($\geq$ 1 keV), which probably continues to decrease as we go down the temperature scale. The relatively low X-ray luminosity for the NSCC groups, which are WCC and NCC groups, is an indication that there is not strong cooling going on in these systems. It could also indicate the further influence of AGN feedback (particularly for the NCC groups), which suppresses the X-ray luminosity, though we do wish to point out that not all WCC groups harbour a CRS.

This brings us to our next point of discussion, namely the L_X–T relation for those groups with and without a CRS. As the slopes and normalisations for the CRS and the NCRS are both consistent within the errors for the CRS and the NCRS cases, we tried to see if divisions based on the morphology of the CRS could unravel some features. Dividing the groups between those with an CRS that show extended radio emission and those with CRSs that show only central emission based on a visual inspection of the radio contours (Appendix D), we observe that the former has a much steeper slope than the latter (3.64 $\pm$ 1.21 vs. 2.07 $\pm$ 0.31). Taking this one step further, we fit the L_X–T relation for two more sub-samples; this time dividing the sample on the basis of the median radio luminosity of the CRSs

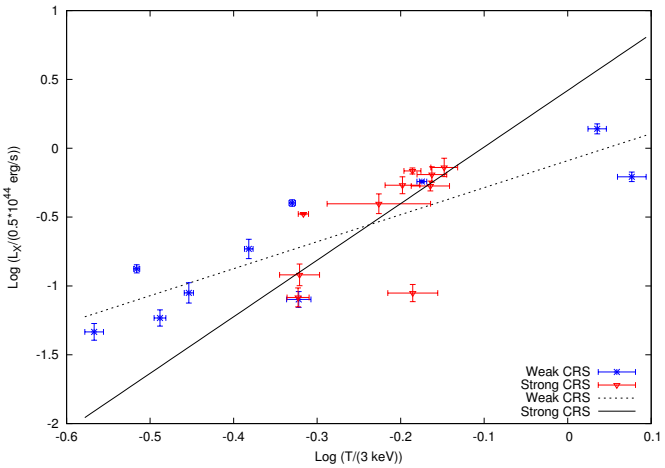

Figure 5.6: The L_X–T relation for sub-samples divided on the basis of the median radio luminosity of the CRS. Blue points ('weak' CRS) represent those groups that have a CRS with total radio luminosity less than the median radio luminosity, while red points represent those groups with a CRS greater than or equal to the median radio luminosity.

(Fig. 5.6). Once again, we observe that the groups with a "strong" radio source (greater than or equal to the median radio luminosity) have a much steeper scaling relation (4.11 ± 1.38 vs. 1.96 ± 0.31) than those with "weak" radio sources. Qualitatively, both these results are in agreement with Magliocchetti & Brüggen (2007) who find a much steeper slope for objects with extended radio sources (~ 4) than for radio sources with point-like emission. The mean radio output of the SCC groups CRS is a factor of 34 lower than the NSCC groups CRS, which could indicate that AGN activity is weaker in SCC groups than the NSCC groups, assuming the radio luminosity is a good indicator of AGN activity. This would be very much in line with simulation results by Gaspari et al. (2011, 2014) who argue that AGN feedback in galaxy groups must be self-regulated with low mechanical efficiencies, and is a fundamental requirement for the preservation of the cool core. Moreover, in this particular group sample, 60% of the groups with a "strong" CRS are NSCC groups, while 60% of the groups with a "weak" CRS are SCC groups. This could be an indication that the more powerful radio AGN are preferentially located in NSCC groups rather than SCC groups. These conclusions are subject to selection effects, and more robust results would require a much larger, complete group sample, backed by radio data down to lower frequencies and more homogeneous flux limits.

5.4 Summary

With a sample of 26 galaxy groups, we studied the effects of ICM cooling, AGN feedback, and selection effects on the L_X–T relation for the galaxy group regime. The main results of this study can be summarised as follows:

- The observed L_X–T relation for groups is significantly affected by selection effects that impact the slope, normalisation, and the intrinsic scatter in L_X and requires bias corrections. We also conclude that SCC groups require a different bias correction than NSCC groups.
- The bias-corrected slope of the L_X–T relation for groups obtained after correcting for selection effects shows indications of steepening, but is consistent within errors to the bias-corrected slope of the clusters.

- The SCC groups have the highest normalisation and the steepest slope for the scaling relation. This is attributed to the enhanced luminosities of these systems.
- The bias-corrected intrinsic scatter in L_X seems to generally increase as we enter the group regime. Additionally, for groups the observed intrinsic scatter is lower than the bias-corrected scatter obtained from simulations for most cases.
- Subject to selection effects, we see indications of a steepening of the scaling relation for those groups that have a CRS radio luminosity greater than the median, and speculate that such relatively powerful CRSs are preferentially located in NSCC groups.

In short, we have demonstrated that the behaviour of the L_X–T relation in groups is similar (e.g. the slopes) and yet different (e.g. intrinsic scatter in L_X) to that in clusters. The next step towards having a survey ready L_X-T relation would be to account for every process at work in galaxy groups, their effect on the slopes and normalisations, and their contribution to the overall scatter. Quantifying these processes will be a challenge. As we have pointed out, objectively selected, large samples of groups, particularly to much lower temperatures (< 1 keV) with good quality X-ray data and without potential archival bias, would be of paramount importance. Additionally, we expect more features to be obtained when we sub-classify these potential group samples into SCC, WCC, and NCC classes and sub-classes thereof. This is a project that we hope to pursue in the near future.

CHAPTER 6

Investigating the cores of fossil systems with Chandra

This chapter is presented as a research paper that was submitted to the journal Astronomy and Astrophyiscs and has been recommended for publication by an anonymous referee, subject to revisions. The core properties of 17 fossil systems with archival Chandra data are discussed here. Section 6.1 gives an introduction to fossil groups/clusters of galaxies and motivates the study that was conducted in this work. Section 6.2 discusses the sample of fossil systems, the basic data reduction steps, and the analysis involved in obtaining the cool-core properties of the fossils. Section 6.3 presents the results and a discussion is presented. A short summary is presented in Sec. 6.4. The text is reproduced largely unmodified from the submitted article with only very minor changes for typographical and grammatical reasons.

6.1 Introduction

Clusters of galaxies are the largest gravitationally bound structures in the Universe, with an aggregate mass between a few times 10^{13} $M_\odot$ and 10^{15} $M_\odot$. Consisting of galaxies, hot X-ray emitting gas (the intracluster medium—ICM) and dominated by dark matter, these objects are unique in their application to study both cosmology and astrophysics. On the lower mass end, these systems are sometimes called as groups, to indicate a smaller aggregation of galaxies. The distinction between groups and clusters is quite loose, with definitions in literature based on optical richness or simply a mass/temperature cut (e.g. Stott et al. 2012).

Within the existing division of groups and clusters, lie an ostensibly "special" class of systems called as fossil systems (also called as fossil groups); systems which are dominated by a single, bright, elliptical galaxy and deficient in other bright galaxies. The first fossil group was reported by Ponman et al. (1994) who showed the existence of a system at redshift 0.171 which had a large X-ray halo associated with an elliptical galaxy. The choice of nomenclature "fossil" is used to indicate a class of systems which is a remnant of galaxy merging, with hot X-ray gas and an elliptical galaxy the only remnants of this process. A "formal" definition for a fossil system was provided by Jones et al. (2003) who defined it as a spatially extended X-ray source with luminosity larger than $10^{42} h_{50}^{-2}$ erg/s with an optical counterpart wherein the magnitude difference between the first and second brightest galaxy is greater than or equal to 2 in the Johnson R band. Simulations by Dariush et al. (2007) show that systems selected by this

criterion represent a class of objects which assemble a higher fraction of their mass at high redshift as compared to non-fossils, further justifying their tag of being early-forming "old" systems. This formal definition, however, is open to contention as pointed out again by Dariush et al. (2010) who argue via simulations that a magnitude difference of 2.5 between the first and fourth brightest galaxy identifies 50% more early formed systems.

The most widely acknowledged formation scenario for these systems is one wherein dynamical friction causes galaxies close to the centre of the group to merge and leave behind a large elliptical galaxy and a hot X-ray halo (e.g. D'Onghia et al. 2005). An outstanding question is if the properties of fossil systems make them a *special* class of systems. Also, it is still unclear whether they are the final stages of mass assembly or are merely a temporary state in the formation of larger clusters. La Barbera et al. (2009) argue that fossils are not special, and merely represent the final stages of mass assembly in a region without enough surrounding matter. Simulations by von Benda-Beckmann et al. (2008) claim however, that the "fossil" phase is a temporary one and the magnitude gap would end by renewed infall from the surroundings. Adding to the confusion are results by Proctor et al. (2011) who argue that the high mass to light ratios of these systems and their low richness are not predicted by any current model of fossil formation.

Very few fossil systems have been thoroughly studied, which adds to the lack of sound conclusions on their formation and evolution (e.g. Mulchaey & Zabludoff 1999; Khosroshahi et al. 2004; Sun et al. 2004). X-ray sample studies of fossil systems, which could provide us additional details, are even rarer (e.g. Khosroshahi et al. 2007; Miller et al. 2012; Harrison et al. 2012) and have focused more on global properties such as X-ray luminosity, temperature and mass. Till date, there has never been a detailed and focused investigation of the cores of a sample of fossil systems in X-rays, particularly with respect to their cool-core properties.

The cores of galaxy clusters and groups offer important hints on the dynamical state of the ICM in the central regions, e.g. systems which are morphologically disturbed, generally have long central cooling times (CCTs) and elevated central entropies as compared to relaxed systems which show much shorter CCTs and lower central entropies. The clusters with the strongest cooling, namely the strong cool core (SCC) clusters, show very short CCTs (≤ 1 Gyr), low entropies (≤ 30 keV cm^2), and central temperature drops (Hudson et al. 2010). This is not necessarily true on the group regime, where there are examples of systems which do not show any indication of cool gas in the cores despite short CCTs and low entropies (e.g. Bharadwaj et al. 2014). Feedback also plays an important role in cluster/group cores as without it, there would be catastrophic cooling with very high mass deposition rates, inconsistent with observations (e.g. Peterson et al. 2001; Tamura et al. 2001; Kaastra et al. 2001; Peterson et al. 2003; Sanders et al. 2008). Where do fossil systems fit in this picture? What hints can the cool core properties of these systems offer in terms of their formation and evolution? These are the questions we attempt to address in this paper.

This paper is organised as follows: Section 6.2 deals with the data and analysis. We present our results and discuss them in section 6.3. A short summary is presented in section 6.4. Throughout this work, we assume a ΛCDM cosmology with $\Omega_m = 0.30$, $\Omega_\Lambda = 0.70$ and $h = 0.70$ where $H_0 = 100h$ km/s/Mpc, unless stated otherwise. All errors are quoted at the 68% level. Log is always base 10 here.

6.2 Data and analysis

6.2.1 Sample

For this study, we selected a sample of 17 fossil systems and candidates spanning a large redshift range (from ~ 0.01 to ~ 0.4) with good quality archival Chandra data ($t_{exp} \geq 10$ ks) as required for exploring

Table 6.1: The sample of fossil systems. The starred entry represents the system which was only considered in the L_X–T study. Columns are (1) name of the fossil system, (2) redshift (3) literature sources.

Name	redshift	Literature
NGC 6482	0.013129	Khosroshahi et al. (2004)
NGC 1132	0.0232	Mulchaey & Zabludoff (1999)/Yoshioka et al. (2004)
RX J0454.8-1806	0.0314	Yoshioka et al. (2004)
ESO 306–G 017	0.035805	Sun et al. (2004)
UGC 842	0.045	Lopes de Oliveira et al. (2010)
RX J1331.5+1108	0.081	Jones et al. (2003)
cl1159p5531	0.081	Vikhlinin et al. (1999)/Voevodkin et al. (2010)
cl2220m5228	0.102	Voevodkin et al. (2010)
cl1038p4146*	0.125	Voevodkin et al. (2010)
cl1416p2315	0.138	Jones et al. (2003)/Voevodkin et al. (2010)
cl0245p0936	0.147	Voevodkin et al. (2010)
cl1340p4017	0.171	Ponman et al. (1994)/Voevodkin et al. (2010)
RX J2247.4+0337	0.199	Vikhlinin et al. (1999)/Voevodkin et al. (2010)
RX J0825.9+0415	0.225	Eigenthaler & Zeilinger (2009)
RX J1256.0+2556	0.232	Jones et al. (2003)
RX J0801+3603	0.287	Eigenthaler & Zeilinger (2009)
RX J1115.9+0130	0.352	Eigenthaler & Zeilinger (2009)
RX J10159.8-0850	0.405	Eigenthaler & Zeilinger (2009)

the properties under consideration here. Chandra was preferred over XMM-Newton due to its superior spatial resolution which makes it easier to probe the central regions which is the major focus of the work. Though the systems were categorized as fossil systems through different techniques, qualitatively the basic selection criteria of a lower X-ray luminosity threshold and a magnitude difference between the first and second brightest galaxies, is maintained for all of them. We also endeavoured to study the L_X–T relation for those fossil systems selected from the 400d cluster sample (Sec. 6.3.6) for which we analysed XMM-Newton data for one more fossil group which was not included for the other studies. Table 6.1 summarises the basic information of the sample with redshifts and literature sources.

6.2.2 Basic data reduction

Most of the data reduction steps were similar to that followed in Bharadwaj et al. (2015) and Bharadwaj et al. (2014) and we describe them here briefly. CIAO 4.4[1] with CALDB 4.5.0 was used for the data reduction. The `chandra_repro` task reprocessed the data and removed afterglows, created the bad-pixel table and applied the calibration. The `lc_clean` algorithm was used to filter the soft proton flares, with the lightcurves visually inspected to check for any residual flaring. Point sources were detected and excluded from further analysis with the `wavdetect` wavelet algorithm. Since our focus is on the bright, central regions, background subtraction for the spectral and surface brightness analysis was done throughout using the blank sky background files. The X-ray emission peak (EP) was determined in an exposure corrected, point source subtracted image using the CIAO tools built into ds9 with a pixel scale of 2.

For extracting spectra, we created annular regions with a minimum source counts threshold of 1000.

[1] http://cxc.harvard.edu/ciao

This ensured that the annuli are sufficiently small and at the same time does not sacrifice too much on the signal to noise. The resultant spectra were fit with an absorbed APEC model in the 0.7–7.0 keV energy range, with the $n_{\rm H}$ value taken from the built in $n_{\rm H}$ ftools which outputs the value from the Leiden/Argentine/Bonn (LAB) survey (Kalberla et al. 2005). The abundance was kept thawed for the spectral fit and in cases where we could not get a reasonable constraint on the value, we froze it to 0.30. We used the Anders & Grevesse (1989) abundance table throughout.

The surface brightness profile (SBP) was obtained by centring on the EP. This SBP was then fit by a single or double beta model (e.g. Cavaliere & Fusco-Femiano 1976) given by

$$\Sigma = \Sigma_0 \left[1 + \left(\frac{x}{x_{\rm c}}\right)^2\right]^{-3\beta+1/2}, \tag{6.1}$$

$$\Sigma = \Sigma_{01} \left[1 + \left(\frac{x}{x_{\rm c_1}}\right)^2\right]^{-3\beta_1+1/2} + \Sigma_{02} \left[1 + \left(\frac{x}{x_{\rm c_2}}\right)^2\right]^{-3\beta_2+1/2}, \tag{6.2}$$

where $x_{\rm c_i}$ is the core radius. This in turn gave us the electron density profile for the single and double beta cases as

$$n = n_0 \left[1 + \left(\frac{r}{r_{\rm c}}\right)^2\right]^{\frac{-3\beta}{2}}, \tag{6.3}$$

$$n = \left(n_{01}^2 \left[1 + \left(\frac{r}{r_{\rm c_1}}\right)^2\right]^{-3\beta_1} + n_{02}^2 \left[1 + \left(\frac{r}{r_{\rm c_2}}\right)^2\right]^{-3\beta_2}\right)^{1/2}, \tag{6.4}$$

where $r_{\rm c}$ is the physical core radius. The central electron density n_0 for the single beta case is given by

$$n_0 = \left(\frac{10^{14} 4\pi D_{\rm A} D_{\rm L} \zeta N}{\rm EI}\right)^{\frac{1}{2}}. \tag{6.5}$$

Here, N is the normalisation of the APEC model in the innermost annulus, ζ is the ratio of electrons to protons (~ 1.2), $D_{\rm A}$ is the angular diameter distance and $D_{\rm L}$ is the luminosity distance. EI is defined as:

$${\rm EI} = 2\pi \int_{-\infty}^{\infty} \int_{0}^{R} x \left(1 + \frac{x^2 + l^2}{x_c^2}\right)^{-3\beta} {\rm d}x{\rm d}l, \tag{6.6}$$

where R is the radius of the innermost annulus.

Similarly, for the double beta case, n_0 (Appendix A of Hudson et al. 2010) is given by

$$n_0 = \left[\frac{10^{14} 4\pi(\Sigma_{12}{\rm LI}_2 + {\rm LI}_1) D_{\rm A} D_{\rm L} \zeta N}{\Sigma_{12}{\rm LI}_2{\rm EI}_1 + {\rm LI}_1{\rm EI}_2}\right]^{\frac{1}{2}}, \tag{6.7}$$

with the same definitions as before. ${\rm LI}_i$ is the line emission measure and is defined as

$${\rm LI}_i = \int_{-\infty}^{\infty} \left(1 + \frac{l^2}{x_{c_i}^2}\right)^{-3\beta_i} {\rm d}l \tag{6.8}$$

To estimate the uncertainty on n_0, we conducted Monte Carlo simulations where the surface brightnesses were varied within their errors to generate new SBPs. These new SBPs were then fit again by

a single or double beta model which was then used to determine n_0 (the APEC normalisation is also varied each time within the errors). The process was repeated 500 times to get a distribution for the values of n_0, and the standard deviation of the distribution gives the uncertainty on the measured n_0.

6.2.3 Cool-core analysis

The most robust parameter to identify the cool-core nature of an object is the CCT (Hudson et al. 2010), a quantity that is dependent on the central temperature and the central density. But, considering that most (59%) of our objects have a redshift ≥ 0.1, the determination of the CCT becomes problematic given that it is difficult to resolve the temperature profile for these objects in the central regions. Moreover, in many cases the data quality is not good enough to determine a temperature profile. Thus, in addition to the CCT, we used two other diagnostics, namely, cuspiness α and concentration parameter $c_{\rm SB}$, both of which have been shown to have a strong correlation with the cooling time (e.g. Santos et al. 2010; Hudson et al. 2010). Indeed, recent studies of high redshift systems have used these two quantities to identify their CC nature (e.g. Semler et al. 2012; Pascut & Ponman 2014). In our study, if a fossil satisfied two out of three CC diagnostics, it was classified as a CC system.

The CCT is given as

$$\mathrm{CCT} = t_{\rm cool}(0) = \frac{3}{2}\zeta\frac{(n_{\rm e0} + n_{\rm i0})kT_0}{n_{\rm e0}^2\Lambda(T_0, Z_0)}, \tag{6.9}$$

where n_{i0} and n_{e0} are the central ion and electron densities, respectively, and T_0 is the temperature in the innermost annulus. As with Hudson et al. (2010) and Bharadwaj et al. (2014) we took the value of central density values to be the value at $r = 0.004r_{500}$. To estimate r_{500}, we determined the virial temperature ($T_{\rm vir}$) in a single region centered on the EP, and a scaling relation by Evrard et al. (1996)

$$\left(\frac{r_{500}}{h_{71}^{-1}\ \mathrm{Mpc}}\right) = 2 \times \left(\frac{T_{\rm vir}}{10\ \mathrm{keV}}\right)^{\frac{1}{2}}. \tag{6.10}$$

To determine $T_{\rm vir}$ for cl1416p2315 (and later also cl1038p4146) we used the XMM-Newton data sets which were analysed with the standard pipelines as illustrated in Schellenberger et al. (2014). Note that temperatures determined from Chandra and XMM-Newton can differ significantly as shown by Schellenberger et al. (2014) and hence to remain consistent, we used the formula given in that study to convert the XMM-Newton temperatures to Chandra temperatures,

$$\log_{10}(T_{\rm XMM}) = 0.889 \times \log_{10}(T_{\rm Chandra}). \tag{6.11}$$

There are six fossil systems for which we could not obtain a temperature profile. Hence, for these objects we assumed $T_{\rm vir}$ to be the central temperature while constraining the CCT. To estimate the uncertainties on the CCT for these objects, we conservatively assumed the lower bound of the temperature to be 0.6 times of $T_{\rm vir}$ (the largest central temperature decrement observed for $z < 0.05$ fossils, i.e. ES0306) and the upper bound to be 1.25 times $T_{\rm vir}$ (the largest central temperature increment, i.e. NGC 6482). A CC system has a CCT < 7.7 Gyr.

The cuspiness α (Vikhlinin et al. 2007) is defined as

$$\alpha = -\frac{\mathrm{d}\log(n)}{\mathrm{d}\log(r)} \tag{6.12}$$

which in model parameters (Hudson et al. 2010) for the single beta model is expressed as

$$\alpha = \frac{3\beta r^2}{r_c^2 + r^2} \tag{6.13}$$

and for the double beta model is

$$\alpha = 3r^2 \frac{\Sigma_{12}\mathrm{LI}_2\beta_1 r_{c_1}^{-2} b_1' + \mathrm{LI}_1\beta_2 r_{c_2}^{-2} b_2'}{\Sigma_{12}\mathrm{LI}_2 b_1 + \mathrm{LI}_1 b_2}. \tag{6.14}$$

Here, $\Sigma_{12}, \mathrm{LI}_1$ and LI_2 are as defined for the CCT, b_i and b_i' are defined as

$$b_i \equiv \left(1 + \left(\frac{r}{r_{c_i}}\right)^2\right)^{-3\beta_i}, \tag{6.15}$$

and

$$b_i' \equiv \left(1 + \left(\frac{r}{r_{c_i}}\right)^2\right)^{-3\beta_i - 1}, \tag{6.16}$$

respectively. In both single and double beta cases, cuspiness is calculated at $r = 0.04 r_{500}$. A CC system has $\alpha \geq 0.5$. The error on α is once again determined by Monte Carlo simulations as with n_0.

The concentration parameter c_{SB} (Santos et al. 2008) is given as

$$c_{\mathrm{SB}} \equiv \frac{\Sigma(r < 40\ \mathrm{kpc})}{\Sigma(r < 400\ \mathrm{kpc})}, \tag{6.17}$$

where Σ is the integrated surface brightness within the defined radii (40 and 400 kpc). A CC system has $c_{\mathrm{SB}} \geq 0.075$. As the $z < 0.05$ fossils are too close for estimating the surface brightness within 400 kpc, we did not determine c_{SB} for these systems.

6.3 Results and discussion

6.3.1 Cool-core properties

Table 6.2 summarises the CC properties of the fossil systems. We find that 14 out of 17 systems, i.e., 82% are cool core systems, as evidenced by at least two out of the three CC diagnostics. If one uses the CCTs, we observe a range of values from a minimum of 0.124 Gyr to a maximum of 24.2 Gyr. The sub-classifications of the fossil systems using just the CCTs are 29% SCC (CCT $<$ 1 Gyr), 53% WCC (1 $\leq$ CCT $<$ 7.7 Gyr), and 18% NCC (CCT $\geq$ 7.7 Gyr).

As we have already pointed out, it is not always possible to determine the CCT and this becomes especially true for X-ray survey data (e.g. eROSITA). Thus, we also state the effect of using one CC parameter alone. With only the cuspiness, we identify 76% of the fossil systems as CC systems. If one uses the concentration parameter alone, we observe that 67% of the systems are selected as CC systems (though it's quite likely that the $z < 0.05$ fossils will also have $c_{\mathrm{SB}} > 0.075$, in which case the fraction would go up to 76%).

Thus, if one were to simply use a single quantity to identify CC groups, conservatively, one would get a lower limit on the fossil CC fraction of 67% and an upper limit of 82%, i.e. qualitatively there are indications that a majority of fossil systems are CC systems, albeit as the cooling times indicate, most of them are WCC systems. Fig. 6.1 shows the relation between the CCT–α and CCT–c_{SB} and despite

Table 6.2: Cool-core diagnostics of the fossils. The columns are (1) name of system, (2) co-ordinates (J2000) of the EP, (3) virial temperature of fossil, (4) central cooling time, (5) cuspiness, (6) concentration parameter, (7) cool-core or not, via any two diagnostics. Starred entries represent fossils for which the CCT was determined using $T_{\rm vir}$.

Name	EP (RA/DEC)	$T_{\rm vir}$ (keV)	CCT (in Gyr)	α	$c_{\rm SB}$	CC or not?
NGC 6482	17 : 51 : 48.85 + 23 : 04 : 19.34	$0.75^{+0.0078}_{-0.0079}$	$0.124^{+0.015}_{-0.013}$	$1.46^{+0.01}_{-0.01}$	-	YES
NGC 1132	02 : 52 : 51.79 − 01 : 16 : 29.13	$1.23^{+0.015}_{-0.015}$	$1.18^{+0.18}_{-0.14}$	$0.969^{+0.066}_{-0.066}$	-	YES
RX J0454.8–1806	04 : 54 : 52.34 − 18 : 06 : 55.57	$2.35^{+0.07}_{-0.07}$	$2.81^{+1.38}_{-0.78}$	$0.888^{+0.020}_{-0.020}$	-	YES
ESO 306–G 017	05 : 40 : 06.75 − 40 : 50 : 10.80	$2.71^{+0.07}_{-0.05}$	$0.497^{+0.064}_{-0.057}$	$0.790^{+0.022}_{-0.022}$	-	YES
UGC 842	01 : 18 : 53.67 − 01 : 00 : 06.75	$1.90^{+0.07}_{-0.07}$	$1.75^{+0.22}_{-0.18}$	$1.02^{+0.06}_{-0.06}$	-	YES
RX J1331.5+1108	13 : 31 : 29.65 + 11 : 07 : 57.44	$0.74^{+0.02}_{-0.03}$	$1.01^{+0.38}_{-0.23}$	$1.33^{+0.11}_{-0.11}$	$0.110^{+0.006}_{-0.006}$	YES
cl1159p5531	11 : 59 : 52.20 + 55 : 32 : 06.29	$1.69^{+0.018}_{-0.019}$	$0.261^{+0.032}_{-0.028}$	$1.78^{+0.20}_{-0.20}$	$0.285^{+0.005}_{-0.005}$	YES
cl2220m5228*	22 : 20 : 08.64 − 52 : 27 : 50.33	$4.12^{+0.38}_{-0.35}$	$20.9^{+2.74}_{-2.34}$	$0.264^{+0.037}_{-0.037}$	$0.062^{+0.006}_{-0.006}$	NO
cl1416p2315*	14 : 16 : 27.39 + 23 : 15 : 22.59	$2.74^{+0.22}_{-0.22}$	$5.39^{+0.69}_{-0.61}$	$0.500^{+0.049}_{-0.049}$	$0.067^{+0.005}_{-0.005}$	YES
cl0245p0936*	02 : 45 : 48.83 + 09 : 36 : 37.30	$2.45^{+0.38}_{-0.31}$	$4.99^{+0.90}_{-0.76}$	$0.790^{+0.028}_{-0.028}$	$0.116^{+0.012}_{-0.012}$	YES
cl1340p4017*	13 : 40 : 32.70 + 40 : 17 : 39.26	$1.42^{+0.12}_{-0.10}$	$3.29^{+0.53}_{-0.44}$	$0.620^{+0.025}_{-0.025}$	$0.179^{+0.011}_{-0.011}$	YES
RX J2247.4 + 0337*	22 : 47 : 27.88 + 03 : 37 : 00.22	$2.43^{+0.44}_{-0.35}$	$15.9^{+3.58}_{-2.84}$	$0.359^{+0.036}_{-0.036}$	$0.060^{+0.006}_{-0.006}$	NO
RX J0825.9+0415	08 : 25 : 57.83 + 04 : 14 : 47.12	$4.91^{+0.33}_{-0.33}$	$5.16^{+0.76}_{-0.55}$	$0.486^{+0.073}_{-0.073}$	$0.086^{+0.006}_{-0.006}$	YES
RX J1256.0 + 2556*	12 : 56 : 02.25 + 25 : 56 : 35.38	$3.13^{+0.75}_{-0.51}$	$24.2^{+5.15}_{-3.84}$	$0.250^{+0.045}_{-0.045}$	$0.074^{+0.010}_{-0.010}$	NO
RX J0801+3603	08 : 00 : 56.81 + 36 : 03 : 23.67	$8.13^{+0.30}_{-0.30}$	$2.25^{+0.32}_{-0.24}$	$0.844^{+0.034}_{-0.034}$	$0.120^{+0.003}_{-0.003}$	YES
RX J1115.9+0130	11 : 15 : 51.80 + 01 : 29 : 55.48	$7.22^{+0.31}_{-0.31}$	$0.617^{+0.038}_{-0.036}$	$1.21^{+0.03}_{-0.03}$	$0.224^{+0.005}_{-0.005}$	YES
RX J10159.8–0850	01 : 59 : 49.36 − 08 : 49 : 59.45	$8.56^{+0.50}_{-0.39}$	$0.594^{+0.039}_{-0.037}$	$1.10^{+0.02}_{-0.02}$	$0.223^{+0.006}_{-0.006}$	YES

the scatter, it is clear that the anti-correlation trend between the quantities is quite strong with Spearman correlation coefficients of −0.91 and −0.90 respectively.

Assuming no significant effect of selection bias on the sample, to the best of our knowledge, this is the first demonstrated result that suggests that most fossils are in fact cool-core systems based on observable diagnostics. The fraction of cool-core fossil systems is marginally higher than that typically reported for objectively selected group (77%, Bharadwaj et al. 2014) and cluster samples (72%, Hudson et al. 2010). The high CC fossils fraction is not totally unexpected as it is generally assumed that fossils are among the most relaxed clusters/groups in the Universe and hence should have pronounced cool-cores with very short CCTs. What is more intriguing is the fact that the WCC fraction is the highest among the three classes, and the population of WCC and NCC fossils combined together (collectively called non-strong cool-cores; NSCCs) *exceed* the SCC fossils population. This is not what one would naively expect from ostensibly relaxed objects such as these.

6.3.2 EP-BCG/EP-EWC separation

We also quantified the dynamical state of the fossil system via two properties, namely the emission peak–emission weighted centre (EWC) separation and the central elliptical galaxy–EP separation, i.e. the BCG–EP separation. These are reasonable indicators of whether the system is relaxed or not, as large values for these numbers would indicate a disturbed system (e.g. Hudson et al. 2010).

The EWC was determined iteratively in a point source subtracted, exposure-corrected image by starting off from the EP as was done in Hudson et al. (2006). The positions of the BCG were taken from literature and was confirmed from the NASA extragalactic database (NED)[2].

[2] http://ned.ipac.caltech.edu/

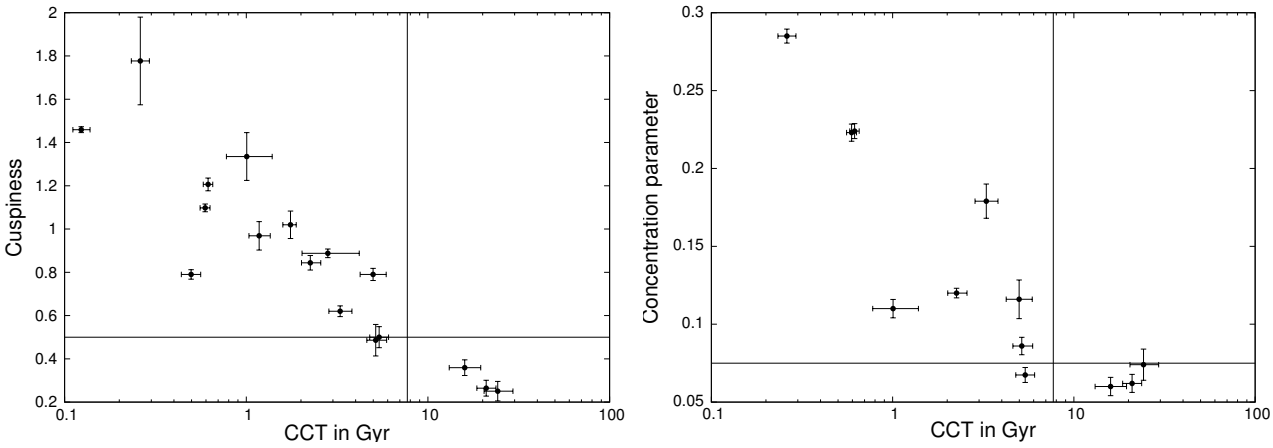

Figure 6.1: Plot of CCT vs. cuspiness (left) and CCT vs. concentration parameter (right). The horizontal lines represent the cut for being classified as a cool-core system. The vertical line represents CCT = 7.7 Gyr.

Table 6.3 shows the EP–EWC and EP–BCG separation. All fossils have their BCG located within 50 kpc of the X-ray peak. The EP–EWC peak shows a wider range of values with four fossils (24%) having a separation $\geq$ 50 kpc. Despite most fossils having an EP–EWC separation less than 50 kpc, again such a large variation in EP–EWC values is not naively expected for ostensibly relaxed systems such as fossils.

6.3.3 Temperature profiles

Appendix C shows the scaled temperature profiles for the fossil systems for which we could obtain one (11 objects). There's a great degree of variation in the profile shapes with temperature drops and flat shapes for the fossil systems and we fail to pinpoint a "typical" temperature profile for the fossils. The high redshift, high temperature systems show temperature profiles that are expected for a SCC/WCC cluster, i.e. indications of a temperature drop for the SCC objects and a relatively flat profile for the WCC objects (Hudson et al. 2010). NGC 6482 shows a profile that rises all the way to the centre which has been reported thoroughly in previous studies of the object (Khosroshahi et al. 2004). NGC 1132 shows an almost a flat profile with barely a decline towards the centre. ESO306, RX J0454.8–1806, and UGC00842 lacks a smooth temperature decline towards the centre which while indicative of a cool-core, shows that it's a truncated one. One possibility for the shape of such a temperature profile could be emission from the BCG, which we discuss in Sec. 6.3.4. A deprojection analysis (Sec. 6.3.5) for the $z < 0.05$ systems indicates the imprint of a heating process such as AGN. Indeed, only cl1159p5531 shows the "classic", peaky temperature profile observed for groups with a SCC (Sun et al. 2009; Eckmiller et al. 2011) versus that for clusters which show flattening at intermediate radii (Vikhlinin et al. 2006).

6.3.4 Potential emission from the BCG

As shown in Table 6.3 most fossils have a BCG which is very close to or on the X-ray peak. The source detection tool `wavdetect` manages to detect sources which seem to be coincident with the BCG in most cases and we explored whether part of the emission in the core regions comes from the BCG itself, i.e. if they are coronae which consists of gas of stellar origin. This could in principle also explain the truncated cool-cores seen in objects such as UGC00842, ESO306, and RX J0454.8–1806. To study this emission,

Table 6.3: EP–BCG, EP–EWC separation. The columns are (1) name of system, (2) separation between BCG and EP in kpc, (3) separation between EP and EWC in kpc. The uncertainty on these quantities correspond to $1''$ which in turn corresponds to 0.27 kpc for the nearest fossil, and 5.41 kpc for the furthest one.

Name	BCG-EP (kpc)	EP-EWC (kpc)
NGC 6482	0.212	1.16
NGC 1132	0.785	5.90
RX J0454.8–1806	3.22	13.3
ESO 306–G 017	0.842	13.3
UGC 842	0.960	2.87
RX J1331.5+1108	1.71	14.8
cl1159p5531	3.77	4.40
cl2220m5228	3.71	62.8
cl1416p2315	0.964	17.5
cl0245p0936	2.78	32.4
cl1340p4017	3.46	30.4
RX J2247.4+0337	2.93	59.2
RX J0825.9+0415	3.58	52.0
RX J1256.0+2556	6.6	61.2
RX J0801+3603	1.29	29.5
RX J1115.9+0130	7.88	21.4
RX J10159.8–0850	4.31	19.5

we focused our attention only on the fossil systems with $z < 0.1$, as it becomes harder to resolve potential coronae for high redshift objects. Using the regions generated by `wavdetect` we extracted spectra which were fit to an absorbed APEC model. The regions used for the spectral extraction are of the order of a few kpc, which is the typical size of a corona. Our estimated temperatures from the spectral fit is in most cases much higher ($\geq$ 1 keV) than that is typically observed for the corona class. Moreover, the X-ray luminosity of the emission is in the order of 10^{41} erg/s which is an order of magnitude higher than what is typically observed for coronae (Sun et al. 2007) and accounts for as much as 17% of the total fossil ROSAT luminosity. Lastly, the abundances are much lower (median of 0.28) than what has been reported for true coronae (0.8, Sun et al. 2007) which gives indications that the detected emission might not be completely of stellar origin, though we do point out that there is evidence from literature for low-metallicity coronae as well (e.g. Sanders et al. 2014b). One strong possibility is that the stellar content has mixed with the surrounding dense ICM. Table 6.4 shows the properties of the emission associated with the BCG.

6.3.5 Deprojection analysis of $z < 0.05$ fossils

In order to explore thermodynamic properties of fossil systems in detail, we focused in particular on the low redshift ($z < 0.05$) fossils and performed a deprojection analysis. To do this, we adopted the MBPROJ code (Sanders et al. 2014a) which is based on the surface brightness deprojection method of Fabian et al. (1981) and is used to estimate the ICM thermodynamical properties from the surface brightness profiles. This method potentially has the advantage of resolving the extreme inner regions of the galaxy group which cannot be probed with traditional spectral analysis in the absence of very high quality data. Additionally, this is a good opportunity to test the code on low temperature groups to see how well the results agree with spectral analysis and test the usability of the code for situations where

Table 6.4: X-ray emission coincident with the BCG for $z \leq 0.1$ fossils.

Name	T (keV)	$Z_\odot$	L_X (0.5–2.0keV)(10^{41} erg/s)	% of ROSAT group emission
NGC 6482	$0.95^{+0.022}_{-0.022}$	$0.28^{+0.08}_{-0.06}$	1.05	17%
NGC 1132	$0.82^{+0.06}_{-0.08}$	$0.11^{+0.05}_{-0.04}$	1.78	3.8%
RX J0454.8–1806	$1.04^{+0.16}_{-0.08}$	$0.40^{+0.55}_{-0.19}$	1.06	1.2%
ESO 306–G 017	$1.30^{+0.04}_{-0.05}$	$0.29^{+0.12}_{-0.09}$	6.46	2.4%
UGC 842	$1.39^{+0.13}_{-0.07}$	$0.21^{+0.11}_{-0.07}$	1.78	7.1%
RX J1331.5+1108	$0.89^{+0.063}_{-0.034}$	$0.15^{+0.54}_{-0.10}$	1.84	2.9%
cl1159p5531	$1.28^{+0.02}_{-0.02}$	$0.38^{+0.06}_{-0.05}$	17.2	15%

spectral analysis would not be possible (e.g. survey data).

For purposes of brevity we refrain from describing the code in detail and guide the reader to the aforementioned paper. The relevant information for this particular study are as follows:

- Surface brightness profiles were extracted in the 0.5–1, 1–1.5, 1.5–2.5, 2.5–7 keV bands.
- We focused only on the "null potential" case for this particular study. This particular case does not assume hydrostatic equilibrium and essentially corresponds to low resolution spectral fitting. The advantage of this case is that it prevents the thermodynamic profiles from being biased due to assumption of hydrostatic equilibrium. The null potential case can be used to estimate thermodynamic properties with and without linear interpolation of the temperatures between the bins. The non-interpolation case assumes the temperature is the same in groups of 3 bins. For the scientific discussion here, we focused only on the profiles which do not involve linear interpolation of the temperatures.
- The abundance is assumed to be $0.3Z_\odot$ throughout.

Figure 6.2 shows a comparison of the temperature profiles from the spectral analysis and MBPROJ. The code does a good job of recovering the shape of the temperature profiles though some deviations are seen for NGC 1132 and NGC 6482 which could be due to the extremely low temperatures of these systems (1.2 and 0.75 keV respectively), and possible projection effects. For the hotter groups, the agreement is much better. Overall though, MBPROJ seems to be a competitive code even on the group regime and would be particularly useful for eROSITA data where most systems would be galaxy groups and would lack sufficient counts even for a simple spectral temperature estimate (Borm et al. 2014).

Figure 6.3 shows the cooling time and the entropy profiles of the fossil systems. The cooling time profiles can be well-described by a powerlaw with an index varying from 1.06±0.03 to 1.20±0.05 for the five systems. Hudson et al. (2010) define the cooling radius as the radius at which $t_{\rm cool}$ = 7.7 Gyr. For these five fossils, namely, NGC 1132, RX J0454.8–1806, ESO306, NGC 6482, and UGC 00842, this corresponds to 43 kpc, 36 kpc, 51 kpc, 54 kpc, and 30 kpc respectively. However, as shown in Fig. 6.2, the region with the cool gas (if present) is generally much smaller than the cooling radius. MBPROJ detects cool gas out to 3 kpc for NGC 1132, 12 kpc for RX J0454.8–1806, 9 kpc for ESO306, 0 kpc for NGC 6482, and 19 kpc for UGC 00842. Thus, all these systems seem to lack a group-sized cool-core and the region of cool gas is not commensurate to the region of short cooling times. As argued above, it seems unlikely that the cool gas component is emission purely associated with the BCG. The slope of

Table 6.5: Best-fit results for Entropy profiles of $z < 0.05$ fossils. Columns are (1) Name of group, (2) Slope, (3) Normalisation

Name	slope	normalisation (keV cm^2)
NGC 6482	0.77 ± 0.04	3.20 ± 0.27
NGC 1132	0.78 ± 0.02	4.29 ± 0.39
RX J0454.8–1806	0.75 ± 0.03	6.50 ± 0.66
ESO 306–G 017	0.85 ± 0.02	3.74 ± 0.39
UGC 842	0.77 ± 0.02	6.75 ± 0.57

the entropy profiles of the fossils, also fit to a powerlaw, deviate significantly from the typical value of 1.1 (Table 6.5) which is expected for pure gravitational process (e.g. Tozzi & Norman 2001), though that relation strictly holds true only for regions outside the core (Voit et al. 2005). Recently, Panagoulia et al. (2014) showed that the overall entropy profile for a sample of galaxy groups and clusters can be well-described by a powerlaw model ($K(r) = \alpha \times (r/(100\ \mathrm{kpc}))^{\beta}$) without indications of a core-flattening that had been previously reported in literature (Cavagnolo et al. 2009). This powerlaw model describes the overall entropy profile of our fossils quite well too with $\alpha = 185.3 \pm 6.13$ keV cm^2 and $\beta = 0.86 \pm 0.02$ (vs. $\alpha = 95.4$ and $\beta = 0.7$ in Panagoulia et al. 2014). The shallow powerlaw indices points to a strong influence of non-gravitational processes on the properties of the ICM, which we discuss in greater detail in Sec. 6.3.7.

6.3.6 L_X–T relation for 400d fossil systems

The L_X–T relation is an interesting scaling relation which can give insights into the baryonic physics at play in the ICM as they affect both quantities, T and L_X. For example, clusters with cool-cores/non-cool cores have L_X–T relations with different slopes and normalisations (Mittal et al. 2011). Note that selection effects can play a significant role in determining the true L_X–T scaling relation (e.g. Mittal et al. 2011; Lovisari et al. 2015; Bharadwaj et al. 2015) and hence simply using an archival sample of clusters/groups to construct scaling relations would not result in an accurate description of the underlying properties of the objects. Since this study contains fossil systems from the 400d catalogue, and the selection criteria are well-defined, we attempt to present a bias-corrected L_X–T relation for fossils for the first time. All 400d fossils which have either Chandra or XMM-Newton data (seven) have been used for this study. The correction for selection effects was done using the method described in Bharadwaj et al. (2015) with the slight change that the intrinsic scatter in L_X was kept frozen at all times to the observed value. The selection criteria for the 400d fossil sample was taken from Voevodkin et al. (2010) and are: a lower flux cut of 1.4×10^{-13} erg/s/cm^2, an upper redshift cut of 0.2, and a lower luminosity cut of $10^{43} h_{71}^{-2}$ ergs^{-1}. The fluxes and luminosities are in the ROSAT (0.5–2.0 keV) band. To compare the L_X–T relation to bias-corrected relations for clusters and groups, we converted the ROSAT luminosities to the bolometric (0.01–40 keV) luminosities like in Mittal et al. (2011) and Bharadwaj et al. (2015). We used the BCES (Y|X) code by Akritas & Bershady (1996) and the fits were performed in Log space using the fitting function

$$\left(\frac{L_X}{0.5 \times 10^{44}\ h_{71}^{-2} \mathrm{erg\ s^{-1}}}\right) = c \times \left(\frac{T}{3\ \mathrm{keV}}\right)^{m} \tag{6.18}$$

The observed best-fit L_X–T relation has a slope of 2.24±0.50 and normalisation of 0.31±0.10. Fig. 6.4 (left) shows the observed and bias-corrected L_X–T relation for the 400d fossils. The normalisation for

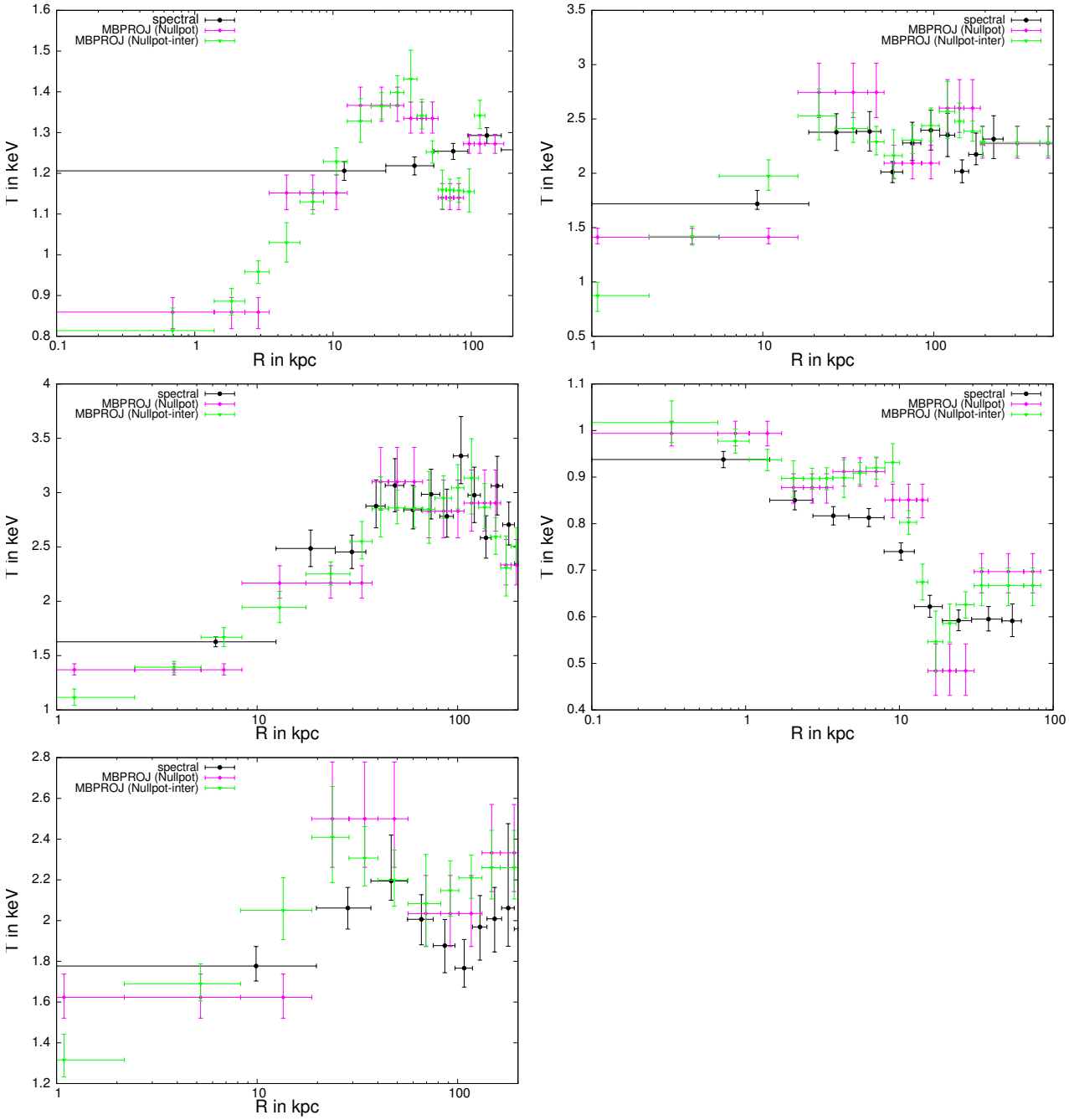

Figure 6.2: Temperature profiles of the fossil systems, from spectral analysis and MBPROJ. *Clockwise from top left*: NGC 1132, RXJ 0454.8–1806, NGC 6482, ESO306, UGC 00842. The spectral temperature profiles were also determined for an abundance of $0.3Z_{\odot}$.

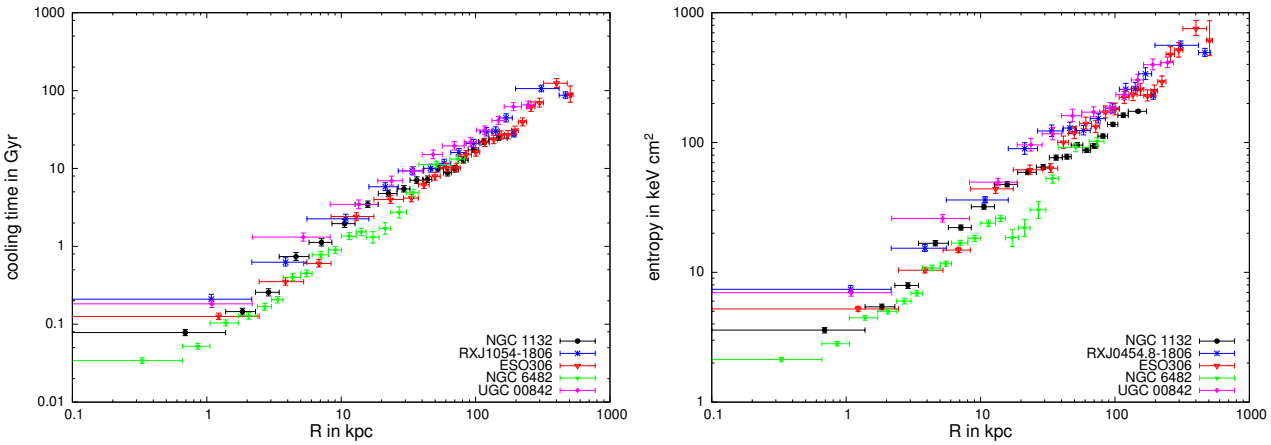

Figure 6.3: *Left:* Cooling time profiles of $z < 0.05$ fossils. *Right:* Entropy profiles of $z < 0.05$ fossils.

Table 6.6: The bias-corrected L_X–T relation for the 400d fossil systems compared to the results of Bharadwaj et al. (2015). Errors are the measurement errors from observations.

Type	Slope (m)	Normalisation (log c)
400d fossils	2.48 ± 0.50	0.27 ± 0.10
All groups	3.20 ± 0.26	0.08 ± 0.09
NSCC groups	2.52 ± 0.39	-0.17 ± 0.11

the bias-corrected relation is lower and the slope is marginally steeper (2.48 vs. 2.24). When the bias-corrected L_X–T relation for the fossils is compared to the bias-corrected relations for the groups sample of Bharadwaj et al. (2015) (Fig. 6.4 (right), table 6.6), it is seen that there are indications that the slope of the L_X–T relation for the 400d fossils is shallower than the reported slope for the group sample of Bharadwaj et al. (2015) and the normalisation seems to be higher for fossil systems, i.e. fossils seem to be more X-ray luminous for a given T for most of the temperature range covered here. Interestingly, the slope of the bias-corrected L_X–T relation for the fossil systems is comparable to the bias-corrected slope for NSCC groups in Bharadwaj et al. (2015) (2.48 vs. 2.52), albeit with much higher normalisations. Qualitatively, our results shows indications of being different to those of Khosroshahi et al. (2007) and Miller et al. (2012) who state that the L_X–T relations for fossils do not deviate significantly to that of non-fossils. Table 6.2 gives indications that most of the 400d fossils are NSCC groups which could partially explain the L_X–T relation, particularly the shallow slope. Additionally, the high X-ray normalisations might provide indications of an early formation epoch relative to non-fossils, but we do point out that the X-ray luminosities in the 400d catalogue and the ones in the catalogues on which the Bharadwaj et al. (2015) study is based, are not determined homogeneously which could partially explain the elevated values. Lastly, we are mindful of the fact that despite our attempt to obtain a bias-corrected L_X–T relation for fossil systems, given the extremely small sample size, potential archival bias, and the limited data quality for most of these objects, we can only give some hints at this stage and are unable to derive statistically significant bias-corrected scaling relations.

6.3.7 Discussion

Though our results concern mostly the cores of fossil systems, these properties offer us interesting insights into their formation and evolution. Fossil systems not having experienced any recent major

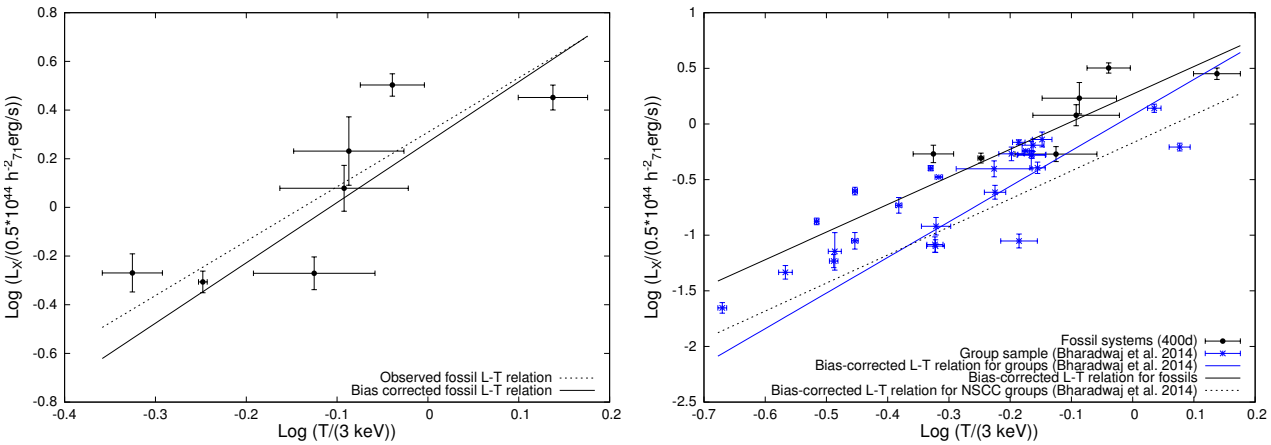

Figure 6.4: *Left:* Observed and bias-corrected L_X–T relation for 400d fossils. *Right:* Comparison of bias-corrected 400d fossil L_X–T relation to Bharadwaj et al. (2015).

merger activity should have a pronounced cool-core with very short CCTs and "typical" temperature profiles with a clear central temperature drop. The distribution of the CCTs and the shapes of the observed temperature profiles does not however seem to support this idea. Given that the BCG–EP separation is not large and that most fossils still have an EP–EWC separation less than 50 kpc, it seems unlikely that invoking mergers can easily explain the thermodynamic properties of the fossils.

A lot of these properties can be explained due to a non-gravitational process, in particular the AGN activity at the centres, which we speculate was much more powerful at an earlier epoch than it is now. Simulation results by e.g. Dariush et al. (2007) and Díaz-Giménez et al. (2011) point out that fossils assemble most of their masses at high redshifts. Interestingly, Díaz-Giménez et al. (2008) point out that while the virial mass of the groups were assembled at high redshifts, much of the BCG mass is assembled at much later epochs. Recent results by Méndez-Abreu et al. (2012) conclude that the BCGs of fossils underwent major dissipational mergers at earlier epochs, albeit most of the stellar content was assembled via dissipationless major mergers at later times. Thus, we speculate that during the relatively "gas-rich" phase of mass assembly, the SMBH was strongly fuelled which led to strong AGN feedback such that an almost isothermal central region, or a centrally rising temperature profile was formed. When this phase ended, dissipationless major mergers continued to build the BCG, but there wasn't enough gas to fuel the SMBH strongly pushing it into a state of relative quiescence. Eventually, for some objects, a small cool-core region was formed probably from the mixture of stellar mass ejecta and the surrounding ICM, not quite unlike thermal coronae seen in groups/clusters. This cool gas started feeding the SMBH, and is now probably involved in a self-regulated feedback cycle which leads to a much lower AGN activity. Four out of the five $z < 0.05$ fossils show extremely weak radio sources (Bharadwaj et al. 2014; Miraghaei et al. 2014; Condon et al. 1998) indicating that the AGN activity is definitely not strong currently, giving credence to this theory. Interestingly, simulation results by Burns et al. (2008) indicate that non cool-core clusters (cool-cores here are defined by a central temperature drop in the temperature profile) at low redshifts ($z < 0.3$) have less halos in their neighbourhood as compared to CC clusters, while the situation was exactly reversed at $z > 1$. Though Burns et al. (2008) only discuss about clusters with virial masses greater than 10^{14} $M_\odot$, the under dense regions of fossil systems relative to other systems would seem to qualitatively agree with the idea that the progenitors of fossils originated in a region with a higher density of halos that strongly contributed to mergers and the final mass assembly currently resides in a relatively under-dense region. This is also qualitatively

in agreement with the observational results of Harrison et al. (2012) who base their conclusions via a study of the fossil ellipticals, and also the simulation results of Díaz-Giménez et al. (2011).

The above speculation however, still does not explain the "classical" temperature profile seen for cl1159p5531 and the high temperature fossils. One possibility is that the thermodynamic properties of the fossil systems are strongly dependent on the environment in which it was formed and it could be that these anomalous objects grew in a region relatively under-dense in halos that led to the formation of a proper cool-core via hierarchical, small-scale mergers (Burns et al. 2008) and led to relatively gentle AGN feedback throughout. Secondly, we do not rule out the possibility of the high temperature objects being falsely identified as fossils as the Eigenthaler & Zeilinger (2009) sample is largely based on the SDSS catalogue and it has been known for some systems to be wrongly classified as fossils for previous similar samples, only to be corrected later when better data was available (e.g. Zarattini et al. 2014 vs. Santos et al. 2007). Cl1159p5531 has a galaxy just outside the search radius which if included would not satisfy the magnitude criterion of Voevodkin et al. (2010) and be classified as a fossil in that study. Naively though, it seems unlikely that subtle changes in the magnitude gap would have a drastic impact on the ICM properties of these objects.

6.4 Summary

We have studied the core properties of 17 fossil systems from literature with data from the Chandra archives. The conclusions of our work can be summarised as follows:

- Most fossil systems (82%) are identified as cool-core objects based on at least two diagnostics. Interestingly though, there are indications that most fossil systems are WCC objects and that the population of NSCC fossils outstrip SCC fossils.
- Fossil systems show a large range of temperature profiles with many cool-core objects lacking the expected central temperature drop.
- We analysed the X-ray emission coincident with the BCG for fossils with $z < 0.1$ and conclude that these are not the typical X-ray coronae reported for some other objects. We speculate that the stellar X-ray component (if present) has mixed with the ICM.
- We performed a deprojection analysis using the SBPs for fossils with $z < 0.05$ and derived their thermodynamic properties. These objects lack group-sized cool-cores and show evidence for non-gravitational processes (AGN feedback in particular) based on their entropy profiles.
- Using fossil systems from the 400d sample, we show that there are indications that the bias-corrected L_X–T relation for fossils is much shallower than the expected relation and higher in normalisation. Also, there are indications that the slope is consistent with the L_X–T relation for groups lacking strong cool cores.
- We speculate that early, dissipational major mergers led to a strong fuelling of the central SMBH leading to powerful AGN feedback and this could explain the lack of group-sized cool-cores in fossils. There are however anomalous cases which lead us to conclude that this is probably an incomplete picture of the formation and evolution of fossil systems.

In short, we have offered a glimpse into the nature of fossil systems through their core properties. In order to concretise these ideas, we will have to construct large, objectively selected fossils sample with high quality X-ray data; ideally with some mass/luminosity cut to distinguish between fossil groups and

clusters. A key point here seems to be to understand the weak cool-core cluster/group regime which till date has been probed poorly. These observational results will also need backing from detailed, high-resolution simulations which factors in feedback processes that would help us unravel substantial features in the growth of fossil systems and the impact on the properties of the ICM.

CHAPTER 7

Summary and outlook

7.1 Summary of results

In this dissertation, three scientific papers are presented, which together form a detailed investigation of galaxy groups and fossil systems in the X-ray wavelength. The main results of the papers can be summarised as follows:

- The cool-core fraction in the galaxy group regime is comparable to that of the cluster regime.
- Not all galaxy groups with a central cooling time (CCT) less than 1 Gyr have a clear central temperature drop indicative of a cool gas component in the cores of the groups, which is unlike that seen for clusters.
- The radio-loud AGN fraction does not scale as a function of the CCT unlike for clusters.
- The radio AGN output for strong cool-core (SCC) galaxy groups is an order of magnitude lower than that for SCC clusters, and once again no correlation is seen between the radio AGN output and the CCT. Also, the mean radio output for SCC central radio sources (CRS) is a factor of 34 lower than CRSs for non-SCC (NSCC) groups.
- Extending the scaling relation between the brightest cluster galaxy (BCG) near-infrared luminosity and the system X-ray luminosity/mass, to the galaxy group regime, results in an increase in the scatter, and there are potential indications of higher stellar mass content in group BCGs than cluster BCGs.
- A large fraction of fossil systems have a cool-core, indicated by at least two cool-core diagnostics, albeit most of these are weak cool-core systems.
- Fossil systems lack a universal temperature profile, and most low-z fossils in our sample lack the pronounced central temperature drop typically seen in cool-core clusters.
- Brightest cluster galaxies (BCGs) of fossils do not show clear indications of thermal coronae which has been reported in literature for a few galaxies in some clusters. We have speculated that the stellar content has mixed with the surrounding intracluster medium.

- A deprojection analysis of $z < 0.05$ fossils shows that the region of cool gas (if present) is not commensurate with the region of low cooling times, which is much larger. This indicates the impact of non-gravitational processes on the ICM.
- The bias-corrected L_X–T relation in the galaxy group regime is marginally steeper than in the galaxy cluster regime, but the slopes are mutually consistent within the errors.
- The L_X–T relation for SCC groups has the largest slope and also has the largest normalisation (L_X) relative to the scaling relation for non-SCC (NSCC) groups. This can be explained by the enhanced luminosities of these systems which is due to their relatively high central densities.
- There are indications that the L_X–T relation for groups hosting a central radio AGN with extended emission are steeper than those for groups hosting a radio AGN with only central emission.
- The bias-corrected intrinsic scatter increases from the cluster to the group regime. Additionally, the "observed" scatter for groups is lower than the "true" scatter possibly due to selection effects.
- There are indications that the slope of the bias-corrected L_X–T relation for fossil systems are lower (~ 2.5) than typically seen for other groups and clusters (~ 3), though this is comparable to groups which lack a SCC.

7.2 Outlook

Despite presenting many exciting results for galaxy groups and fossil systems, the work presented in this dissertation has raised several interesting scientific questions which are worthy of investigation in the near future. Here, a quick overview of three scientific questions raised by each study is presented, and the methods with which one can address them in a practical way.

Star formation in cool-core galaxy groups An important question raised by the work in this dissertation is how star formation fits within the ICM cooling–AGN feedback paradigm in galaxy groups, i.e. how do the star formation rates in cool-core galaxy groups compare to the gas deposition rates in the central regions of groups? A project to study the correlation of ICM cooling and star formation rates in galaxy groups, and to potentially identify differences, if any, with respect to clusters is thus worth pursuing. Hα data for the BCGs of galaxy groups can give an estimation of the star formation rate which can then be used to study star formation in the group regime.

Detailed, multi-wavelength study of fossil systems The results presented in the fossil systems study is only a primer for more detailed, future studies about this exciting class of galaxy clusters and groups which will be conducted with larger samples. However, as iterated time and again throughout this dissertation, archival samples of galaxy clusters/groups are not advisable as they can result in biased conclusions. The first step would be to construct an objectively selected sample of fossil systems which can then be used for multi-wavelength follow-up. As a starting point, one could identify fossil systems in the new REFLEX-II catalogue (Böhringer et al. 2014), which consists of galaxy clusters in the southern sky down to a X-ray flux limit of 1.8×10^{-12} erg s^{-1} cm^{-2}. Additionally, while observational results has given important information about the properties of fossil systems, understanding their formation and evolution, particularly of the ICM is still a challenge. A detailed investigation via simulations is thus required to constrain the ICM properties of fossil progenitors and to study how the thermodynamic properties are impacted as they evolve into the ostensibly relaxed systems that one observes in the present day.

Extending X-ray scaling relations to lower masses The scaling relations results presented in this dissertation are still somewhat incomplete as there is still a lack of many systems below 1 keV. Extending the scaling relation to lower temperatures (and masses) would be important in order to see if the scaling relations show a gradual steepening, and/or whether a clear similarity break is visible at some point on the temperature scale. Recent results by Anderson et al. (2014) show that the L_X–M_{500} scaling relation can be expressed by a power law for a large range of masses extending from the cluster regime to the galaxy regime with an index steeper than theoretical expectations. These results rely on a combination of simulations and ROSAT observations, and would require a proper observational follow-up by careful analysis of X-ray data from telescopes such as Chandra and XMM-Newton, and careful handling of selection effects. It is worth stating here that we are currently exploring the L_X–T relation for a flux-limited sample of elliptical galaxies, and very preliminary results suggest that the relation steepens quite significantly for those objects.

7.2.1 eROSITA outlook on the gas mass in galaxy clusters

The eROSITA all-sky survey is poised to generate a large amount of galaxy cluster/groups data and as mentioned many times throughout this dissertation, most would lack enough photons for an accurate mass estimate, which is the most relevant physical quantity for cosmological studies. The gas mass (M_{gas}) however requires a much lower number of X-ray photons for measurement, as one just needs to get the shape and normalisation of the surface brightness profile (SBP) which when fit with various models can be used to obtain the density profile and the gas mass thereon. Scaling relations between M_{gas} and the total mass (M_{tot}) can then be used to estimate the mass of the cluster which can then be used to construct the cluster mass function and cosmological parameters thereon. The big advantage of using an M_{gas}–M_{tot} scaling relation is the significantly reduced intrinsic scatter as compared to using the X-ray luminosity (Kravtsov et al. 2006). Additionally, Borm et al. (2014) show that there are around 2000 clusters for which the temperature can be estimated with an uncertainty less than 10% with only the all-sky survey data. The product of M_{gas} and T is called the Y_X parameter which has the smallest intrinsic scatter for a cluster mass proxy (Kravtsov et al. 2006). Thus, it is interesting to test how well eROSITA would recover cluster gas masses, which we studied via pilot X-ray simulations. We describe the procedure and the first results briefly here.

For this pilot study, we used the simulation of X-ray telescopes (SIXTE) software by C. Schmid[1]. Starting from the total mass (M_{500}) of the galaxy cluster and scaling relations from Reichert et al. (2011) and Lovisari et al. (2015), the input T (in keV) and M_{gas} (in $M_\odot$) were obtained respectively as:

$$\left(\frac{T}{\mathrm{keV}}\right) = \left(\frac{3.44 \times M_{500}}{10^{14} M_\odot}\right)^{0.62} E(z)^{0.64}, \tag{7.1}$$

$$\log\left(\frac{M_{gas}}{5 \times 10^{12} M_\odot}\right) = 1.22 \times \log\left(\frac{M_{500}}{5 \times 10^{13} M_\odot}\right) - 0.16, \tag{7.2}$$

where $E(z) = \left[\Omega_m(1+z)^3 + \Omega_\Lambda\right]^{\frac{1}{2}}$ is the assumed redshift evolution term, where $\Omega_m = 0.3$, and $\Omega_\Lambda = 0.7$. The Hubble constant is taken to be 70 km/s/Mpc in this work.

The next step is to make a list of core radii and beta values which would be used for describing the SBP of the galaxy cluster[2]. The core radius (r_c in kpc) was determined from M_{500} using a scaling relation from Chen et al. (2007)

[1] http://www.sternwarte.uni-erlangen.de/research/sixte/
[2] We only focused on a single beta model in this study

$$\log\left(\frac{r_c}{100\ \mathrm{kpc}}\right) = 0.253 + 1.18 \times \log\left(\frac{M_{500}}{5 \times 10^{14} M_\odot}\right). \tag{7.3}$$

An intrinsic scatter in r_c was also introduced which was determined from the data of Chen et al. (2007). This core radius was used to determine the input beta (β) using a scaling relation from Neumann & Arnaud (1999):

$$\beta = 0.55 \times \left[1 + \left(\frac{r_c}{885\ \mathrm{kpc}}\right)^2\right]. \tag{7.4}$$

The r_c and β values give the shape of the input density profiles for an input M_{gas}. One can thus determine the input central electron density value (n_0) for a combination of r_c, β and M_{gas}. The next step is to generate the relevant input files for the simulator. The primary file is the so-called simulation input (SIMPUT[3]) file which contains the cluster co-ordinates, the flux of the cluster, and the spectral model of the cluster emission (APEC is used here). The cluster spectral model requires four quantities, namely a temperature (estimated from the scaling relation stated above), an abundance for the cluster ICM (assumed to be $0.3 Z_\odot$ throughout), a redshift (varied from 0.1–0.5 depending on the simulation), and the normalisation, which was estimated from the density profile using the formula

$$\left(\frac{N}{\mathrm{cm}^{-5}}\right) = \left[\frac{10^{-14}}{D_A^2 (1+z)^2} \int_0^{r_{500}} \frac{n^2(r)}{1.2} r^2 \mathrm{d}r\right], \tag{7.5}$$

where $n(r)$ is the density profile given by the single beta model making the input APEC normalisation of the cluster dependent on the input density profiles. The factor of 1.2 is essentially the ratio of electrons to protons, assuming the plasma is fully ionised with 10% Helium.

The input image of the galaxy cluster was generated by using the model of the SBP, which was estimated from the beta profile. The cosmic X-ray background was accounted for with relevant background files (credit: K. Borm). The source and background input files were then passed through the simulator in the all-sky survey mode to generate the events files, with the simulator also applying the particle background for eROSITA. Images were extracted in the 0.5–2.0 keV band which was then used to extract the SBPs, and a single beta model was fit to it to obtain the output r_c and β. To estimate the output n_0, one needs an estimation of the output APEC normalisation. This was determined by estimating the X-ray count rate in a large region, and using an APEC model in *Xspec* to match the observed count rate. The *Xspec* model assumes a temperature of 3 keV and an abundance of $0.3 Z_\odot$. Note that since the count rate is estimated in the 0.5–2.0 keV band, the dependence on temperature is not expected to be too significant for most of the masses probed here. Using the output APEC normalisation, and the determined r_c and β, we calculated the value of M_{gas}. The steps described here were repeated 10 times, by generating new events files each time (each events file contains 36 clusters, with each cluster having a different r_c and β), and finally a distribution of M_{gas} values was obtained, and the median M_{gas} was compared to the input value.

Figure 7.2 shows a plot of the ratio of the output gas mass (median) from the simulations to the input gas mass as a function of the total mass of the cluster. The error bars on the ratio of gas masses correspond to the standard deviation of the distribution of the output gas masses. We ran the simulations for different masses in three redshifts, 0.1, 0.3, and 0.5. The preliminary results show that for lower cluster masses, the eROSITA all-sky survey over-estimates the gas masses, and it under-estimates the masses towards the higher mass end. Expectedly, the standard deviation decreases with increasing mass.

[3] http://hea-www.harvard.edu/heasarc/formats/simput-1.1.0.pdf

The estimation of the gas masses is relatively stable with increase in redshift, with only an increase in the standard deviation of the gas mass distribution. These results are an encouraging start, but a lot more has to be done before making robust forecasts for the survey. An outstanding issue, which is not trivial, would be to take into account the point spread function (PSF) of the eROSITA telescopes in the analysis of the simulated images.

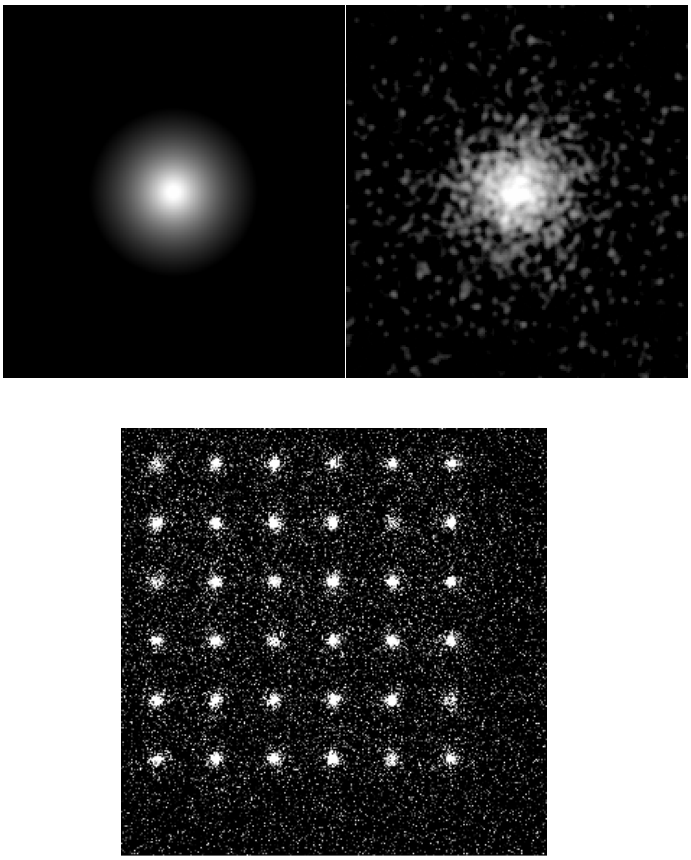

Figure 7.1: *Top:*Comparison of an eROSITA observation (right) for an input galaxy cluster (left). The cluster is of mass $3 \times 10^{14} M_{\odot}$ and $z = 0.1$, while the observation corresponds to an exposure time of 1.6 kiloseconds. *Bottom:* eROSITA observation of the same cluster with different input core radii and beta. The size of the image is 3.6×3.6 deg^2.

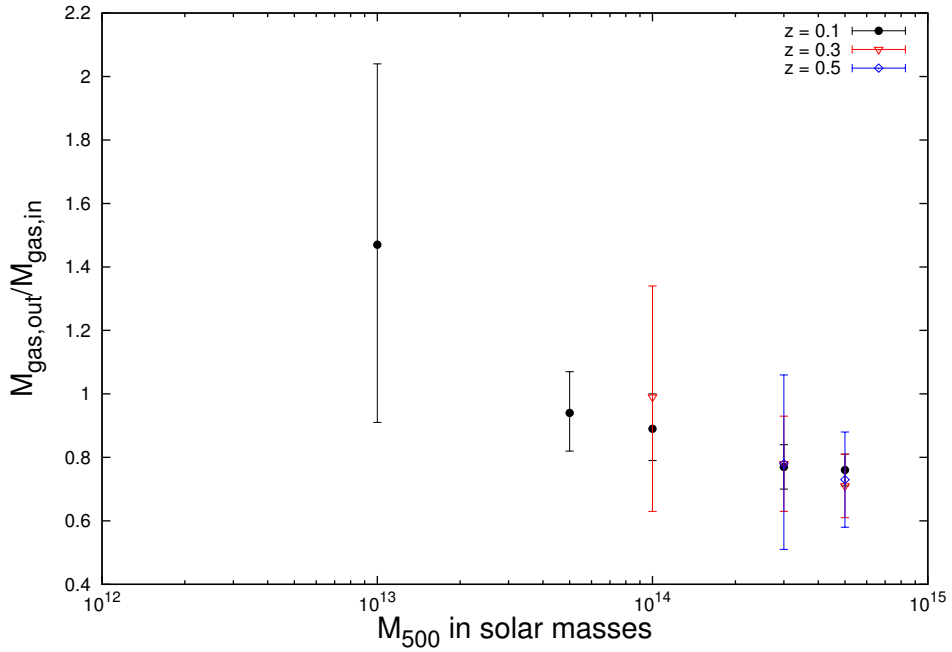

Figure 7.2: Ratio of output (median) gas mass from simulations to the input gas mass as a function of the total mass of the cluster.

APPENDIX A

Calculation of scatter for $L_{\rm X}$–$L_{\rm BCG}$ and M_{500}–$L_{\rm BCG}$ scaling relations

We give the formula for the calculation of scatter given in Table 4.3, which is based on the weighted sample variance in the log-log plane (Arnaud et al. 2005; Mittal et al. 2011). Here, "raw" is the raw scatter, "stat" is the statistical scatter.

$$
\begin{aligned}
\sigma^2_{\rm raw,\ L_{BCG}} &= {\rm C}_{L_{\rm BCG}} \sum_{i=1}^{N} \frac{1}{\sigma^2_{i,\ L_{\rm BCG}}} \left[\log(L_{\rm BCG_i}) - (\log c + m\log(L_{\rm X_i}))\right]^2 \\
{\rm C}_{L_{\rm BCG}} &= \frac{1}{(N-2)} \frac{N}{\sum_{i=1}^{N}(1/\sigma^2_{i,\ L_{\rm BCG}})} \\
\sigma^2_{\rm raw,\ L_X} &= C_{L_{\rm X}} \sum_{i=1}^{N} \frac{1}{\sigma^2_{i,\ L_{\rm X}}} \left[\log(L_{\rm X_i}) - (\log(L_{\rm BCG_i}) - \log c)/m\right]^2 \\
{\rm C}_{\rm L_X} &= \frac{1}{(N-2)} \frac{N}{\sum_{i=1}^{N}(1/\sigma^2_{i,\ L_{\rm X}})}
\end{aligned}
$$

where $\sigma^2_{i,\ L_{\rm BCG}} = (\Delta\log(L_{\rm BCG_i}))^2 + m^2(\Delta\log(L_{\rm X_i}))^2$,

$\sigma^2_{i,\ L_{\rm X}} = (\Delta\log(L_{\rm X_i}))^2 + (\Delta\log(L_{\rm BCG_i}))^2/m^2$,

Here, N is the sample size, c is the normalisation, m is the slope and the deltas represent the errors on the quantities. The statistical scatter, $\sigma_{\rm stat}$, is estimated by calculating the root-mean-square of σ_i. The intrinsic scatter is given as the difference between the raw and the statistical scatters in quadrature. We simply replace M_{500} in place of $L_{\rm X}$ in the formula to calculate scatter for the M_{500}–$L_{\rm BCG}$ relation.

APPENDIX B

Temperature profiles of the galaxy group sample in Chapter 4

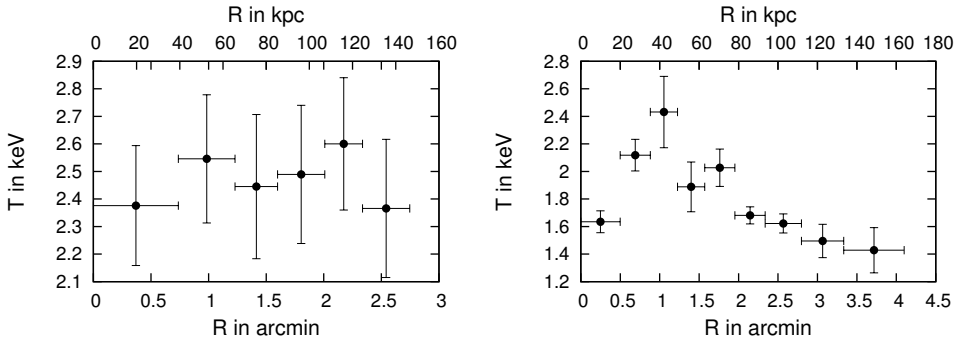

Figure B.1: Temperature profiles of A0160 (left) and A1177 (right).

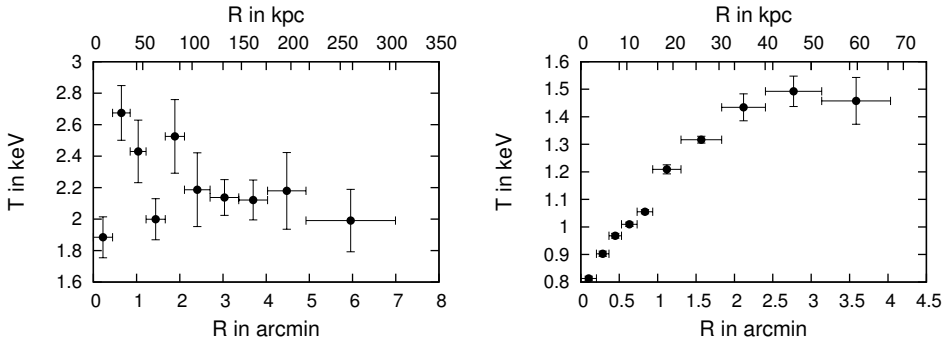

Figure B.2: Temperature profiles of ESO 55 (left) and HCG 62 (right).

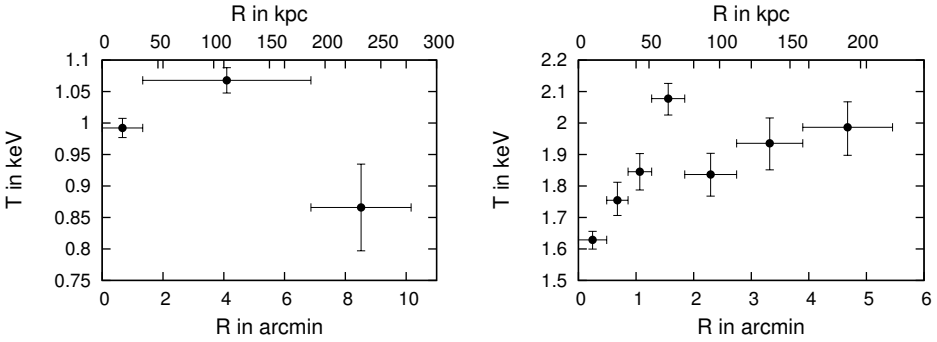

Figure B.3: Temperature profiles of HCG 97 (left) and IC 1262 (right).

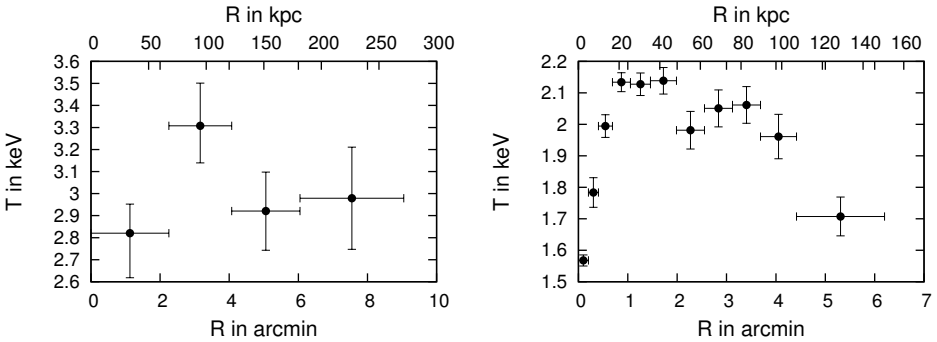

Figure B.4: Temperature profiles of IC 1633 (left) and MKW 4 (right).

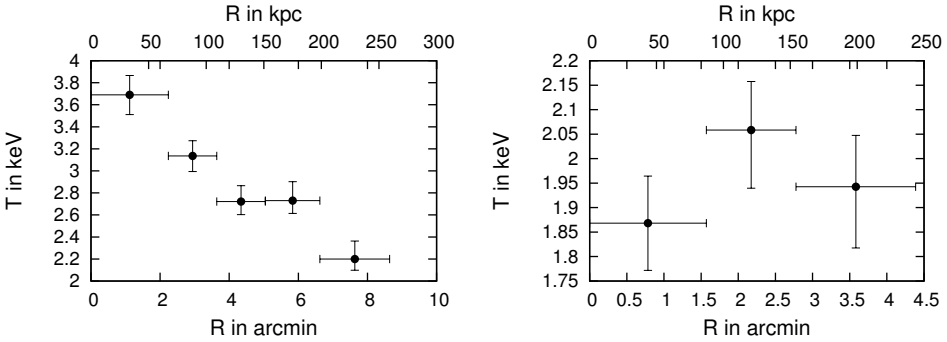

Figure B.5: Temperature profiles of MKW 8 (left) and NGC 326 (right).

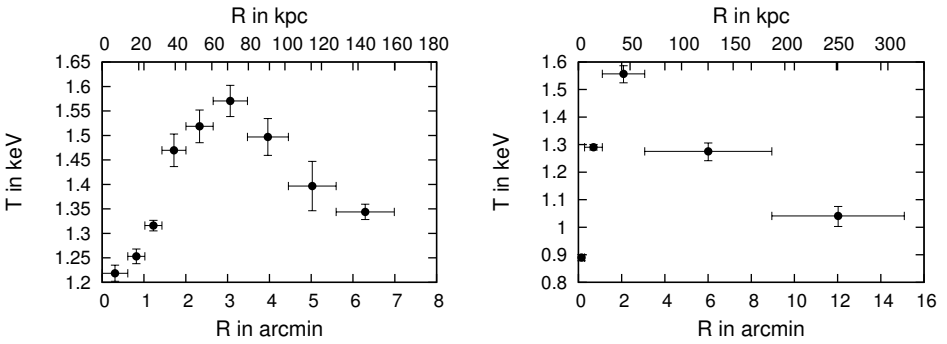

Figure B.6: Temperature profiles of NGC 507 (left) and NGC 533 (right).

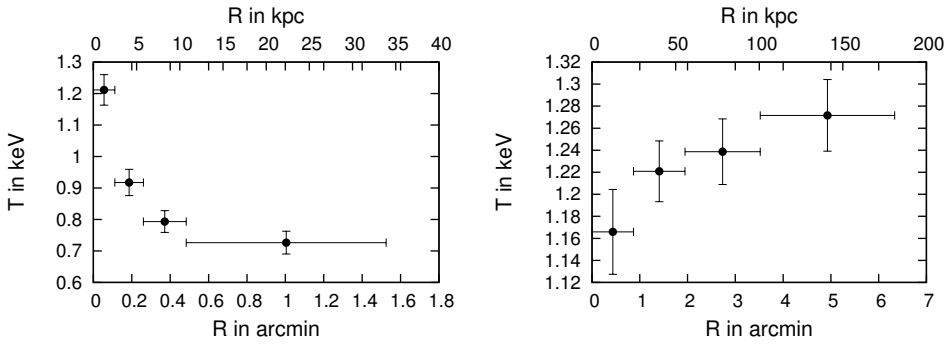

Figure B.7: Temperature profiles of NGC 777 (left) and NGC 1132 (right).

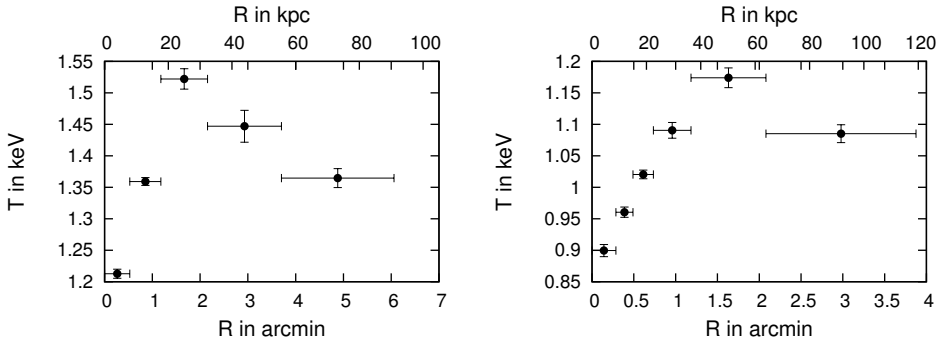

Figure B.8: Temperature profiles of NGC 1550 (left) and NGC 4325 (right).

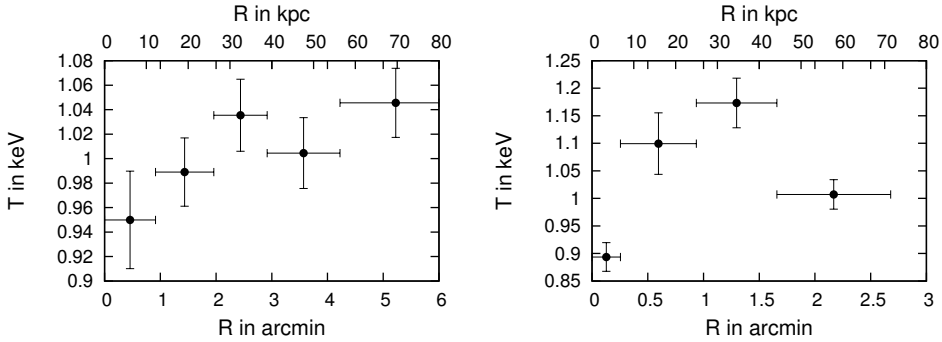

Figure B.9: Temperature profiles of NGC 4936 (left) and NGC 5129 (right).

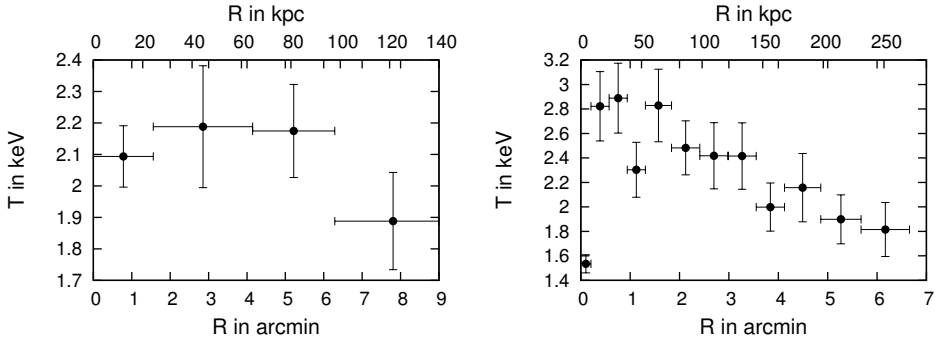

Figure B.10: Temperature profiles of NGC 5419 (left) and NGC 6269 (right).

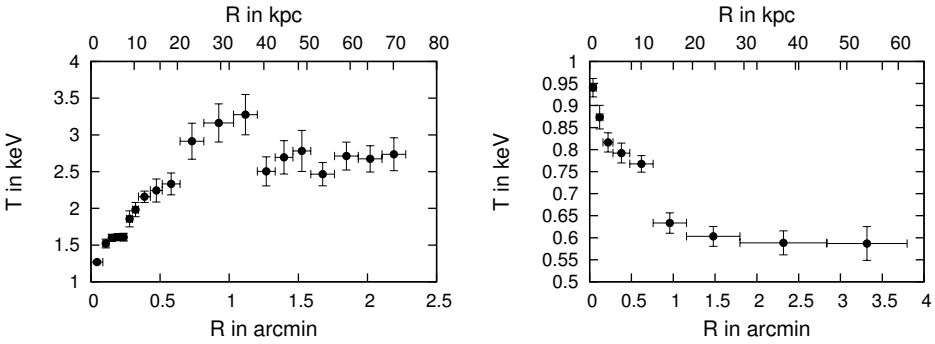

Figure B.11: Temperature profiles of NGC 6338 (left) and NGC 6482 (right).

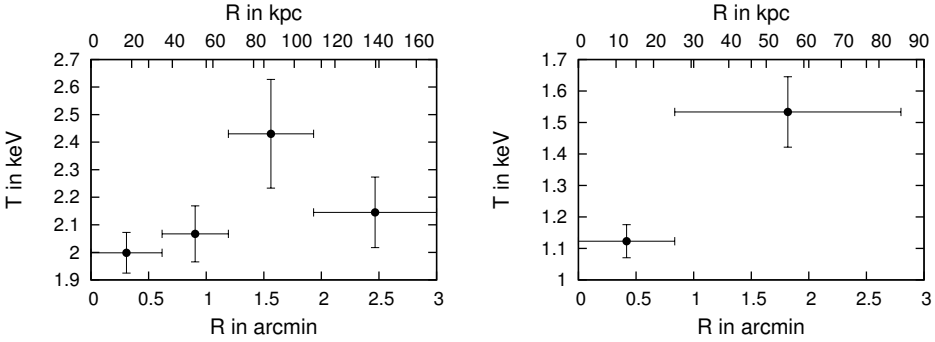

Figure B.12: Temperature profiles of RXCJ 1022 (left) and RXCJ 2214 (right).

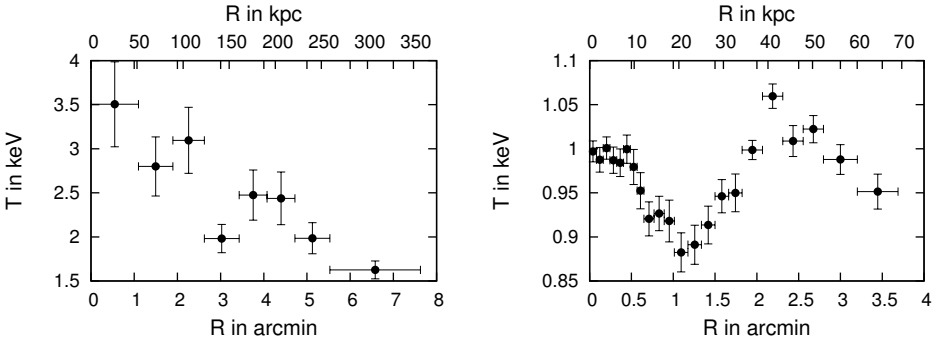

Figure B.13: Temperature profiles of S0463 (left) and SS2B153 (right).

APPENDIX C

Temperature profiles of the fossil systems in Chapter 6

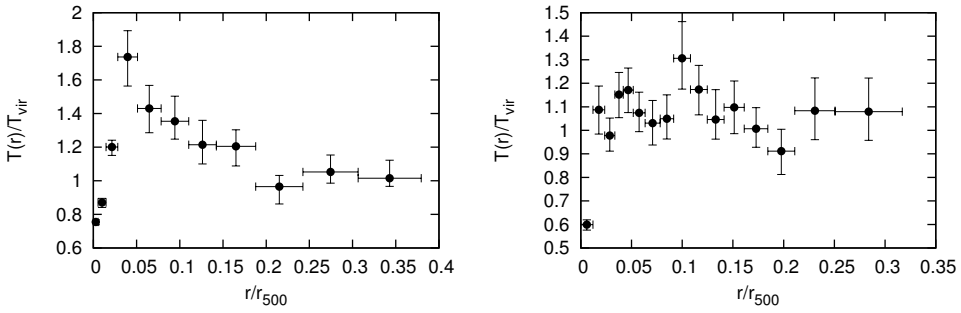

Figure C.1: Scaled temperature profiles of Cl1159p5531 (left) and ESO306 (right).

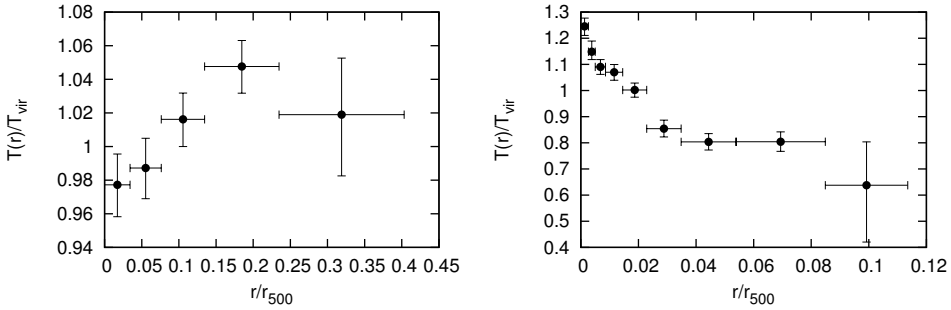

Figure C.2: Scaled temperature profiles of NGC 1132 (left) and NGC 6482 (right).

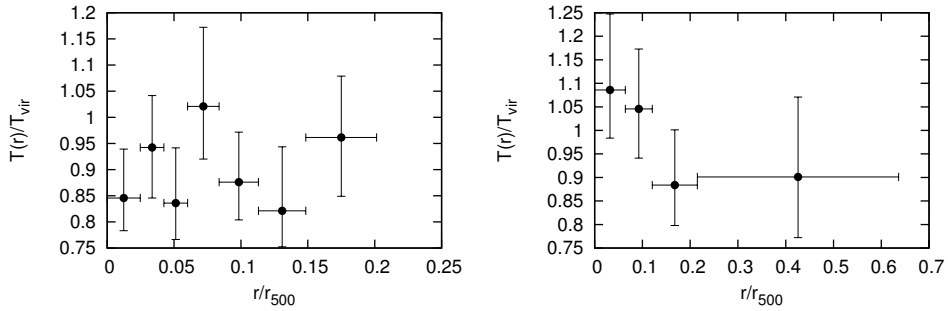

Figure C.3: Scaled temperature profiles of RX J0801+3603 (left) and RX J0825.9+0415 (right).

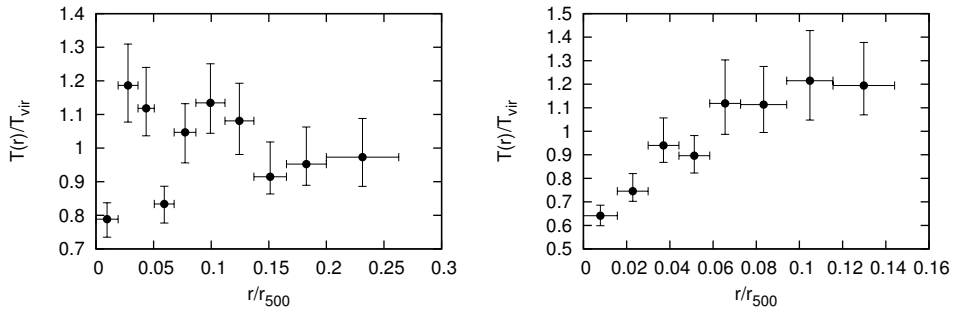

Figure C.4: Scaled temperature profiles of RX J0454.8–1806 (left) and RX J1115.9+0130 (right).

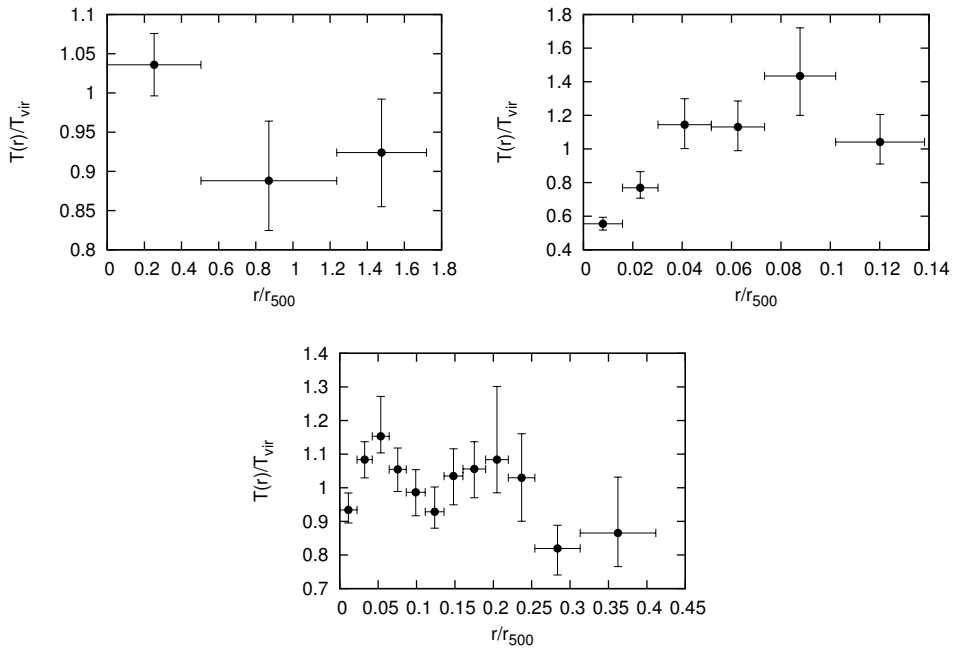

Figure C.5: Scaled temperature profiles of RX J1331+1108 (top left), RX J10159.8–0850 (top right), and UGC00842 (bottom). For RX J1331+1108, the blank-sky files might be under-estimating the background beyond r_{500}. This should however not be a problem in the central regions.

APPENDIX D

NVSS radio contours on optical images for some groups in Chapter 4

Here, we present 1.4 GHz NVSS radio contours (green) overlaid on optical images from SAO-DSS with the EP marked (red X). Co-ordinates are sexagesimal Right Ascension and Declination.

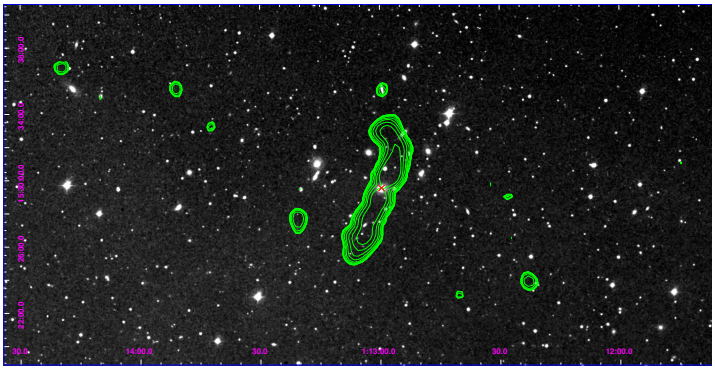

Figure D.1: A0160.

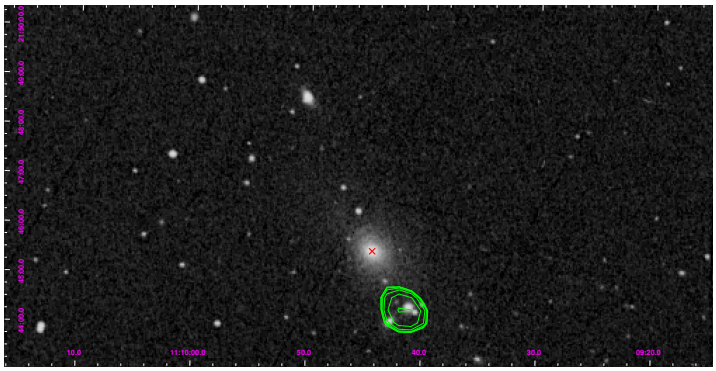

Figure D.2: A1177.

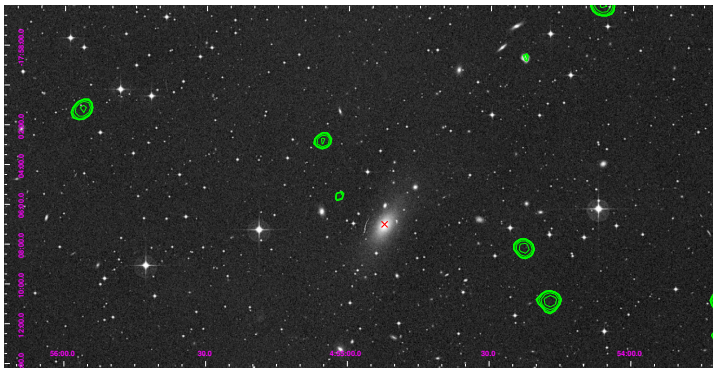

Figure D.3: ESO55

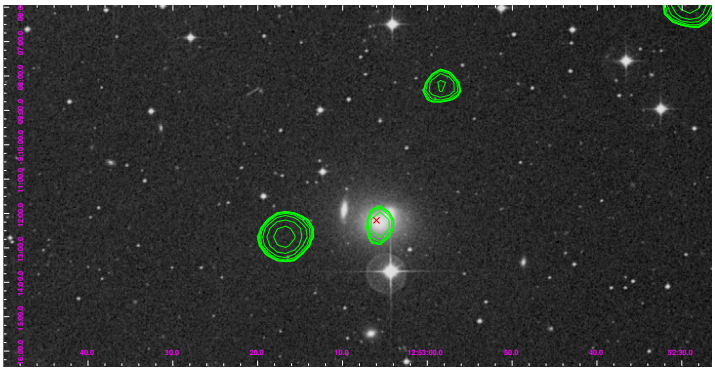

Figure D.4: HCG62.

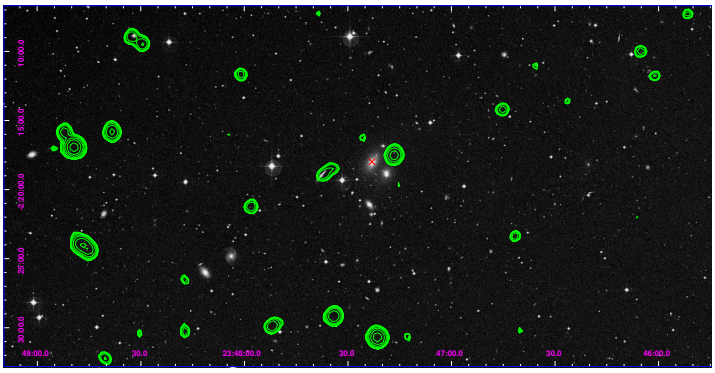

Figure D.5: HCG97.

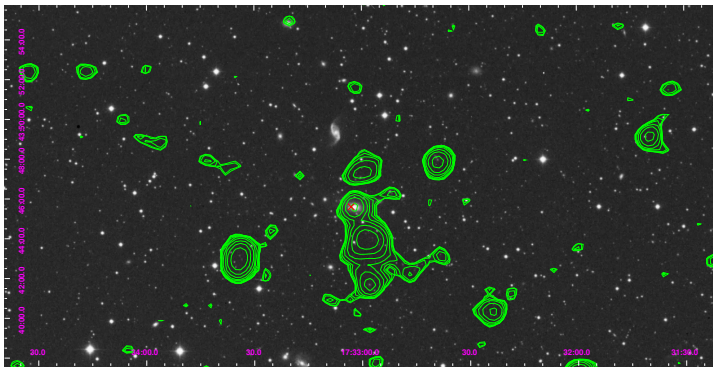

Figure D.6: IC1262.

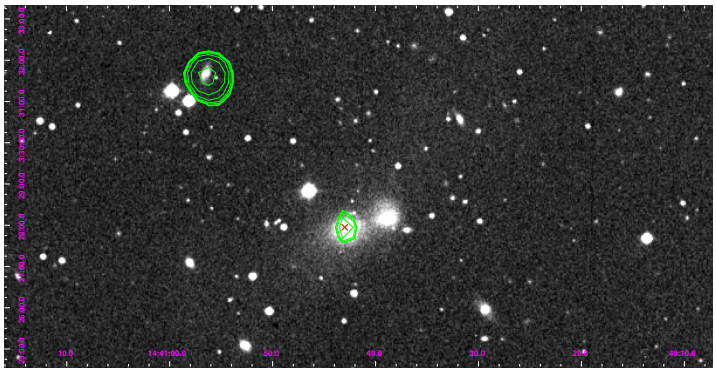

Figure D.7: MKW8.

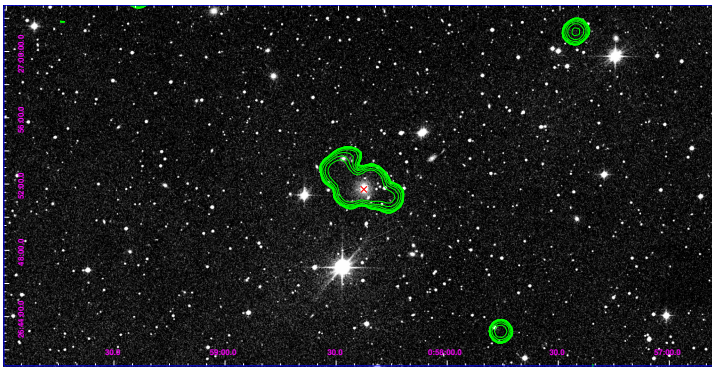

Figure D.8: NGC326.

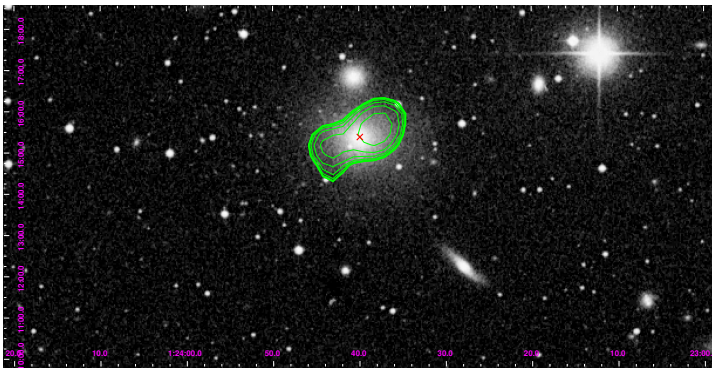

Figure D.9: NGC507.

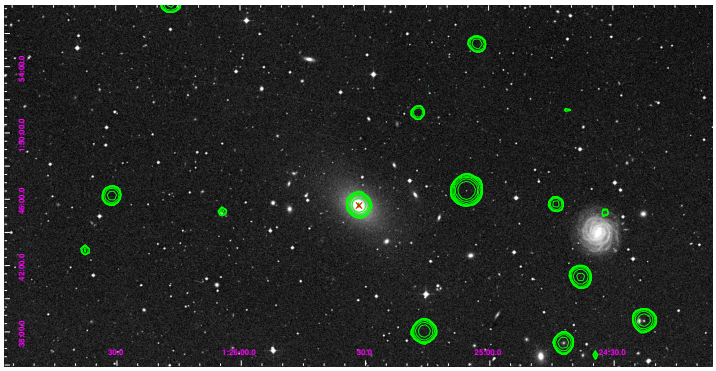

Figure D.10: NGC533.

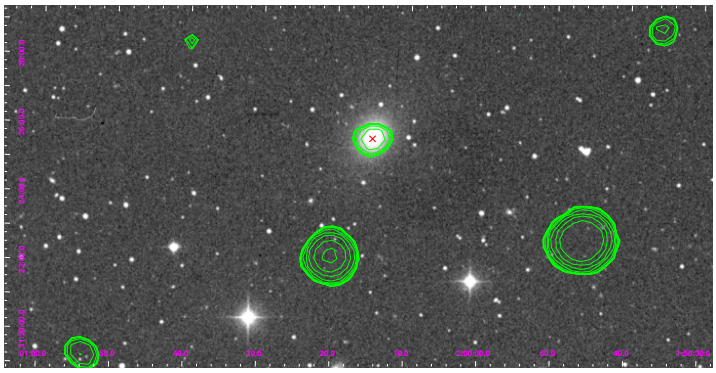

Figure D.11: NGC777.

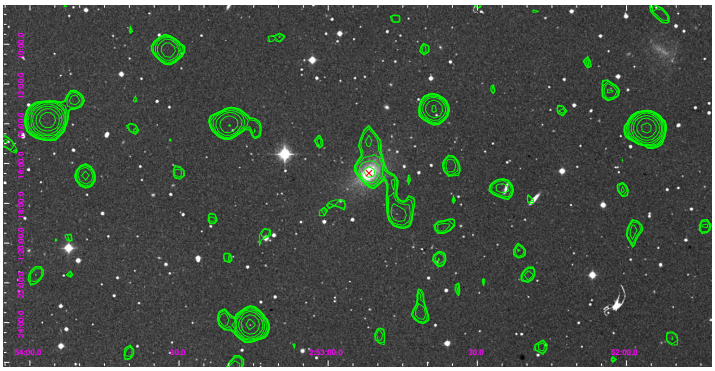

Figure D.12: NGC1132.

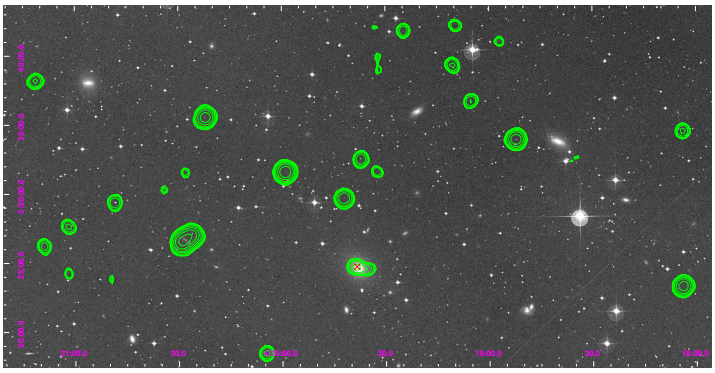

Figure D.13: NGC1550.

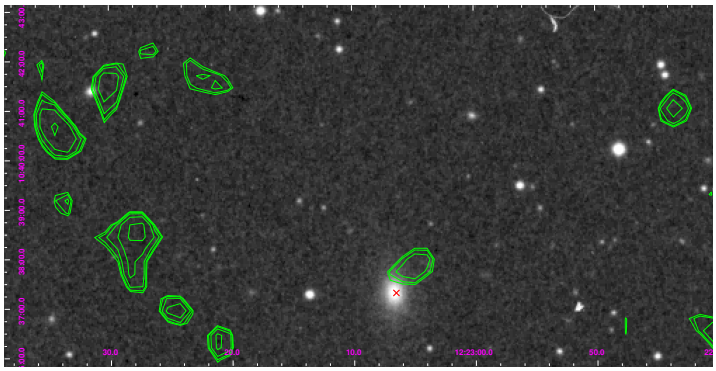

Figure D.14: NGC4325.

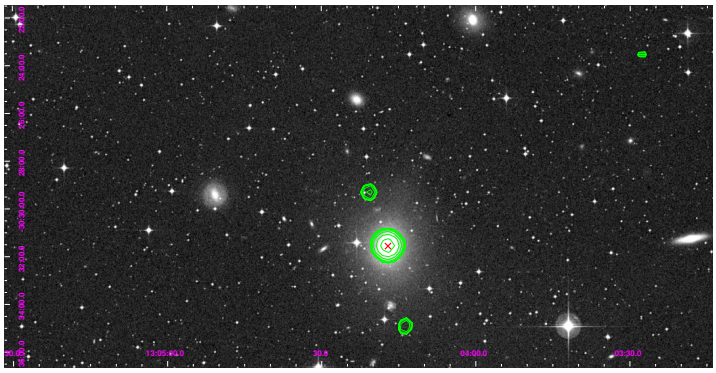

Figure D.15: NGC4936.

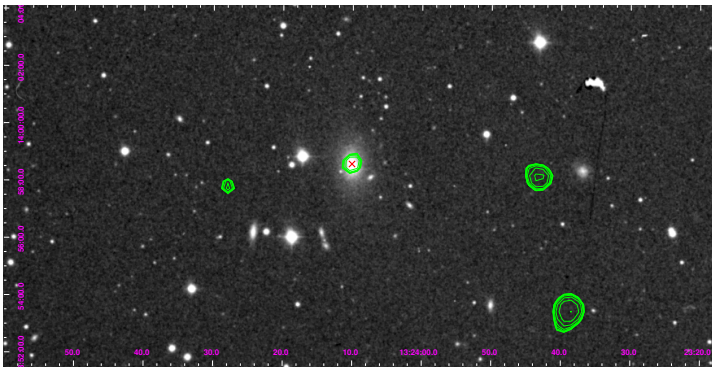

Figure D.16: NGC5129.

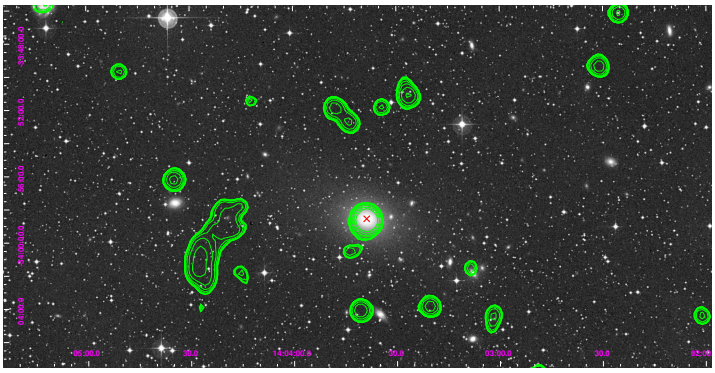

Figure D.17: NGC5419.

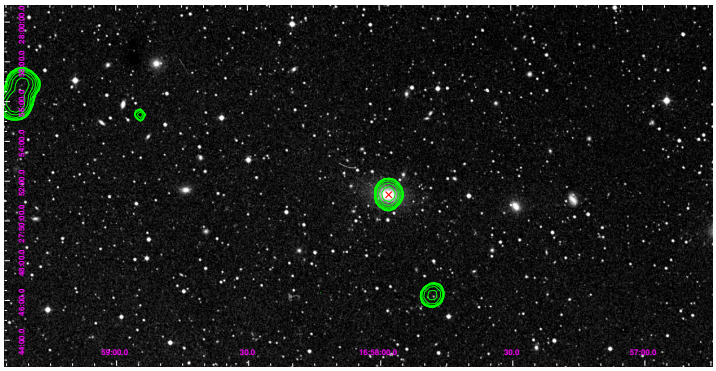

Figure D.18: NGC6269.

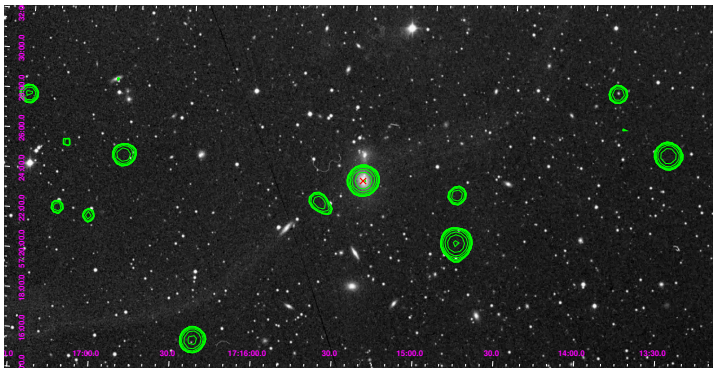

Figure D.19: NGC6338.

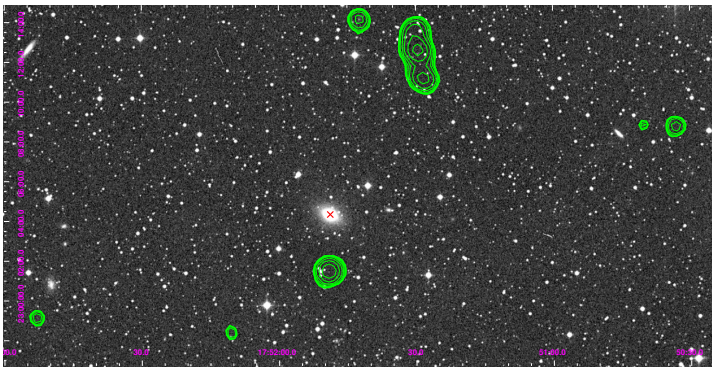

Figure D.20: NGC6482.

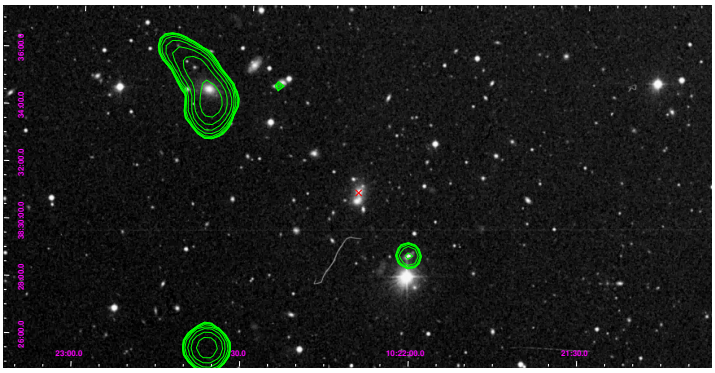

Figure D.21: RXCJ1022.

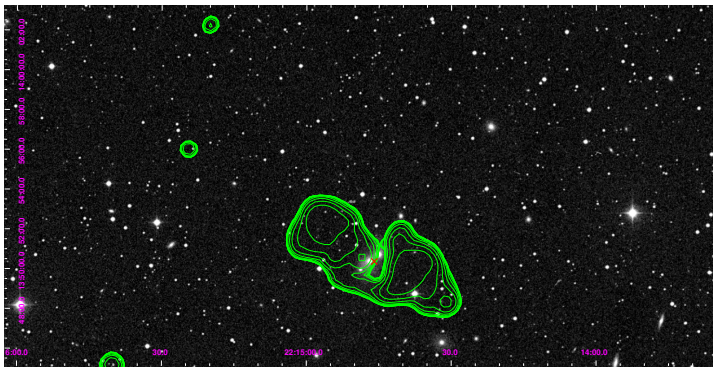

Figure D.22: RXCJ2214.

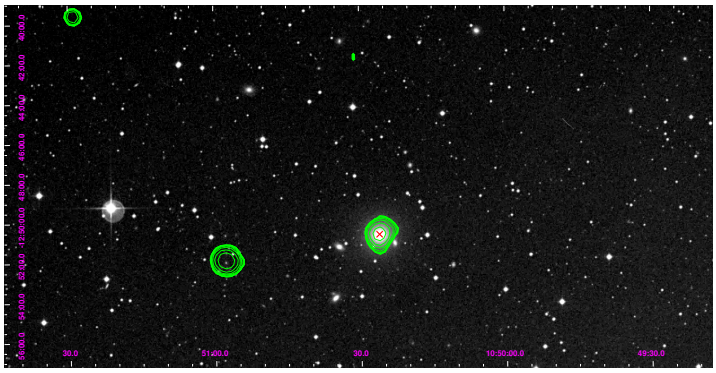

Figure D.23: SS2B.

Bibliography

Abell, G. O. 1958, ApJS, 3, 211

Akritas, M. G. & Bershady, M. A. 1996, ApJ, 470, 706

Albrecht, A., Bernstein, G., Cahn, R., et al. 2006, ArXiv e-prints 0609591

Allen, S. W. 1995, MNRAS, 276, 947

Allen, S. W., Schmidt, R. W., & Fabian, A. C. 2001, MNRAS, 328, L37

Anders, E. & Grevesse, N. 1989, GCA, 53, 197

Anderson, M. E., Gaspari, M., White, S. D. M., Wang, W., & Dai, X. 2014, ArXiv e-prints 1409.6965

Arnaud, M. & Evrard, A. E. 1999, MNRAS, 305, 631

Arnaud, M., Pointecouteau, E., & Pratt, G. W. 2005, A&A, 441, 893

Arnaud, M., Rothenflug, R., Boulade, O., Vigroux, L., & Vangioni-Flam, E. 1992, A&A, 254, 49

Aschenbach, B. 1985, Reports on Progress in Physics, 48, 579

Ashman, K. M., Bird, C. M., & Zepf, S. E. 1994, AJ, 108, 2348

Bartalucci, I., Mazzotta, P., Bourdin, H., & Vikhlinin, A. 2014, ArXiv e-prints 1404.3587

Batcheldor, D., Marconi, A., Merritt, D., & Axon, D. J. 2007, ApJL, 663, L85

Bell, E. F. & de Jong, R. S. 2001, ApJ, 550, 212

Bharadwaj, V. 2011, MSc. thesis, Rheinische Friedrich-Wilhelms-Universität Bonn

Bharadwaj, V., Reiprich, T. H., Lovisari, L., & Eckmiller, H. J. 2015, A&A, 573, A75

Bharadwaj, V., Reiprich, T. H., Schellenberger, G., et al. 2014, A&A, 572, A46

Birkinshaw, M. 1999, physrep, 310, 97

Bîrzan, L., McNamara, B. R., Nulsen, P. E. J., Carilli, C. L., & Wise, M. W. 2008, ApJ, 686, 859

Bîrzan, L., Rafferty, D. A., McNamara, B. R., Wise, M. W., & Nulsen, P. E. J. 2004, ApJ, 607, 800

Blanton, E. L., Sarazin, C. L., McNamara, B. R., & Wise, M. W. 2001, ApJL, 558, L15

Blumenthal, Faber S. M., Primack Joel R., & Rees Martin J. 1984, Nature, 311, 517, 10.1038/311517a0

Bock, D. C.-J., Large, M. I., & Sadler, E. M. 1999, AJ, 117, 1578

Böhringer, H., Chon, G., Collins, C. A., et al. 2014, ArXiv e-prints 1403.5886

Böhringer, H., Schuecker, P., Guzzo, L., et al. 2004, A&A, 425, 367

Böhringer, H., Voges, W., Fabian, A. C., Edge, A. C., & Neumann, D. M. 1993, MNRAS, 264, L25

Böhringer, H., Voges, W., Huchra, J. P., et al. 2000, ApJS, 129, 435

Bolzonella, M., Miralles, J.-M., & Pelló, R. 2000, A&A, 363, 476

Borgani, S., Murante, G., Springel, V., et al. 2004, MNRAS, 348, 1078

Borm, K., Reiprich, T. H., Mohammed, I., & Lovisari, L. 2014, A&A, 567, A65

Burns, J. O., Hallman, E. J., Gantner, B., Motl, P. M., & Norman, M. L. 2008, ApJ, 675, 1125

Burrows, C. J., Burg, R., & Giacconi, R. 1992, ApJ, 392, 760

Carlstrom, J. E., Holder, G. P., & Reese, E. D. 2002, ARAA, 40, 643

Cavagnolo, K. W., Donahue, M., Voit, G. M., & Sun, M. 2009, ApJS, 182, 12

Cavaliere, A. & Fusco-Femiano, R. 1976, A&A, 49, 137

Chen, Y., Reiprich, T. H., Böhringer, H., Ikebe, Y., & Zhang, Y.-Y. 2007, A&A, 466, 805

Churazov, E., Brüggen, M., Kaiser, C. R., Böhringer, H., & Forman, W. 2001, ApJ, 554, 261

Churazov, E., Sunyaev, R., Forman, W., & Böhringer, H. 2002, MNRAS, 332, 729

Clarke, T. E., Blanton, E. L., & Sarazin, C. L. 2004, ApJ, 616, 178

Clowe, D., Bradač, M., Gonzalez, A. H., et al. 2006, ApJL, 648, L109

Cohen, A. S., Lane, W. M., Cotton, W. D., et al. 2007, AJ, 134, 1245

Colina, L. & Bohlin, R. 1997, AJ, 113, 1138

Conconi, P., Campana, S., Tagliaferri, G., et al. 2010, MNRAS, 405, 877

Condon, J. J., Cotton, W. D., Greisen, E. W., et al. 1998, AJ, 115, 1693

Cowie, L. L. & Binney, J. 1977, ApJ, 215, 723

Cox, D. P. & Reynolds, R. J. 1987, ARAA, 25, 303

Dariush, A., Khosroshahi, H. G., Ponman, T. J., et al. 2007, MNRAS, 382, 433

Dariush, A. A., Raychaudhury, S., Ponman, T. J., et al. 2010, MNRAS, 405, 1873

Démoclès, J., Pratt, G. W., Pierini, D., et al. 2010, A&A, 517, A52

Díaz-Giménez, E., Muriel, H., & Mendes de Oliveira, C. 2008, A&A, 490, 965

Díaz-Giménez, E., Zandivarez, A., Proctor, R., Mendes de Oliveira, C., & Abramo, L. R. 2011, A&A, 527, A129

D'Onghia, E., Sommer-Larsen, J., Romeo, A. D., et al. 2005, ApJL, 630, L109

Dressel, L. L. & Condon, J. J. 1978, ApJS, 36, 53

Dressler, A. 1980, ApJ, 236, 351

Dressler, A. 1984, ARAA, 22, 185

Dubinski, J. 1998, ApJ, 502, 141

Eckert, D., Molendi, S., & Paltani, S. 2011, A&A, 526, A79+

Eckmiller, H. J., Hudson, D. S., & Reiprich, T. H. 2011, A&A, 535, A105

Edge, A. C. & Frayer, D. T. 2003, ApJL, 594, L13

Edwards, L. O. V., Hudson, M. J., Balogh, M. L., & Smith, R. J. 2007, MNRAS, 379, 100

Eigenthaler, P. & Zeilinger, W. W. 2009, Astronomische Nachrichten, 330, 978

Eke, V. R., Navarro, J. F., & Frenk, C. S. 1998, ApJ, 503, 569

Evrard, A. E., Metzler, C. A., & Navarro, J. F. 1996, ApJ, 469, 494

Fabian, A. C. 1994, ARAA, 32, 277

Fabian, A. C., Hu, E. M., Cowie, L. L., & Grindlay, J. 1981, ApJ, 248, 47

Fabian, A. C. & Nulsen, P. E. J. 1977, MNRAS, 180, 479

Fabian, A. C., Nulsen, P. E. J., & Canizares, C. R. 1984, Nature, 310, 733

Fabian, A. C., Sanders, J. S., Allen, S. W., et al. 2003, MNRAS, 344, L43

Fabricant, D., Rybicki, G., & Gorenstein, P. 1984, ApJ, 286, 186

Ferrarese, L. & Merritt, D. 2000, ApJL, 539, L9

Finoguenov, A., Reiprich, T. H., & Böhringer, H. 2001, A&A, 368, 749

Franceschini, A., Vercellone, S., & Fabian, A. C. 1998, MNRAS, 297, 817

Fujita, Y. & Reiprich, T. H. 2004, ApJ, 612, 797

Fujita, Y., Tawa, N., Hayashida, K., et al. 2008, PASJ, 60, 343

Fukugita, M., Hogan, C. J., & Peebles, P. J. E. 1998, ApJ, 503, 518

Gaspari, M., Brighenti, F., D'Ercole, A., & Melioli, C. 2011, MNRAS, 415, 1549

Gaspari, M., Brighenti, F., Temi, P., & Ettori, S. 2014, ApJL, 783, L10

Giodini, S., Lovisari, L., Pointecouteau, E., et al. 2013, SSR, 177, 247

Giodini, S., Pierini, D., Finoguenov, A., et al. 2009, ApJ, 703, 982

Gitti, M., O'Sullivan, E., Giacintucci, S., et al. 2010, ApJ, 714, 758

Griest, K. 1991, ApJ, 366, 412

Gunn, J. E. & Gott, I. J. R. 1972, ApJ, 176, 1

Guo, F. & Oh, S. P. 2008, MNRAS, 384, 251

Harrison, C. D., Miller, C. J., Richards, J. W., et al. 2012, ApJ, 752, 12

Harrison, F. A., Craig, W. W., Christensen, F. E., et al. 2013, ApJ, 770, 103

Heinz, S., Reynolds, C. S., & Begelman, M. C. 1998, ApJ, 501, 126

Helsdon, S. F. & Ponman, T. J. 2000, MNRAS, 315, 356

Hess, K. M., Wilcots, E. M., & Hartwick, V. L. 2012, AJ, 144, 48

Hickox, R. C. & Markevitch, M. 2006, ApJ, 645, 95

Hicks, A. K., Mushotzky, R., & Donahue, M. 2010, ApJ, 719, 1844

Hopkins, A., Georgakakis, A., Cram, L., Afonso, J., & Mobasher, B. 2000, ApJS, 128, 469

Hudson, D. S., Mittal, R., Reiprich, T. H., et al. 2010, A&A, 513, A37+

Hudson, D. S., Reiprich, T. H., Clarke, T. E., & Sarazin, C. L. 2006, A&A, 453, 433

I. Sakelliou, J. R. Peterson, T. Tamura, et al. 2002, A&A, 391, 903

Ikebe, Y., Reiprich, T. H., Böhringer, H., Tanaka, Y., & Kitayama, T. 2002, A&A, 383, 773

Jarrett, T. H., Chester, T., Cutri, R., et al. 2000, AJ, 119, 2498

Jones, C., Forman, W., Vikhlinin, A., et al. 2002, ApJL, 567, L115

Jones, L. R., Ponman, T. J., Horton, A., et al. 2003, MNRAS, 343, 627

Kaastra, J. S., den Boggende, A. J., Brinkman, A. C., et al. 2001, in Astronomical Society of the Pacific Conference Series, Vol. 234, X-ray Astronomy 2000, ed. R. Giacconi, S. Serio, & L. Stella, 351

Kaiser, N. 1986, MNRAS, 222, 323

Kalberla, P. M. W., Burton, W. B., Hartmann, D., et al. 2005, A&A, 440, 775

Kennicutt, J. R. C. 1998, ARAA, 36, 189

Khosroshahi, H. G., Jones, L. R., & Ponman, T. J. 2004, MNRAS, 349, 1240

Khosroshahi, H. G., Ponman, T. J., & Jones, L. R. 2007, MNRAS, 377, 595

King, I. R. 1966, AJ, 71, 64

King, I. R. 1972, ApJL, 174, L123

Koester, B. P., McKay, T. A., Annis, J., et al. 2007, ApJ, 660, 239

Kormendy, J. & Richstone, D. 1995, ARAA, 33, 581

Kravtsov, A. V., Vikhlinin, A., & Nagai, D. 2006, ApJ, 650, 128

La Barbera, F., de Carvalho, R. R., de la Rosa, I. G., et al. 2009, AJ, 137, 3942

Lacy, M., Laurent-Muehleisen, S. A., Ridgway, S. E., Becker, R. H., & White, R. L. 2001, ApJL, 551, L17

Laganá, T. F., Lima Neto, G. B., Andrade-Santos, F., & Cypriano, E. S. 2008, A&A, 485, 633

Laganá, T. F., Zhang, Y.-Y., Reiprich, T. H., & Schneider, P. 2011, ApJ, 743, 13

Laureijs, R., Amiaux, J., Arduini, S., et al. 2011, ArXiv e-prints 1110.3193

Lea, S. M., Silk, J., Kellogg, E., & Murray, S. 1973, ApJL, 184, L105+

Lin, Y.-T., Mohr, J. J., & Stanford, S. A. 2003, ApJ, 591, 749

Liu, Y., Jiang, D. R., & Gu, M. F. 2006, ApJ, 637, 669

Lopes de Oliveira, R., Carrasco, E. R., Mendes de Oliveira, C., et al. 2010, AJ, 139, 216

Lovisari, L., Reiprich, T. H., & Schellenberger, G. 2015, A&A, 573, A118

Magliocchetti, M. & Brüggen, M. 2007, MNRAS, 379, 260

Makishima, K., Ezawa, H., Fukuzawa, Y., et al. 2001, PASJ, 53, 401

Mantz, A., Allen, S. W., Ebeling, H., Rapetti, D., & Drlica-Wagner, A. 2010, MNRAS, 406, 1773

Marconi, A. & Hunt, L. K. 2003, ApJL, 589, L21

Markevitch, M. 1998, ApJ, 504, 27

Markevitch, M., Gonzalez, A. H., David, L., et al. 2002, ApJL, 567, L27

Mathews, W. G. & Brighenti, F. 2003, ARAA, 41, 191

Mathews, W. G., Faltenbacher, A., & Brighenti, F. 2006, ApJ, 638, 659

McCarthy, I. G., Schaye, J., Ponman, T. J., et al. 2010, MNRAS, 406, 822

McNamara, B. R. & Nulsen, P. E. J. 2007, ARAA, 45, 117

McNamara, B. R. & O'Connell, R. W. 1989, AJ, 98, 2018

McNamara, B. R., Wise, M., Nulsen, P. E. J., et al. 2000, ApJL, 534, L135

Meidinger, N., Andritschke, R., Elbs, J., et al. 2011, in Society of Photo-Optical Instrumentation Engineers (SPIE) Conference Series, Vol. 8145, Society of Photo-Optical Instrumentation Engineers (SPIE) Conference Series, 2

Méndez-Abreu, J., Aguerri, J. A. L., Barrena, R., et al. 2012, A&A, 537, A25

Merloni, A., Predehl, P., Becker, W., et al. 2012, ArXiv e-prints 1209.3114

Miller, E. D., Rykoff, E. S., Dupke, R. A., et al. 2012, ApJ, 747, 94

Miraghaei, H., Khosroshahi, H. G., Klöckner, H.-R., et al. 2014, MNRAS, 444, 651

Mittal, R., Hicks, A., Reiprich, T. H., & Jaritz, V. 2011, A&A, 532, A133

Mittal, R., Hudson, D. S., Reiprich, T. H., & Clarke, T. 2009, A&A, 501, 835

Molendi, S. & Pizzolato, F. 2001, ApJ, 560, 194

Moore, B. & Silk, J. 1995, ApJL, 442, L5

Motl, P. M., Hallman, E. J., Burns, J. O., & Norman, M. L. 2005, ApJL, 623, L63

Mulchaey, J. S. & Zabludoff, A. I. 1999, ApJ, 514, 133

Neumann, D. M. & Arnaud, M. 1999, A&A, 348, 711

Oemler, J. A. 1992, in NATO Advanced Science Institutes (ASI) Series C, Vol. 366, NATO Advanced Science Institutes (ASI) Series C, ed. A. C. Fabian, 29

O'Hara, T. B., Mohr, J. J., Bialek, J. J., & Evrard, A. E. 2006, ApJ, 639, 64

Osmond, J. P. F. & Ponman, T. J. 2004, MNRAS, 350, 1511

O'Sullivan, E., Vrtilek, J. M., Harris, D. E., & Ponman, T. J. 2007, ApJ, 658, 299

Panagoulia, E. K., Fabian, A. C., & Sanders, J. S. 2014, MNRAS, 438, 2341

Pascut, A. & Ponman, T. J. 2014, ArXiv e-prints 1412.6121

Peterson, J. R. & Fabian, A. C. 2006, Physics reports, 427, 1

Peterson, J. R., Kahn, S. M., Paerels, F. B. S., et al. 2003, ApJ, 590, 207

Peterson, J. R., Paerels, F. B. S., Kaastra, J. S., et al. 2001, A&A, 365, L104

Pilkington, J. D. H. & Scott, P. F. 1965, MEMRAS, 69, 183

Pillepich, A., Porciani, C., & Reiprich, T. H. 2012, MNRAS, 422, 44

Planck Collaboration, Ade, P. A. R., Aghanim, N., et al. 2014a, A&A, 571, A1

Planck Collaboration, Ade, P. A. R., Aghanim, N., et al. 2014b, A&A, 571, A16

Ponman, T. J., Allan, D. J., Jones, L. R., et al. 1994, Nature, 369, 462

Ponman, T. J., Bourner, P. D. J., Ebeling, H., & Böhringer, H. 1996, MNRAS, 283, 690

Pratt, G. W., Croston, J. H., Arnaud, M., & Böhringer, H. 2009, A&A, 498, 361

Predehl, P., Andritschke, R., Böhringer, H., et al. 2010, in Society of Photo-Optical Instrumentation Engineers (SPIE) Conference Series, Vol. 7732, Society of Photo-Optical Instrumentation Engineers (SPIE) Conference Series

Proctor, R. N., de Oliveira, C. M., Dupke, R., et al. 2011, MNRAS, 418, 2054

Puchwein, E., Sijacki, D., & Springel, V. 2008, ApJL, 687, L53

Rafferty, D. A., McNamara, B. R., & Nulsen, P. E. J. 2008, ApJ, 687, 899

Rafferty, D. A., McNamara, B. R., Nulsen, P. E. J., & Wise, M. W. 2006, ApJ, 652, 216

Randall, S. W., Forman, W. R., Giacintucci, S., et al. 2011, ApJ, 726, 86

Reichert, A., Böhringer, H., Fassbender, R., & Mühlegger, M. 2011, A&A, 535, A4

Reiprich, T. H. 2006, A&A, 453, L39

Reiprich, T. H., Basu, K., Ettori, S., et al. 2013, SSR, 177, 195

Reiprich, T. H. & Böhringer, H. 2002, ApJ, 567, 716

Robertson, J. G. & Roach, G. J. 1990, MNRAS, 247, 387

Rossetti, M., Eckert, D., Cavalleri, B. M., et al. 2011, A&A, 532, A123

Roychowdhury, S., Ruszkowski, M., Nath, B. B., & Begelman, M. C. 2004, ApJ, 615, 681

Ruszkowski, M., Brüggen, M., & Begelman, M. C. 2004, ApJ, 615, 675

Sanders, J. S., Fabian, A. C., Allen, S. W., et al. 2008, MNRAS, 385, 1186

Sanders, J. S., Fabian, A. C., Hlavacek-Larrondo, J., et al. 2014a, MNRAS, 444, 1497

Sanders, J. S., Fabian, A. C., Sun, M., et al. 2014b, MNRAS, 439, 1182

Sanderson, A. J. R., Ponman, T. J., & O'Sullivan, E. 2006, MNRAS, 372, 1496

Santos, J. S., Rosati, P., Tozzi, P., et al. 2008, A&A, 483, 35

Santos, J. S., Tozzi, P., Rosati, P., & Böhringer, H. 2010, A&A, 521, A64

Santos, W. A., Mendes de Oliveira, C., & Sodré, J. L. 2007, AJ, 134, 1551

Sarazin, C. L. 1986, Reviews of Modern Physics, 58, 1

Sarazin, C. L. & Bahcall, J. N. 1977, ApJS, 34, 451

Schechter, P. 1976, ApJ, 203, 297

Schellenberger, G., Reiprich, T. H., Lovisari, L., Nevalainen, J., & David, L. 2014, ArXiv e-prints 1404.7130

Schindler, S. 2004, APSS, 289, 419

Schlegel, D. J., Finkbeiner, D. P., & Davis, M. 1998, ApJ, 500, 525

Semler, D. R., Šuhada, R., Aird, K. A., et al. 2012, ApJ, 761, 183

Skrutskie, M. F., Cutri, R. M., Stiening, R., et al. 2006, AJ, 131, 1163

Snowden, S. L., Egger, R., Finkbeiner, D. P., Freyberg, M. J., & Plucinsky, P. P. 1998, ApJ, 493, 715

Snowden, S. L., Mushotzky, R. F., Kuntz, K. D., & Davis, D. S. 2008, A&A, 478, 615

Stanek, R., Evrard, A. E., Böhringer, H., Schuecker, P., & Nord, B. 2006, ApJ, 648, 956

Stott, J. P., Hickox, R. C., Edge, A. C., et al. 2012, MNRAS, 422, 2213

Sun, M. 2009, ApJ, 704, 1586

Sun, M. 2012, New Journal of Physics, 14, 045004

Sun, M., Forman, W., Vikhlinin, A., et al. 2004, ApJ, 612, 805

Sun, M., Jones, C., Forman, W., et al. 2007, ApJ, 657, 197

Sun, M., Voit, G. M., Donahue, M., et al. 2009, ApJ, 693, 1142

Sunyaev, R. A. & Zeldovich, Y. B. 1972, CoASP, 4, 173

Sutherland, R. S. & Dopita, M. A. 1993, ApJS, 88, 253

Takahashi, T., Mitsuda, K., Kelley, R., et al. 2014, in Society of Photo-Optical Instrumentation Engineers (SPIE) Conference Series, Vol. 9144, Society of Photo-Optical Instrumentation Engineers (SPIE) Conference Series, 25

Tamura, T., Kaastra, J. S., Peterson, J. R., et al. 2001, A&A, 365, L87

Tinker, J., Kravtsov, A. V., Klypin, A., et al. 2008, ApJ, 688, 709

Tozzi, P. & Norman, C. 2001, ApJ, 546, 63

Tremaine, S., Gebhardt, K., Bender, R., et al. 2002, ApJ, 574, 740

Urry, C. M. & Padovani, P. 1995, PASP, 107, 803

Vikhlinin, A., Burenin, R., Forman, W. R., et al. 2007, in Heating versus Cooling in Galaxies and Clusters of Galaxies, ed. H. Böhringer, G. W. Pratt, A. Finoguenov, & P. Schuecker, 48

Vikhlinin, A., Burenin, R. A., Ebeling, H., et al. 2009a, ApJ, 692, 1033

Vikhlinin, A., Kravtsov, A., Forman, W., et al. 2006, ApJ, 640, 691

Vikhlinin, A., Kravtsov, A. V., Burenin, R. A., et al. 2009b, ApJ, 692, 1060

Vikhlinin, A., McNamara, B. R., Hornstrup, A., et al. 1999, ApJL, 520, L1

Voevodkin, A., Borozdin, K., Heitmann, K., et al. 2010, ApJ, 708, 1376

Voigt, L. M. & Fabian, A. C. 2004, MNRAS, 347, 1130

Voit, G. M., Cavagnolo, K. W., Donahue, M., et al. 2008, ApJL, 681, L5

Voit, G. M. & Donahue, M. 2005, ApJ, 634, 955

Voit, G. M., Kay, S. T., & Bryan, G. L. 2005, MNRAS, 364, 909

von Benda-Beckmann, A. M., D'Onghia, E., Gottlöber, S., et al. 2008, MNRAS, 386, 2345

Werner, N., Urban, O., Simionescu, A., & Allen, S. W. 2013, Nat, 502, 656

Willingale, R., Starling, R. L. C., Beardmore, A. P., Tanvir, N. R., & O'Brien, P. T. 2013, MNRAS, 431, 394

Woo, J.-H. & Urry, C. M. 2002, ApJ, 579, 530

Xu, H., Kahn, S. M., Peterson, J. R., et al. 2002, ApJ, 579, 600

Xue, Y.-J. & Wu, X.-P. 2000, ApJ, 538, 65

Yoshioka, T., Furuzawa, A., Takahashi, S., et al. 2004, Advances in Space Research, 34, 2525

Zarattini, S., Barrena, R., Girardi, M., et al. 2014, A&A, 565, A116

Zhang, Y.-Y., Andernach, H., Caretta, C. A., et al. 2011, A&A, 526, A105

Zhang, Y.-Y., Reiprich, T. H., Finoguenov, A., Hudson, D. S., & Sarazin, C. L. 2009, ApJ, 699, 1178

Zwicky, F. 1933, Helvetica Physica Acta, 6, 110

Acknowledgements

I had a dream, and it was not this good—If I were to summarise my five year scientific journey in one sentence, this would be it. A lot of people have played an important role in shaping this dissertation and their direct or indirect contributions have made it what it is, and this is my small way of thanking them. By no means an exhaustive list, I apologise to many people who I am sure have been inadvertently left out here—trust me when I say that you too are in my thoughts.

The first person to thank would undoubtedly be my doctoral supervisor Prof. Thomas Reiprich. My association with Thomas goes back nearly as long as my time in Germany ($\sim$ 6 years) from the time I took classes with him, to my Master's thesis, followed by my doctoral work. Thomas' patient and careful guidance is in my opinion the primary reason I feel I have achieved some measurable success in my scientific work. I was fortunate enough to explore different scientific projects, and he always had encouraging words and excellent insight in all of them. Thank you for bringing me into the world of X-ray cluster science and for your constant encouragement and support.

I would also like to thank Prof. Peter Schneider for agreeing to be the co-referee of this dissertation. Peter had many useful comments to offer to improve the thesis which I was glad to take cognizance of. I would also like to thank Prof. Jochen Dingfelder and Prof. Andreas Hense for agreeing to be on my thesis committee.

Over the years, the open atmosphere in the research group meant that I had the opportunity to collaborate with a few people and more importantly, learn quite a lot from them. In particular, a lot of the work in this dissertation has benefited from direct and indirect contributions from Lorenzo Lovisari and Gerrit Schellenberger. Lorenzo provided very useful insight in the L_{X}–T work, particularly the bias corrections, which in the end turned out to be a major part of that paper. I am also particularly indebted in his contribution during the difficult postdoc application phase early this year. Gerrit and I have shared an office over the past few years, and we've had long discussions about everything from Chandra data analysis to Xbox gaming. Gerrit's insight into the technical side of X-ray data reduction was something I always valued, and we've collaborated successfully on a few projects, with hopefully more to come in the future. I would also like to thank my collaborators outside the institute, namely, Holger Israel, Rupal Mittal, Helen Eckmiller, and Jeremy Sanders. Holger in particular is someone I learnt quite a lot from during my early years, and he always provided much-needed, and well-appreciated insight on a lot of things, both scientific and otherwise. Katharina Borm navigated the warped world of the SIXTE with help from Nicolas Clerc, and was instrumental in providing the background files which eventually made its way into my eROSITA simulations. The program to calculate the cooling time was kindly provided by Paul Nulsen.

Astronomy cannot be done without computers, and our competent computing group (Reinhold Schaaf, Andreas Bödewig, Oliver Cordes et al.) ensured that system outages were few and far in between. A big thank you also to the extremely patient and competent secretaries of the AIfA, in particular Ellen Vasters and Christina Stein-Schmitz, who always went out of their way to help me and many others

navigate bureaucratic quagmires, some of them seemingly daunting at first, but dispatched away with swift alacrity by them.

The Argelander Institut für Astronomie has been the place where I have spent most of my 20s, and the impact that it has had on me as a person are unquestionable. A scientific institute is much more than brick and mortar, for its foundation rests on the minds that throng its corridors. In that sense, I have been fortunate to meet some amazing people in the AIfA, whose friendship and camaraderie I always cherished and will continue to do so long after my departure. Top on that list is fellow Marvelite, Jedi, and Whedonite, Philipp Wilking. In Philipp I have found one of my closest friends and confidantes, and a person on whom I place unquestionable faith and affection. I cannot even begin to count the number of amazing days and nights we've spent talking, watching movies, partying (with many amazing people whom I had the good fortune of meeting through him, including his wonderful girlfriend Nina), or just hanging around at the comic book store. Our trip to India where we covered no less than 5000 kms using everything from a horse-cart to a boat, is one of my most cherished memories.

Office 2.014 has been the home to some amazing people, who've all left behind many memories if not mementos. Vera, Holger, Brenda, Gerrit, thank you for the wonderful time we've had together, and for tolerating my eccentricities over the years—I hope I wasn't all that bad an office-mate.

The Astroclub was a big part during the early years, which I had to sadly give up in the final year due to my PhD commitments. A hat-tip to current and former members, especially, Dominik Klaes, David Muelheims, and Mikolaj Borzyszkowski for handling the Astroclub in a professional way.

Thanks are also in order to Douglas Applegate (and his wife Kristen), Alberto Doria, Aarti Nagarajan, Armin Rasekh, Miriam Ramos, Sandra Martin, Benjamin Magnelli, Hananeh Saghiha, and Maria Strandet with whom I've spent immeasurable hours of bonhomie, both inside and outside the institute. Former AIfA members Felipe Alves (and his wife Anna Laura), Marcelo Ferreira, Nina Roth, Vera Jaritz, Michael Marks, Brenda Miranda, and Matthias Klein (and his wife Snezhanka) are those who I count among my closest friends even today, and their presence in Bonn is sorely missed.

The hours spent figuring out the screenplay for Infinity War, discussing every tiny detail in Joss Whedon's work, and solving every crisis on the planet, with fellow Whedonite Vishwas Kaveeshwar might not have necessarily been the most prudent use of our times, but boy was it worth it! Thanks also go to Naveen Hegde, whose quiet demeanour, yet uncanny ability to crack anyone up in the most unlikely of circumstances made him a very integral cog of our little "brotherhood". A hat-tip to fellow amateur-politicos and cricketers Ripunjay Acharya, Rohan Diwe, Tushar Deshpande, and Dibya Mohanty with whom I've spent hours dissecting all sorts of frivolous things. A big thank you also to Shachi Joglekar, Aishwarya Ghule, Neha Sharma, and Deepak Venkanna who've all been part of this long journey since the time we met many years ago as clueless Master's students trying to acclimatise to a foreign country and tough coursework, and later decided to bite the bullet and stay on for a doctorate.

My extended, and constantly expanding family spread across four continents, and friends around the world may not always understand my work, but they had nothing but words of encouragement and goodwill throughout. Thank you all for those confidence boosts; it was, and is, much appreciated!

Lastly, the biggest thanks are reserved to my parents. They were probably the only people who backed me when I came up with the somewhat bizarre idea (at that point) of studying Astronomy. Over the years a lot has changed, but not their unwavering support. Without them, the aforementioned dream would have been just that, a dream...